DISSERTATIONES
CHIMICAE
UNIVERSITATIS
TARTUENSIS
225

PEETER VALK

Methanol Oxidation on Platinum-Rare-Earth Metal Oxide Activated Catalysts

DISSERTATIONES CHIMICAE UNIVERSITATIS TARTUENSIS
225

DISSERTATIONES CHIMICAE UNIVERSITATIS TARTUENSIS
225

PEETER VALK

Methanol Oxidation on Platinum-Rare-Earth Metal Oxide Activated Catalysts

UNIVERSITY OF TARTU
Press
1632

Institute of Chemistry, Faculty of Science and Technology, University of Tartu, Estonia

The dissertation is accepted for the commencement of the degree of Doctor of Philosophy in Chemistry on June 22nd, 2023, by the Council of Institute of Chemistry, University of Tartu.

Supervisors: Associate Professor Jaak Nerut, PhD
University of Tartu, Estonia

Professor Enn Lust, PhD
University of Tartu, Estonia

Opponent: Dr.-Ing. Mihails Kusnezoff
Fraunhofer Institute for Ceramic Technologies and Systems, Germany

Commencement: 31.08.2023 at 10:15. Auditorium 1020, Ravila 14a, Tartu

ISSN 1406-0299 (print)
ISBN 978-9916-27-296-1 (print)
ISSN 2806-2159 (pdf)
ISBN 978-9916-27-297-8 (pdf)

University of Tartu Press
www.tyk.ee

CONTENTS

1. LIST OF ORIGINAL PUBLICATIONS

I. **P. Valk**, J. Nerut, I. Tallo, E. Tee, K. Vaarmets, T. Romann, H. Kurig, R. Palm, and E. Lust, Structure and stability of partially chlorinated molybdenum carbide composite materials synthesised via high temperature chlorination, *Electrochim. Acta* **191** (2016) 337–345. https://doi.org/10.1016/j.electacta.2016.01.048

II. K. Vaarmets, **P. Valk**, J. Nerut, I. Tallo, J. Aruväli, S. Sepp, and E. Lust, Rotating Disk Electrode Study of Carbon Supported Pt-nanoparticles Synthesized Using Microwave-Assisted Method, *ECS Trans.* **80** (2017) 743–755. https://doi.org/10.1149/08008.0743ecst

III. **P. Valk**, J. Nerut, R. Kanarbik, I. Tallo, J. Aruväli, and E. Lust, Synthesis and Characterization of Platinum-Cerium Oxide Nanocatalysts for Methanol Oxidation, *J. Electrochem. Soc.* **165** (2018) F315–F323. https://doi.org/10.1149/2.0781805jes

IV. **P. Valk**, J. Nerut, R. Kanarbik, J. Aruväli, P. Paiste, I. Tallo, and E. Lust, Synthesis and Characterization of Platinum-Praseodymium Oxide Nanocatalysts for Methanol Electrooxidation, *J. Electrochem. Soc.* **166** (2019) F1062–F1069. https://doi.org/10.1149/2.0691914jes

Author's contribution:

Paper I: Performed synthesis of all materials, electrochemical measurements, and analysis of data. Mainly responsible for the preparation of the manuscript.

Paper II: Performed synthesis of materials and analysis of measurements data. Participated in preparation of the manuscript.

Paper III: Performed synthesis of all materials, electrochemical measurements, and analysis of data. Mainly responsible for the preparation of the manuscript.

Paper IV: Performed synthesis of all the materials, electrochemical measurements, and analysis of data. Mainly responsible for the preparation of the manuscript.

2. ABBREVIATIONS AND SYMBOLS

a	lattice parameter
BET	Brunauer Emmett Teller
C	gravimetric capacitance in F g^{-1}
CA	chronoamperometry
C_{CV}	gravimetric capacitance calculated from CV data in F g^{-1}
C_{edl}	electrical double layer capacitance
C_S	series capacitance
C_P	parallel capacitance
CPE	constant phase element
CV	cyclic voltammetry
d_{CV}	diameter of spherical Pt nanoparticles calculated from ECSA
d_{XRD}	average size of the crystallite calculated from XRD data
DMFC	direct methanol fuel cell
edl	electrical double layer
E	electrode potential
E^0	standard electrode potential
$E_{1/2}$	half-wave potential
ECSA	electrochemically active surface area of platinum nanoparticles
EDX	energy dispersive X-ray spectroscopy
EIS	electrochemical impedance spectroscopy
f	frequency of alternating potential
Fr%	fraction percentage
GCDE	glassy carbon disk electrode
$H_{ads/des}$	hydrogen adsorption/desorption
HER	hydrogen evolution reaction
HOR	hydrogen oxidation reaction
HRTEM	high resolution transmission electron microscopy
i	current density in A g_{Pt}^{-1}
i_{chron}	chronoamperometry current measured after 1800 s holding at a potential $E = -0.2$ V vs. MSE in 1 M CH_3OH + 0.5 M H_2SO_4 solution saturated with argon
i_{ECSA}	the peak current density of the positive going potential sweep measured in 1 M CH_3OH + 0.5 M H_2SO_4 solution saturated with argon (potential sweep rate 10 mV s^{-1}) normalised with regard to ECSA
i_{max}	gravimetric peak current density of the positive going potential sweep measured in 1 M CH_3OH + 0.5 M H_2SO_4 solution saturated with argon (potential sweep rate 10 mV s^{-1})
ICP-MS	inductively coupled plasma mass spectroscopy
j	current density in A m^{-2}
j_c	current density in A m^{-2} corrected for edl charging currents
j_d	diffusion limited current density in A m^{-2}
j_f	film diffusion limited current density controlled by reactant diffusion in the Nafion layer in A m^{-2}

j_{kin}	kinetic current density in A m^{-2}
j_L	measured limiting current density in A m^{-2}
j_{max}	peak current density of the positive going potential sweep measured in 1 M CH_3OH + 0.5 M H_2SO_4 solution saturated with argon (potential sweep rate 10 mV s^{-1})
K	shape factor
MA	mass activity
MOR	methanol oxidation reaction
MP-AES	microwave plasma atomic emission spectrometry
MSE	mercury-mercurous sulfate reference electrode ($Hg|Hg_2SO_4|$saturated K_2SO_4)
ORR	oxygen reduction reaction
PEMFC	proton exchange membrane fuel cell
PZC	point of zero charge
RDE	rotating disk electrode
REO	rare-earth metal oxide
RHE	reversible hydrogen (reference) electrode
rms	root mean square
R_s	high frequency series (electrolyte) resistance
SA	specific activity
S_{BET}	specific surface area calculated using the BET method
S_{meso}	total mesopore area
S_{micro}	total micropore area
SEM	scanning electron microscopy
t	time
T	temperature
TGA	thermogravimetric analysis
V_{meso}	volume of mesopores
V_{micro}	volume of micropores
V_{tot}	total volume of pores
w	pore width
wt%	weight percent
XRD	X-ray diffraction
$\|Z\|$	impedance modulus
Z'	real part of impedance
Z''	imaginary part of impedance
β	line broadening at full width at half maximum
Δ^2	weighted sum of squares
θ	Bragg angle
λ	wavelength
ν	electrode potential scan rate
τ	time constant
φ	phase angle
χ^2	square of standard deviation between the original data and the calculated EIS spectrum

3. INTRODUCTION

Polymer electrolyte (or proton exchange) membrane fuel cells (PEMFCs) and direct methanol fuel cells (DMFCs) are regarded as promising devices for alternative green energy complexes as in addition to green hydrogen, green methanol can be used for storage of cheap solar and wind energy [1]. These environmentally green DMFCs generate water, heat and CO_2, but no NO_x, SO_x, volatile organic higher molecular mass organic compounds or nanoparticles. Due to their relatively higher efficiency [2,3] PEMFC are under more intensive development than DMFC.

The main problem hindering the commercialisation of DMFC, as well as PEMFC, is the high overpotential of oxygen reduction reaction (ORR) at the porous cathode [4,5] and the complicated oxidation of methanol in DMFC [6,7]. Therefore, novel catalytically active materials are being developed for PEMFC and DMFC applications. For PEMFC, the most common catalyst material is Pt (or Pt alloys) [8,9]; however, for DMFC, Pt by itself is insufficient due to catalyst poisoning [6,7]. Along with Pt group metals, other alternatives are studied as co-catalysts with Pt.

Various catalysts with low Pt or precious metal loading are under intensive development, as well as precious metal-free catalysts. However, low activity or insufficient electrochemical stability is the main problem to be solved. For DMFCs, Pt-rare-earth metal oxide co-catalysts have been used and promising activities for methanol oxidation reaction (MOR) have been demonstrated.

It has been established that the efficiency and stability of electrocatalysts depend very strongly on the selection of appropriate combination of Pt-metals, additional co-catalysts as well as the attributes of the catalyst support materials [8,10,11].

The main demands for support materials are optimal micro-mesoporosity and macroporosity for quick mass transfer of oxygen and methanol, high electrical conductivity and electrochemical stability at different temperatures. Carbon is the most widely used catalyst support material for DMFC and PEMFC due to its affordability, porosity, conductivity and electrochemical stability [9]. These properties are determined by the synthesis conditions and the precursor materials of the carbon support material.

Carbon materials can be synthesised using various methods as well as from different raw materials, like carbon-rich organic precursors (e.g. Estonian peat [12,13]) as well as from different binary carbides, which have been under intensive study at the Institute of Chemistry in the University of Tartu [14–17]. In comparison with carbons prepared from different organic waste material or peat raw materials, carbons prepared from binary or ternary carbides have a more regular structure as well as tuneable micro-meso-macroporosity. Carbide derived carbons have a very high electrochemical stability. These materials have been intensively studied as catalyst supports for PEMFC and could also be used as DMFC catalyst supports.

The main aim of this work was to synthesise active and electrochemically stable Pt nanoclusters deposited onto carbon supports and additionally activated with cerium and praseodymium oxide for oxidation of methanol and to compare the properties of these materials with commercial catalysts. Different synthesis methods have been developed and the influence of deposition methods has been demonstrated. Various physical characterisation methods have been used to characterise the Pt-CeO_2 and Pt-PrO_x complex materials. The catalytic activity towards methanol electrooxidation was studied using various electrochemical methods (cyclic voltammetry, chronoamperometry, impedance spectroscopy). High activity towards MOR was observed for the synthesised platinum-rare earth metal oxide based complex catalysts.

In addition, the structure and stability of Mo_2C based carbon catalyst support materials were studied using various physical and electrochemical characterisation methods.

4. LITERATURE OVERVIEW

4.1. Polymer electrolyte membrane fuel cells

The conversion and storage of energy is an essential topic of research and various avenues are under study to reduce the ecological impact of energy generation. Fuel cells are energy conversion devices to generate electric energy with little to no greenhouse gases. Fuel cells using hydrogen as fuel emit only water as reaction by-products. Fuel cells offer higher efficiency than internal combustion as they are not constrained by the Carnot cycle [2,4,5]. In addition, the losses of energy conversion from mechanical energy are avoided.

Fuel cells generate electricity directly through chemical reactions. Fuel cells consist of an anode and cathode and an ion-conducting membrane between them. The oxidation of fuel occurs on the anode and reduction of oxygen occurs on the cathode. For PEMFCs a proton-conducting membrane (also called a polymer electrolyte membrane, e.g. Nafion) is used, through which protons move from the anode to the cathode, whereas electrons drive a load through the auxiliary circuit. A schematic of a fuel cell is shown in Fig. 1.

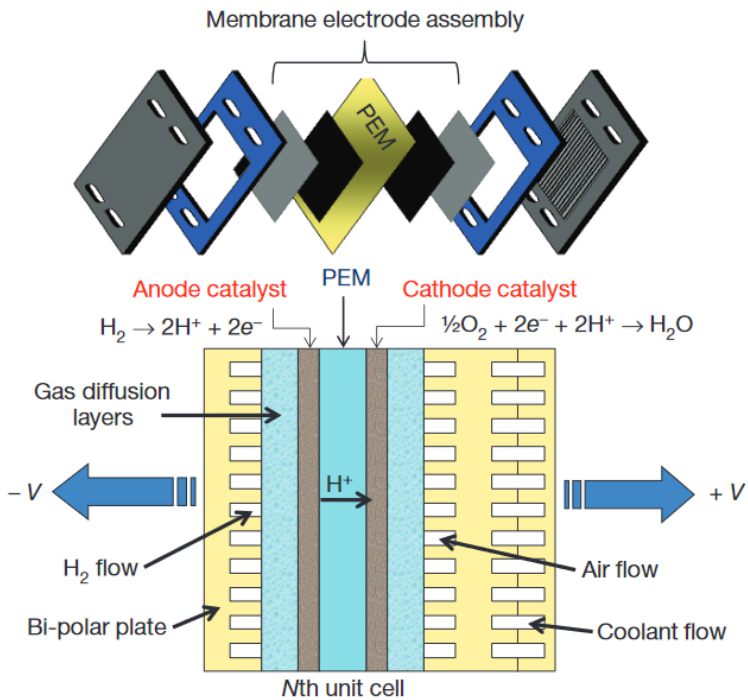

Figure 1. Construction and components of a hydrogen-fuelled polymer electrolyte membrane fuel cell [4].

PEMFCs use catalyst materials for the electrochemical reactions to occur at reasonable rates and with manageable overpotentials. For most low-temperature fuel cells, platinum is the most common catalyst material due to its high activity towards the oxygen reduction reaction as well as the oxidation of fuels such as hydrogen and methanol. [4,6,18]

In PEMFC, the cathode reaction is ORR [19–21]:

$$O_2 + 4H^+ + 4e^- \rightarrow 2H_2O, \qquad E^0 = 1.23 \text{ V}. \tag{1}$$

E^0 is the standard electrode potential.

If hydrogen is used as fuel, the anode reaction is the following [19–21]:

$$H_2 \rightarrow 2H^+ + 2e^-, \qquad E^0 = 0 \text{ V}. \tag{2}$$

The overall reaction is:

$$2H_2 + O_2 \rightarrow 2H_2O. \tag{3}$$

As such, the theoretical cell potential of a hydrogen-fuelled PEMFC is 1.23 V at room temperature [19,21]. However, due to various sources of overpotential, the actual potential of a single cell is lower. The main sources of overpotential are activation overpotential, ohmic overpotential and concentration (or mass transport) overpotential [20–22].

4.2. Oxygen reduction reaction

One of the main issues for PEMFCs is the sluggish nature of ORR, which accounts for nearly two-thirds of the overpotential [23,24].

There are two main pathways for ORR in acidic aqueous solutions: two-electron and four-electron pathway.

The four-electron pathway is shown in Eq. 1. The two-electron pathway is the following [19]:

$$O_2 + 2H^+ + 2e^- \rightarrow H_2O_2, \qquad E^0 = 0.70 \text{ V}. \tag{4}$$

The hydrogen peroxide can be further reduced electrochemically to water [19]:

$$H_2O_2 + 2H^+ + 2e^- \rightarrow 2H_2O, \qquad E^0 = 1.76 \text{ V}. \tag{5}$$

Alternatively, the hydrogen peroxide can decompose:

$$2H_2O_2 \rightarrow 2H_2O + O_2. \tag{6}$$

All the shown reactions consist of several elementary reactions [24–26].

The formation of hydrogen peroxide is undesirable, as it can negatively affect the membrane or electrode materials. Compared to the two-electrode pathway, the four-electrode pathway also offers more energy per reacted molecule [19].

4.2.1. Oxygen reduction reaction catalysts

To increase the kinetics of ORR in low temperature fuel cells, various catalyst materials have been under intensive study.

Pt nanoclusters have been intensively studied, and good catalytic activity has been observed even at very low loadings, demonstrating the importance of the catalyst support material and the dispersion of nanocatalyst on the support material surface [27,28].

While Pt is the most suitable catalyst material for ORR in PEMFC, its high cost is an issue, as well as the loss of catalytic activity due to nanoparticle growth on Pt nanocluster-activated catalyst materials [8]. As such, various Pt alloys and core-shell type catalysts are studied [8].

PtNi and PtCo alloys are among the most catalytically active materials towards ORR [29,30]. PtCo alloys are used in the Toyota Mirai fuel cell vehicle [31].

Pt-rare-earth metal alloys have also shown very high catalytic activity towards ORR [24,32–34]; however, facile and cost-efficient synthesis of Pt-rare-earth metal alloys is somewhat complicated.

To mitigate the negative aspects of Pt, platinum group metal free materials are also intensively studied as ORR catalysts. These are usually based on Fe- or Co-N/C materials, and very good results have been obtained, especially in alkaline conditions [35,36].

4.3. Fuels in PEMFC

The hydrogen oxidation reaction (HOR), shown in Eq. 2 is relatively facile compared to the ORR. On platinum catalysts, the HOR proceeds at nearly zero overpotential and at a very high rate. Hydrogen as a fuel is extremely desirable, as it has a very high energy density and it is essentially the only fuel that is possible to produce and use without carbon emissions. Its negative aspects are its low density requiring energetically costly compression or liquefaction for efficient storage, along with the cost of high-pressure storage vessels suitable for hydrogen [37].

In this aspect, methanol offers some advantages, such as cost and availability. Since methanol is a liquid, it is easily stored, transported, and distributed using existing infrastructure. However, methanol is toxic if swallowed, in contact with skin or if inhaled [38]. As methanol is virtually indistinguishable from ethanol outside of a well-equipped laboratory, mass methanol poisonings are a persistent occurrence throughout the world [39,40], either through malice

or negligence, and it is highly probable that widespread use of methanol as a fuel would only increase these occurrences. Currently, bittering agents have a negative impact on fuel cell performance [41].

While the HOR is fundamentally an extremely interesting, multi-faceted electrochemical process involving several steps, for practical applications in fuel cells, it is essentially a solved problem [28,42]. This is very much the opposite of MOR in fuel cells.

4.4. Methanol Oxidation reaction

Methanol oxidation to CO_2 can be summarised as the following reaction [6]:

$$CH_3OH + H_2O \rightarrow CO_2 + 6H^+ + 6e^- \quad E^0 = 0.02 \text{ V} \tag{7}$$

However, the process involves multiple steps occurring in separate potential regions, involving the adsorption of methanol molecules, the dissociation of water, the splitting of the C-H bond and the surface diffusion and reaction of the various intermediate products. As such, even though the thermodynamic potential of MOR to CO_2 lies very close to the equilibrium potential of hydrogen oxidation, the kinetics of the processes involved are slow and exhibit high overpotential. [6,43]

In addition, methanol crossover to cathode is another important source of overpotential in DMFC [44].

4.4.1. Methanol oxidation catalysts

As with ORR and HOR, platinum is the backbone of MOR electrocatalysis [6,7]. It is an excellent catalyst for splitting the C-H bond; however, pure Pt exhibits low activity towards MOR due to various reasons, such as the poisoning of the catalyst by reaction intermediates (e.g. CO) as well as the high potential required for water splitting on Pt. For these reasons, Pt is usually employed in conjunction with suitable additives in co-catalysts [6,43].

Ruthenium has been studied intensively as a co-catalyst with Pt for MOR for decades [43,45–48]. Ruthenium exhibits a lower potential for water dissociation, which helps overcome the poisoning of catalytic sites by CO. This is often referred to as the bifunctional mechanism, where Ru provides adsorbed active oxygen-containing groups for the oxidation of carbonaceous species adsorbed on Pt through surface diffusion [6,43,44,48].

An obstacle to using platinum and ruthenium at high loadings is their price. An extensive overview of various alternatives is given by Kakati et al. [7]. As alternative cheaper co-catalysts to ruthenium or as a ternary component to reduce the amount of precious metals in Pt-Ru catalysts, various oxide materials have been studied [49], such as WO_3 [50,51], ZrO_2 [50] and TiO_2 [52,53].

More recently, rare earth metal oxides (REO) have been shown to be suitable co-catalysts with Pt for MOR. CeO_2 has been studied most extensively

of this group of materials. A small overview of some results of Pt-REO catalysts is shown in Table I.

Various methods have been developed to synthesise Pt-REO catalysts.

In 2006, Tang and Lu [54] precipitated various REO catalysts in a basic aqueous solution with subsequent heat treatment. Pt was deposited onto the synthesised materials using the sodium borohydride method. The results were promising; however, the electrochemical activity of the catalysts was not very high. Notably, Ce oxide-based catalyst performed relatively worse than some other studied materials, with Pr oxide showing the highest activity.

In 2008, Tang and Lu [55] synthesised Pt-$PrCeO_x$-C mixed catalysts using the same method, which exhibited higher activity than their previously studied materials. This was credited to the mixed oxides having high oxygen mobility and oxygen vacancies.

Takahashi et al. [56] synthesised CeO_2 particles using the ammonium carbonate method and heat treatment at various temperatures. Pt particles were deposited onto the CeO_2 using the hydrogen reduction method. The synthesised materials were then dispersed with carbon particles and dried to obtain the final catalyst material. The synthesised materials exhibited higher performance than a commercial PtRu catalyst.

Guo and Jing [57] co-precipitated Pt and CeO_2 precursor in a basic aqueous solution over 6 days which was then heat treated at 400 °C. Compared to a Pt-C catalyst synthesised using the sodium borohydride method, better results were achieved; however, the dimensions of Pt nanoparticles in the two catalysts synthesised using different methods were not compared.

Gu et al. [58] synthesised CeO_2 particles via precipitation in a basic aqueous solution with subsequent heat treatment. The Pt particles were deposited using the ethylene glycol method in a microwave oven. Good activity was achieved for the synthesised materials depending on the CeO_2 content, with 20% CeO_2 having the highest activity. Remarkably, a Pt-C catalyst synthesised using the same method also had a relatively high or even comparable activity. It is probable that this is due to the very small Pt particle size achieved through microwave synthesis; however, the particle size of this catalyst material was not revealed for comparison.

Wang et al. [59] developed a method for depositing CeO_2 onto graphene sheets by oxidizing cerium ions using graphene oxide as the oxidant, thereby reducing it to graphene. Pt was deposited onto the synthesised material using the sodium borohydride method with the addition of L-lysine as a linker to preferentially deposit Pt onto the CeO_2 particles. The activity of this material was remarkably higher compared to a synthesised material without CeO_2. This was attributed to the L-lysine mediated method preferentially depositing Pt nanoparticles onto ceria, which avoids conglomeration of Pt nanoparticles due to their high mobility on graphene sheets.

Table I. Overview of Pt-rare-earth metal oxide catalysts

Catalyst	Measurement conditions	MOR activity	Ref.
Pt-CeO_x/C **Pt-PrO_x/C**	0.5M MeOH + 0.5M H_2SO_4; CV 50 mV/s CA 1000s (0.65V vs SCE) Pt+REO 10%	CV: 56.3 mA mg^{-1} (E_p=0.70V vs SCE) 92.2 mA mg^{-1} (E_p= 0.71V vs SCE) (estimated) CA: 4.09 mA mg^{-1}	[54]
Pt-$PrCeO_x$/ C(Vulcan)	0.5M MeOH + 0.5M H_2SO_4; CV 50 mV/s (E_p=0.68 V vs SCE) CA 1000s (0.65V vs SCE) Pt+REO 10%	CV: 118.3 mA mg^{-1} CA: 5.1 mA mg^{-1}	[55]
Pt-CeO_2/ C(Vulcan)	0.5M MeOH + 0.5M H_2SO_4; CV 50 mV/s (E_p=0.85V vs RHE) Pt 30%; T=28°C	CV: 2.8 mA $cm^{-2}{}_{Pt}$ (estimated)	[56]
Pt-CeO_2-MWCNT	1M MeOH + 1M $HClO_4$ CV 50 mV/s (E_p=0.64V vs SCE) CA 3600s; 0.5 V vs SCE Pt 10%	CA 3.5 mA cm^{-2} CV 14 mA cm^{-2} (estimated)	[57]
Pt-CeO_2/C	0.5M MeOH + 0.5M H_2SO_4; CV 20 mV/s E_p= 0.85 vs RE REO 20%, Pt 20%	CV: 11 mA cm^{-2}	[58]
Pt-CeO_2-GO	1M MeOH + 0.5M H_2SO_4; CV 100 mV/s E_p= 0.69 vs Ag/AgCl CA: 3600s; 0.742V vs Ag/AgCl	CV: 366 A $g^{-1}{}_{Pt}$ CA: 60 A $g^{-1}{}_{Pt}$ (estimated)	[59]
Pt-CeO_2/ Graphene	1M MeOH + 0.5M H_2SO_4; CV 50 mV/s E_p= 0.25 vs MSE Pt 20%	CV: 25 mA cm^{-2}	[60]
Pt-CeO_2/ C(Vulcan)	0.5M MeOH + 0.5M H_2SO_4; CV 20 mV/s E_p= 0.65 vs Ag/AgCl REO 6%, Pt 20%	20 mA cm^{-2}; 0.71 A $mg^{-1}{}_{Pt}$	[61]
Pt-CeO_2-PANI	0.5M MeOH + 0.5M H_2SO_4; CV 100 mV/s (E_p=0.7V vs SCE) T=30°C	CV: 361.33 A $g^{-1}{}_{Pt}$	[62]
Pt-CeO_2/ C(Vulcan)	1M MeOH + 0.5M H_2SO_4; CV 50 mV/s E_p= 0.6 vs SCE CA: 0.6V vs SCE Pt 18.6%	CV: 1116.9 A $g^{-1}{}_{Pt}$ CA: 350 A $g^{-1}{}_{Pt}$	[63]
Pt-$Ce_{0.7}Mo_{0.3}O_{2-x}$ /C(Vulcan)	1M MeOH + 0.5M H_2SO_4; CV 50 mV/s (E_p= 0.65 vs SCE)	CV: 1888.4 A $g^{-1}{}_{Pt}$	[64]
Pt-PrO_{2-x}- diamond	0.001M MeOH + 0.5M H_2SO_4; CV 50 mV/s (E_p=0.65V vs Ag/AgCl) CA 1000s; 0.6V vs Ag/AgCl	CV: 3 mA cm^{-2} CA: 0.5 mA cm^{-2}	[65]
$Pr_6O_{11}{\cdot}xH_2O$/Pt/ CNT	1.0M MeOH + 1M KOH CV 50 mV/s (E_p=−0.25V vs SCE)	CV: 1131 mA $mg^{-1}{}_{Pt}$	[66]

Chen et al. [60] synthesised a Pt-CeO_2-graphene catalyst using the ethylene glycol method in a microwave oven with pre-synthesised ceria particles. The cerium oxide-containing catalyst exhibited higher activity compared to an analogous catalyst without ceria. This was attributed to both a better dispersion of smaller Pt particles as well as promoted CO oxidation activity due to the addition of CeO_2.

Wu et al. [61] synthesised CeO_2-C materials at various calcination temperatures. Pt was thereafter deposited using the ethylene glycol method in an autoclave. Very high activity was recorded, with the highest activity corresponding to ceria calcined at 550 °C. This material also had the highest ECSA of the studied materials, corresponding to a Pt particle size of 2.5 nm. The catalytic activity was roughly two times higher than for a commercial Pt-C catalyst with a similar Pt particle size, exhibiting the beneficial influence of CeO_2.

Xu et al. [62] synthesised Pt-CeO_2/polyaniline three-layered hollow nanorod arrays using ZnO as a template. Good activity was achieved, with remarkable stability of the catalysts, with 97.89% of maximum activity remaining after 1000 cycles. It is also notable that the catalyst achieved its maximum activity only after several hundred cycles.

Dai et al. [63] used a modified ethylene glycol method under reflux to deposit Pt particles onto ceria synthesised using a histidine-assisted method. The Pt/His-CeO_2-C exhibited very high electrochemical activity towards MOR. In addition, another Pt/CeO_2-C material synthesised without histidine also exhibited very high activity, the materials being two to three times more active than Pt/C catalysts. Remarkably, however, the CO stripping curves showed a very small difference in activity between the Pt/C and Pt/CeO_2-C materials, although ceria-modified catalysts exhibited lower oxidation peak potentials. The authors attributed the very high activity towards MOR to improved CO_{ads} oxidation by oxygen vacancies and higher OH_{ads} species concentration on ceria surface. While facile CO_{ads} oxidation is important for high MOR activity, a comparison of the MOR and CO stripping plots in the article under discussion is arguably more suggestive of CeO_2 having a beneficial influence towards methanol electrooxidation along with some improvement in CO_{ads} oxidation activity compared to Pt/C.

Zhang et al. [64] showed Pt/$Ce_{0.7}Mo_{0.3}O_{2-x}$-C with extremely high MOR activity. The incorporation of Mo into the ceria lattice was suggested to enhance the surface oxygen concentration with more oxygen vacancies generated.

It has been suggested that in case of Pt-CeO_2 catalysts, the promoting effect arises from an analogous bifunctional mechanism as with Pt-Ru [49,54,67–69]. In a somewhat similar proposition, the generation of active adsorbed oxygen-containing surface groups has been explained through improved adsorption of water onto oxygen vacancies in the ceria particles [56]. In one review by Mori et al. [69], this has been summarised as the result of the high oxygen storage capacity of the CeO_x surface. Furthermore, CeO_2 has been suggested to inhibit the growth (recrystallisation) of Pt particles, contributing to the stability and increased catalytic activity [49,70].

Praseodymium oxide has been used in solid oxide fuel cells due to its high oxygen conductivity at higher temperatures [71]. In ambient conditions, praseodymium oxide exists as a mixed oxide Pr_6O_{11}. This oxygen-deficient state and its higher room-temperature conductivity [72] compared to CeO_2 make it a very interesting material to apply as an additive in Pt complex catalysts. Pt-PrO_x materials have been studied in a few papers as ethanol oxidation catalysts [73,74] as well as methanol oxidation catalysts.

As discussed above, Tang and Lu synthesised both Pt-PrO_x-C [54] and Pt-$PrCeO_x$-C [55] catalysts with decent activity towards MOR.

Chen et al. [65] deposited Pt and PrO_{2-x} electrochemically onto poly-crystalline diamond surface. Compared to Pt, increased MOR activity was achieved. The authors suggested that the main role of PrO_{2-x} was to improve the tolerance of surface poisoning of the Pt surface.

Yang et al. [66] studied Pr_6O_{11} and $Pr(OH)_3$ containing Pt/C catalysts in alkaline conditions. The authors concluded that both oxygen vacancies and hydroxyl groups improve the catalytic activity towards MOR, with oxygen vacancies having more importance.

Based on the established results [54,55,65,66], there is further room for tunable improvement of catalytic activity in both the synthesis of the praseodymium oxide as well as in the conditions of Pt nanocluster deposition to increase the catalytic activity of Pt-PrO_x catalysts.

In addition to this work, MOR on Pt-rare-earth metal oxide-based materials has been studied further in University of Tartu [75,76].

4.5. Mo_2C based catalyst support materials

The performance of PEMFCs depends highly on the chemical composition and porous structure of the support material used as the catalyst carrier. The commercial PEMFC catalysts are dominated by carbon black-based support materials (e.g. Vulcan XC72, KetjenBlack, etc.). It has been shown that in addition to good conductivity of the support material and good dispersion of the catalyst material on the support material, the porosity and pore size distribution of the support material plays an important role as well as the ratio of graphitised and amorphous carbon [10].

Carbon materials synthesised from Mo_2C (C(Mo_2C)) have a highly tuneable surface area and porosity (hierarchical porous structure) and have been shown to be prospective catalyst supports for PEMFC, as well as having some electrocatalytic activity towards ORR [11,14,77]. Pure C(Mo_2C) has demonstrated high gravimetric capacitance in aqueous [11,78] and non-aqueous [16] media. In addition, carbon-covered molybdenum carbide electrodes have been studied for supercapacitor applications and high capacitance values were observed; however, the results are somewhat inconclusive regarding the stability of the electrodes [79].

Mo_2C can be used in heterogeneous catalysis [80–82] and in electrochemistry as a catalyst for hydrogen evolution reaction (HER) [83–85] or as a co-catalyst activated with Pt nanoclusters for ORR where complex catalysts have demonstrated higher electrochemical activity compared to pure Pt [85,86].

The stability of molybdenum carbide based composite catalyst materials has received minor attention. It has been shown that bulk Mo_2C dissolves in acidic media at potentials more positive than 0.4 V vs. normal hydrogen electrode (NHE) however the maximal corrosion rate occurs at pH = 8 [87]. Analogous results have been found for Mo_2C thin films, which start to oxidise at $E > 0.5$ V vs. NHE (0.1 mA cm^{-2}) in acidic media [88]. Another study observed the dissolution of Mo_2C from Pt/Mo_2C thin film system at $E > 0.4$ V vs. NHE [89]. Molybdenum carbide particles synthesised from molybdenum oxide onto Vulcan XC72 have been shown to have good CO electrooxidation activity, yet during the activation phase in 0.5 M H_2SO_4 solution, cyclic voltammograms showed multiple reduction and oxidation peaks, as well as a drastic decrease of currents. However, the characteristics of activation were discussed very briefly [90]. Overall, molybdenum carbide seems to be rather stable in the HER potential region but unstable in the potential region of ORR [83–85,89,91].

5. EXPERIMENTAL

5.1. Synthesis of composite materials

5.1.1. Synthesis of C(Mo_2C)+Mo_2C materials

The molybdenum carbide derived materials were synthesised using a high-temperature chlorination method. The Mo_2C powder (-325 mesh, 99.5, Sigma-Aldrich) was loaded into a quartz vessel. The powder was reacted in a tube furnace at 750 °C with Cl_2 gas (AGA, 99.999%) for 2 hours. In case of complete chlorination, the reaction would follow a simple reaction scheme [14]:

$$Mo_2C + 5Cl_2 \rightarrow 2MoCl_5 + C \quad (8)$$

The molybdenum carbide was only partially chlorinated in this study, leaving some Mo_2C in the product. The percentage of Mo_2C in the product was dependent on the reaction time, with a longer chlorination time yielding more carbon and less Mo_2C. A fully chlorinated material without any noticeable Mo_2C was also synthesised.

During the initial heating and after the chlorination, the tube furnace was purged with argon (AGA, 99.999%), the heating to 750 °C took 15 minutes and the cooling to room temperature about 5 hours. After chlorination, the intermediate product was additionally treated with hydrogen (Linde GAS, 99.9999%) at 900 °C to remove excess chlorine, chlorides and surface functional groups from the composite material [14]. The heating step to 900 °C took about 20 minutes. The synthesised materials were designated as $C_{x\%}$, where *x%* indicates the weight percentage of carbon in the C(Mo_2C)+Mo_2C composite materials.

5.1.2. Synthesis of Pt-C(Mo_2C) and Pt-C(Vulcan) materials

Pt nanoparticles were deposited onto the carbon support materials using a microwave-assisted ethylene glycol method. $H_2PtCl_6 \times 6H_2O$ (Alfa Aesar, 99.9% metals basis) was dissolved in 1 ml of MilliQ+ water (18.2 MΩ cm) and ethylene glycol (puriss. p.a Reag. Ph. Eur., ≥ 99.5%, Riedel-de Haën) was added. The volume (30 ml to 100 ml) of ethylene glycol was used to vary the Pt complex concentration in the reaction mixture. The carbon material was added to the reaction mixture and depending on the desired pH of the reaction mixture, concentrated NaOH (Sigma-Aldrich, 99.99% metals basis, Semiconductor grade) solution was added dropwise during sonication in an ultrasonic bath. The molar ratio of OH^- to Pt in the reaction volume was kept constant at $OH^-/Pt = 8$. The reaction mixture was sonicated for three hours, after which the synthesis mixture was heated in a commercial 750 W microwave oven until boiling two times. The product was filtered and washed with MilliQ + water and dried in a vacuum oven at 80 °C and 50 mbar overnight.

The carbon support materials were commercial Vulcan XC72 (Fuel Cell Earth LLC) noted as C(Vulcan), C(Mo_2C) fully chlorinated at 750 °C as described in Chapter 5.1.1., and the commercial Vulcan XC72 material additionally treated with HNO_3, noted as C(Vulcan*).

The C(Vulcan*) material was prepared by boiling Vulcan XC72 in 65% HNO_3 for 3 hours, after which the mixture was diluted with MilliQ+ water and left to settle overnight. The mixture was washed with MilliQ+ water 3 times and the resulting suspension of modified carbon in MilliQ+ water was boiled for one hour. Thereafter the mixture was filtered and dried in a vacuum oven.

A summary of the synthesis conditions is shown in Table II.

Table II. Synthesis conditions of Pt-C(Mo_2C) and Pt-C(Vulcan) materials

Material	Support material	pH	$c(H_2PtCl_6)$ / M	Pt wt%
1	C(Vulcan)	~2	0.00191	23.7 ± 2.1
2	C(Vulcan)	~2	0.00245	21.2 ± 3.2
3	C(Vulcan)	12.3	0.00228	13.6 ± 2.1
4	C(Vulcan)	12.3	0.00295	14.7 ± 2.4
5	C(Vulcan)	12.5	0.00385	12.8 ± 2.7
6	C(Vulcan)	12.7	0.00670	16.4 ± 2.8
7	C(Vulcan*)	12.7	0.00663	8.6 ± 3.2
8	C(Mo_2C)750 °C	12.4	0.00332	18.4 ± 2.8

5.1.3.Synthesis of Pt-CeO_2-C materials

CeO_2 + C(Vulcan) materials were synthesised by dissolving the required amount of $CeNO_3 \times 6H_2O$ (Strem Chemicals, 99.9%-Ce) in 1 cm^3 of MilliQ+ water and adding Vulcan XC72 carbon black. 100 cm^3 of ethylene glycol (Fluka Analytical, puriss. p.a., Reag. Ph. Eur., ≥99.5%) was added and the pH was regulated to pH = 12 using concentrated solution of NaOH. The mixture was sonicated. A commercial 750 W microwave oven was used to heat the mixture twice to boiling using intermittent heating in five-second cycles. The heating of the mixture to boiling took less than five minutes. Between the two heating cycles, a 30-minute cooling step was applied. The cooled mixture was filtered (0.45 μm, Merck Millipore) using a pressure filtration system (Sartorius Stedim 16249) and dried in a vacuum oven.

Some of the synthesised CeO_2 + C(Vulcan) materials were additionally heated in a tubular oven at 600 °C for two hours in an argon (Linde Gas, 99.999%) atmosphere.

Platinum nanoparticles were deposited onto the synthesised CeO_2 + C(Vulcan) materials using a similar microwave heating method as discussed above, with $H_2PtCl_6 \times 6H_2O$ as the precursor material. The Pt complex acid was dissolved in 1 cm^3 of MilliQ+ water, and CeO_2 + C(Vulcan) support material and ethylene glycol were added. The concentration of the Pt complex in the reaction mixture

was varied by changing the volume of ethylene glycol. The pH of the reaction mixture was regulated using a concentrated solution of NaOH. The reaction mixture was sonicated for three hours. After that, the synthesis mixtures were heated in the commercial microwave oven as described above. The product was filtered, washed with MilliQ+ water, and dried in a vacuum oven. The details of the syntheses are summarised in Table III.

Table III. Synthesis conditions of Pt-CeO_2-C materials

Material	Support material	Reducing agent	pH [1]	OH^-/Pt [2]	Pt wt%
EG-1	CeO_2 + C(Vulcan) T = 600 °C	Ethylene glycol	~2		12%
EG-2	CeO_2 + C(Vulcan)	Ethylene glycol	11.6	3.0	12%
EG-3	CeO_2 + C(Vulcan) T = 600 °C	Ethylene glycol	9.5	0.6	4%
EG-4	CeO_2 + C(Vulcan) T = 600 °C	Ethylene glycol	12.3	6.1	31%
EG-5	CeO_2 + C(Vulcan) T = 600 °C	Ethylene glycol	12.4	8.0	21%
EG-6	C(Vulcan)	Ethylene glycol	9.7	1.3	13%
EG-7 [3]	C(Vulcan)	Ethylene glycol	~2		24%
NBH-1	C(Vulcan)	$NaBH_4$	8		15%
NBH-2	NBH-1 T = 600 °C				15%
IWI-1	CeO_2 + C(Vulcan) T = 600 °C	H_2			18%
Commercial [3]	C(Vulcan)				20%

[1] pH of the reaction media
[2] Mole ratio of OH^- and Pt in the reaction mixture
[3] Materials do not contain CeO_2.

The material marked as EG-6 was synthesised by dissolving the required amounts of both $CeNO_3 \times 6H_2O$ and $H_2PtCl_6 \times 6H_2O$ in 1 cm^3 of $MilliQ^+$ water. C(Vulcan), ethylene glycol and NaOH were added. The rest of the microwave synthesis was performed as described above.

The material marked as NBH-1 was synthesised using $NaBH_4$ as the reducing agent [92,93]. $H_2PtCl_6 \times 6H_2O$ was dissolved in MilliQ+ water to prepare a solution with Pt ion concentration of ~1 mM. The solution was stirred for one hour. The pH was regulated to ~8 via dropwise addition of 20% NaOH solution. The required amount of CeO_2 + C(Vulcan) support was suspended in the solution and stirred to form a homogenous suspension. A $NaBH_4$ (Aldrich, ≥98.0%) solution was prepared by dissolving 0.116 mg $NaBH_4$ in 3.08 cm^3 $MilliQ^+$ water. This solution was added dropwise to the CeO_2 + carbon suspension, which was stirred for another two hours, after which the suspension was left to settle overnight. The suspension was filtered, rinsed and dried in a vacuum oven at 45 °C.

A portion of the material NBH-1 was heated at 600 °C for two hours in an argon atmosphere. This material is marked as NBH-2.

The IWI-1 material was synthesised via ultrasound assisted incipient wetness impregnation of $H_2PtCl_6 \times 6H_2O$ solution in ethanol and further gas phase reduction under H_2/Ar atmosphere [94]. 65 mg $H_2PtCl_6 \times 6H_2O$ was dissolved in 1 cm^3 commercial ethanol (distilled over CaO). 100 mg CeO_2 + C(Vulcan) material was added to the solution. The slurry was sonicated for 30 minutes. Afterwards, the ethanol was evaporated under Ar flow at 100 °C for 1 h in a glass tube furnace. Subsequently, the sample was heated to 200 °C at a heating rate of 2.5 °C min^{-1} under Ar flow. The reduction was performed at this temperature using a mixture of 30 vol % H_2 in Ar (100 cm^3 min^{-1}) for 3 h. After the reduction, the sample was cooled to room temperature in Ar atmosphere.

5.1.4.Synthesis of Pt-PrO_x-C materials

$Pr(OH)_3$ was deposited onto the Vulcan XC72 carbon black using $Pr(NO_3)_3 \times 6H_2O$ (Aldrich, 99.9%, metals basis) as a precursor. One gram of praseodymium nitrate was dissolved in 25 cm^3 MilliQ+ water, 1.6 g of Vulcan XC72 was added and the slurry was sonicated for several hours. The slurry was heated to nearly boiling temperature while stirring vigorously using a magnetic stirrer. 10 cm^3 25% ammonium hydroxide was added. The resulting slurry was cooled and left to settle, then filtered using a vacuum filtration system and washed several times with MilliQ+ water. The resulting material was dried overnight in a vacuum oven at 110 °C at 50 mbar pressure.

The $Pr(OH)_3$-C material was calcined in different conditions, shown in Table IV, to obtain various PrO_x-C materials. The materials are distinguished in the text by the applied calcination temperature. The material PrO_x-C 300 was calcined in a Binder FP 53 heating chamber in ambient air. Other materials were calcined in a Carbolite tubular oven in argon flow.

Table IV. Synthesis conditions of PrO_x-C materials.

Material	Calcination temperature	Heating ramp	Atmosphere	Gas flow rate [(1)] / cm^3 min^{-1}	Calcination time [(2)]
PrO_x-C 300	300 °C	2 K min^{-1}	Ambient air	Forced convection	2 h
PrO_x-C 525	525 °C	3 K min^{-1}	Argon (5.0)	200 / 40	2 h
PrO_x-C 700	700 °C	3 K min^{-1}	Argon (5.0)	200 / 40	2 h
PrO_x-C 1100	1100 °C	3 K min^{-1}	Argon (5.0)	200 / 40	2 h

(1) Two gas flow rates are shown: higher value was used during the heating process, the lower value was used once the desired temperature was achieved.
(2) Calcination time refers to the time the material was at the desired temperature after the process of heating up the oven.

Platinum nanoparticles were deposited onto the calcined PrO_x-C materials via reduction of H_2PtCl_6 with hydrogen (the ultrasound assisted incipient wetness impregnation method). The calcined PrO_x-C materials and $H_2PtCl_6 \times 6H_2O$ were added together into a small vial. 1 cm^3 of ethanol (Merck KGaA, EMSURE®, absolute for analysis) was added and the mixture was sonicated to obtain a slurry. The slurry was carried into a quartz vessel. The quartz vessel was heated in a tubular oven to 100 °C at 2.5 K min^{-1} under argon (Linde Gas, 99.999%) flow and held there for 1 hour to evaporate the ethanol. Thereafter the vessel was heated to 200 °C at 2.5 K min^{-1} under the flow of a gas mixture of 30% electrolytic hydrogen (Model NMH_2 500, Linde Gas, >99.9999%) in argon and held there for 3 hours after which the vessel was cooled slowly under argon flow. For all materials, Pt was deposited using the same conditions, however, the materials are distinguished in text by the calcination temperature of the PrO_x-C material onto which the Pt was deposited.

Another Pt-containing material was synthesised using the same method and conditions, but using unmodified Vulcan XC72 as the catalyst support, this material is referred to as Pt-C blank.

The syntheses were performed so as to result in materials with 15% of Pt by weight, however Pt-PrO_x-C 1100 had a slightly higher Pt content.

A commercial 20% Pt-Vulcan XC72 (Fuel Cell Earth, LLC) was used as a reference material.

5.2. Preparation of the catalyst suspension

The catalyst ink for C(Mo_2C)+Mo_2C materials was prepared by suspending the materials in a mixture of 2-propanol (Sigma-Aldrich, ≥95%) and MilliQ+ water. Nafion 117 solution (Aldrich, 5% solution) was added to the suspension so as to result in a dry ink with a 5% Nafion ionomer content. The suspension was alternatingly mixed and sonicated for one hour to obtain a uniformly dispersed ink. The loading of the composite material on the electrode was held constant at 1 mg cm^{-2}.

The catalyst ink for Pt-C(Vulcan) and Pt-C(Mo_2C) materials was prepared analogously, however the Nafion content on the prepared electrode was kept constant at 20%.

The Pt-CeO_2-C materials were suspended in a 20 wt% mixture of 2-propanol in $MilliQ^+$ water. Nafion® 117 solution was added to the suspension so as to result in a 25% Nafion® ionomer content in the final catalyst layer on the electrode.

The Pt-PrO_x-C materials were suspended in 40 wt% mixture of 2-propanol in $MilliQ^+$ water. Nafion 117 solution was added to the suspension so as to result in an ionomer to carbon mass ratio of 1:2 on the final catalyst layer on the electrode.

The suspensions were sonicated using an ultrasonic probe (Sonics & Materials, Inc., 500 W). The ink was deposited onto a glassy carbon disk electrode (GCDE, PINE Instrument Company, electrode diameter 5 mm)

pressed into Teflon holder. The loading of Pt on the electrode for Pt-containing catalyst materials was 18 μg cm^{-2}.

5.3. Physical characterisation of catalysts

X-ray diffraction patterns for all materials were measured using a Bruker D8 Advance diffractometer with Ni filtered Cu Kα radiation (a 0.6 mm wide parallel beam, two 2.5° Soller slits, lynxEye line detector, λ = 0.154186 nm). The scanning step was 0.01° for 2θ (2θ was between 20° and 90°) and the total counting time was 166 s per step. The X-ray tube was operated at 40 kV and 40 mA.

The X-ray diffraction data was used to calculate the size of catalyst nanoclusters deposited onto carbon supports using the Scherrer equation [95]:

$$d_{XRD} = K\lambda/\beta\cos\theta, \quad (9)$$

where d_{XRD} is the average size of the crystallite in nm, K is the shape factor, assumed equal to 1 in this study, λ is the X-ray wavelegth, β is the line broadening at full width at half maximum in radians, and θ is the Bragg angle in degrees.

The porosity of the studied materials was estimated using the low-temperature (−195.8 °C) nitrogen sorption method [96] with an 3FLEX instrument (Micromeritics, USA). A non-local density functional theory model "Carbon-N2-77, 2D-NLDFT Heterogeneous surface" [97], available in SAIEUS software [98], (v2.02, Micromeritics, USA) was used to calculate the pore size distribution data. The specific surface area, S_{BET}, values were calculated according to the Brunauer-Emmett-Teller (BET) multipoint theory within the relative pressure range from 0.05 to 0.2. The total volume of pores, V_{tot}, was calculated from the amount of gas adsorbed near the saturation pressure (0.95). The *t*-plot method was used to calculate the volume of micropores, V_{micro}.

Raman spectroscopy measurements were performed using a Renishaw inVia micro-Raman spectrometer with Ar laser excitation (λ = 514 nm).

Scanning electron microscopy (SEM) measurements were performed using a FEI Helio Nanolab 600 DualBeam with a 50 mm^2 Oxford Instruments X-Max detector for energy dispersive X-ray spectroscopy (EDX).

The morphology of the C(Mo_2C)+Mo_2C materials was studied via high resolution transmission electron microscopy (HRTEM) method using a JEOL JEM-2200FS instrument at a 200 kV accelerating voltage. The samples were prepared by ultrasonically suspending the studied composite material in ethanol. One drop of the sample was deposited onto a copper grid covered with a holey carbon film and dried in an Ar atmosphere before measurements.

The composition of Pt-PrO_x-C materials was analyzed using a microwave plasma atomic emission spectrometry (MP-AES). The samples were dissolved prior to analysis with an Anton Paar Multiwave PRO microwave digestion system using NXF100 digestion vessels (PTFE-TFM liner) in 8N rotor. 10 mg

of sample was weighed into PTFE vessels, into which 6 cm^3 of 35% HCl (Carl Roth ROTIPURAN Supra) and 2 cm^3 69% HNO_3 (Carl Roth ROTIPURAN Supra) were sequentially added. The vessels were capped and digested in the microwave unit. After digestion the samples were diluted using 0.5 M HCl to a final dilution factor of 80000 and analyzed using Agilent 4210 MP-AES, calibrated using single element Pr and Pt solutions. Pr was measured at 417.939 nm and Pt at 265.945 nm.

Inductively coupled plasma mass spectroscopy (ICP-MS) measurements were carried out using an Agilent 8800x. The C(Mo_2C)+Mo_2C) composite material was decomposed in boiling concentrated HNO_3 (Merck, 65%, for analysis EMSURE® ISO), dissolving the molybdenum and evaporating most of the carbon as gas. The solutions were diluted to a volume of 250 cm^3, with molybdenum concentrations between 80 to 8000 μg dm^{-3}. Before measurements, the solutions were filtered through a 0.45 μm cellulose filter to remove any possible particles.

Thermogravimetric analysis (TGA) of the materials was performed with instrument NETZSCH STA449F3 using Al_2O_3 pan. The temperature range applied varied from 25 to 1000 °C. Different heating rates were used (2.5 and 10 K min^{-1}). The gas flow rate was 50 cm^3 min^{-1}. Weight of the sample was 10 mg. Nitrogen, oxygen and hydrogen were used in the studies.

5.4. Electrochemical measurements

A glass three-electrode electrochemical cell was used for the electrochemical measurements. The cell was washed with hot concentrated sulfuric acid (Sigma-Aldrich, 95.0-97.0%, puriss, p.a.) with the addition of hydrogen peroxide (Merck, 30%, for analysis EMSURE®). The cell was rinsed several times with demineralised water and MilliQ+ water.

The working electrode was mounted on a rotating disk electrode system from PINE Instrument Company. For most experiments, a mercury-mercurous sulfate electrode or MSE (Radiometer Analytical) connected to the cell via a Luggin capillary was used as a reference electrode, except in case of Pt-C(Vulcan) and Pt-C(Mo_2C) materials, where a reversible hydrogen electrode or RHE was used. The potential of MSE is $E = 0.7$ V vs. reversible hydrogen electrode in 0.5 M H_2SO_4. A large surface area platinum net was used as the counter electrode. An Autolab PGSTAT 204 or an Autolab PGSTAT 302N potentiostat was used for the measurements with Nova 1.11.2 software. The electrochemical measurements were performed in a Faraday cage at $T = 22 \pm 1$ °C.

0.5 M H_2SO_4 (Fluka, ≥95%, TraceSELECT) solution was used as the electrolyte. The solution was saturated with argon (Linde Gas, 99.9999%) before submerging the working electrode into the solution.

In case of Pt-C(Vulcan) and Pt-C(Mo_2C) materials, 0.1 M $HClO_4$ (Fluka TraceSelect Ultra or Merck Suprapur) was used, saturated with N_2 (Linde Gas, 99.999%). For ORR measurements, the solution was saturated with O_2 (Linde Gas, 99.999%).

In case of C(Mo_2C) + Mo_2C materials, the working electrode was submerged into the 0.5 M H_2SO_4 solution under a potential of 0.1 V vs. MSE. Before electrochemical measurements, the electrodes were stabilised in a process referred to in this work as ”cycling“. One “cycle” consisted of measuring seven current density (j) vs. potential (E) curves using the rotating disk electrode system (electrode rotation speed was 800 revolutions per minute) at potential sweep rate 10 mV s^{-1} and one analogous j vs. E curve at potential sweep rate 5 mV s^{-1}. In addition, one electrochemical impedance spectrum was measured at E = 0.1 V vs. MSE in the ac frequency range from 10 kHz to 50 mHz with a stationary electrode. The first, third and fifth “cycles” were measured in an argon (AGA, 99.9999%) saturated solution and the second and fourth “cycle” in an oxygen (AGA, 99.999%) saturated solution. These five “cycles” allowed for the complete wetting and stabilisation of the C(Mo_2C) + Mo_2C materials in the 0.5 M H_2SO_4 solution.

For Pt-C(Vulcan), Pt-C(Mo_2C), Pt-CeO_2-C and Pt-PrO_x-C materials, at the beginning of the measurements, the working electrode was conditioned according to a protocol proposed in the literature [99,100]. The conditioning procedure consisted of 100 potential scanning cycles at a scan rate of 500 mV s^{-1} in the potential range from −0.65 V to 0.5 V vs. MSE. The rotation rate of the electrode was 1600 rpm.

Cyclic voltammetry (CV) measurements (with the stationary electrode) were performed in the potential range from −0.67 V to 0.3 V vs. MSE at potential sweep rates from 20 mV s^{-1} to 400 mV s^{-1}. In case of C(Mo_2C)+Mo_2C, Pt-C(Vulcan) and Pt-C(Mo_2C) materials, the potential range was −0.71 V to 0.41 V vs. MSE.

To assess the series resistance value of the electrolyte solution, electrochemical impedance data were obtained in the ac frequency range from 10 kHz to 10 mHz (13 points per decade, ac voltage amplitude 5 mV rms) at fixed working electrode potential (E = 0.1 V vs. MSE). Impedance data at high frequencies were used to obtain the high frequency series resistance (R_s) value of the electrolyte.

Separate experiments were performed to further visualise the dissolution of Mo_2C from the C(Mo_2C)+Mo_2C composite materials. The electrode was submerged into the solution under the potential E = −0.65 V vs. MSE and cyclic voltammograms were measured in argon saturated solution in the potential range from −0.71 V to 0.41 V vs. MSE at a potential sweep rate of 0.5 mV s^{-1}.

For MOR studies, methanol (Aldrich, 99.9+%, HPLC grade) was added to the electrolyte solution so as to result in a 0.5 M H_2SO_4 + 1 M CH_3OH solution. CV measurements were performed in the potential range from −0.65 V to 0.41 V vs. MSE at potential sweep rate 10 mV s^{-1}. Chronoamperometry measurements were performed by holding the potential at E = −0.2 V vs. MSE for 30 minutes. Before the measurements, the solution was saturated with argon, during the measurements, argon was flown above the solution level.

For Pt-CeO_2-C materials, electrochemical impedance spectroscopy measurements were performed at fixed potentials −0.4 V, −0.2 V, 0.03 V and

0.18 V in an argon saturated solution both before the addition of methanol as well as afterwards. The *ac* frequency range was from 10 kHz to 10 mHz (amplitude 5 mV rms). During these measurements, the electrode was in stationary conditions.

The content of Pt in the catalyst layer was determined using electrochemical dissolution of Pt from the electrode [101]. The dissolution was performed in deaerated 6 M HCl solution (Sigma-Aldrich, 36.5-38%, Analytical specification Pr. Eur.). A large Pt net (50 cm^2) was used as a counter electrode. Before dissolution, the electrode was soaked in the HCl solution for at least 30 minutes under potentiostatic control. During pre-treatment period, the electrode was kept at a potential $E = 0$ V vs. Ag|AgCl|saturated KCl. The dissolution of Pt was performed in the potential range from 0.47 V to 0.95 V vs. Ag|AgCl|saturated KCl and the potential scanning rate was 0.5 mV s^{-1}. The dissolution currents were corrected for the electrical double layer (edl) charging currents and it was assumed that four electrons are transferred in the Pt dissolution process:

$$Pt + 6Cl^- - 4e^- = [PtCl_6]^{2-} \quad (10)$$

6. RESULTS AND DISCUSSION

6.1. X-ray diffraction measurements

6.1.1. C(Mo_2C)+Mo_2C materials

X-ray diffractograms (Fig. 2) show a significant presence of β-Mo2C phase in the partially chlorinated C(Mo_2C) + Mo_2C composite materials. The most intensive characteristic peaks are at 2θ = 34.4°, 38.7°, 39.4°, 52.0°, 61.9°, 69.8° [102,103]. Other phases present in the materials are γ-MoC (small peaks 2θ = 31°, 36°, 48°) [104] and MoO_2 (small peaks at 2θ = 26°, 37°) [105]. γ-MoC is an intermediate product of the chlorination process. MoO_2 is most probably a by-product formed when the partially reacted materials are first exposed to air after the synthesis steps. The peaks for these by-products are of a minor intensity and their content is very low.

A small graphite peak can be seen at 2θ=26° [14] for materials with a longer applied chlorination time.

X-ray fluorescence measurements were performed to confirm that no residual chlorine was present in the materials.

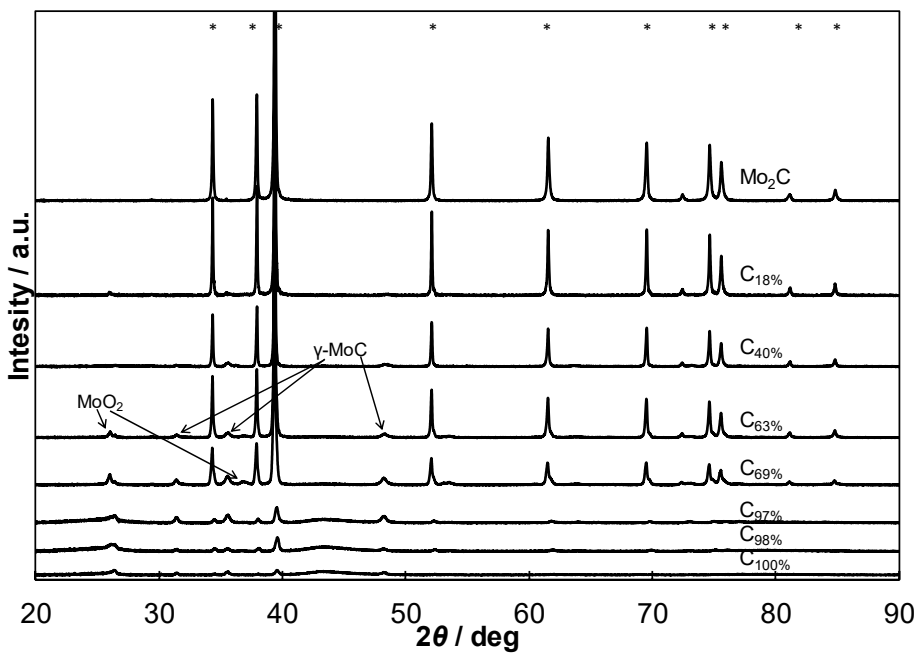

Figure 2. X-ray diffractograms of C(Mo_2C) + Mo_2C composite materials and Mo_2C powder (marked in figure). The percentage shows the weight percentage of C(Mo_2C) in C(Mo_2C) + Mo_2C composite material. The peaks corresponding to the β-Mo_2C phase are marked with asterisks. Peaks corresponding to MoO_2 and γ-MoC phases are indicated with arrows.

6.1.2.Pt-C(Vulcan) and Pt-C(Mo_2C) materials

The results of XRD measurements are shown in Fig. 3. The average crystallite sizes and modelling results using Topas software is shown in Table V. The size of Pt nanoclusters deposited onto the catalyst support materials was calculated according to Eq. 9. The Pt(220) reflection was used to calculate the value of β.

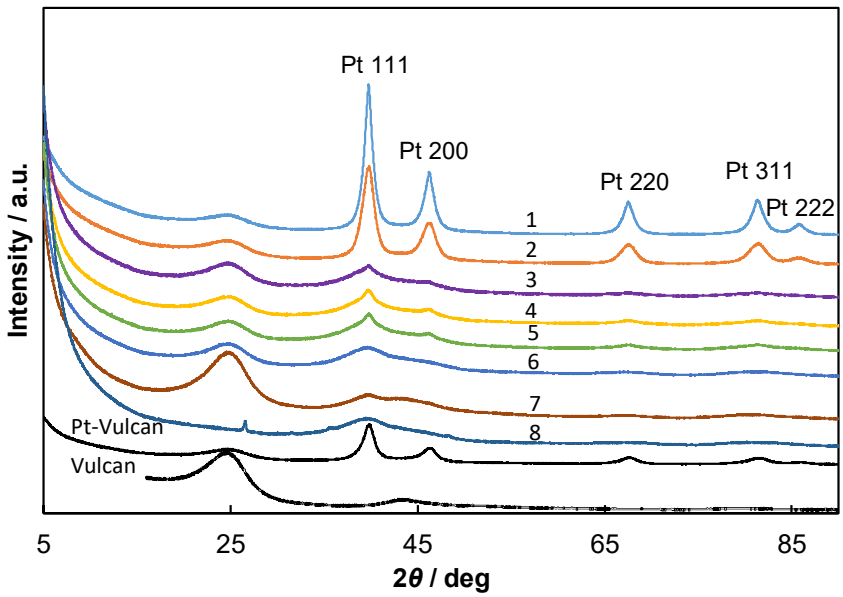

Figure 3. X-ray diffractograms for commercial Vulcan, Pt-Vulcan, and different Pt-C(Vulcan), Pt-C(Vulcan*) and Pt-C(Mo_2C) materials as noted in Table II.

The results indicate that the deposition of Pt onto the C(Vulcan) and C(Mo_2C) materials is influenced by the pH of the reaction mixture. In case of materials where Pt was deposited at acidic pH (materials 1 and 2), very pronounced peaks for different Pt planes are evident. Interestingly, the Pt precursor concentration in the reaction mixture also affects the Pt crystallite size. In case of materials 3 and 4, a small fraction of the Pt nanoclusters is noticeably larger, along with a fraction of Pt nanoclusters with extremely small sizes. In case of material 8 (Pt-C(Mo_2C)) and material 5, Pt nanoclusters of roughly 2 nm size were deposited at very close synthesis conditions (as shown in Table II). However, material 4, also synthesised at similar conditions, exhibits larger Pt crystallite sizes, which could mean that there is either a very narrow optimum for synthesis conditions, or there are other factors influencing the synthesis, such as the exact volume of reaction mixture which influences the temperature rise of the mixture during microwave heating.

Table V. Results of XRD measurements of Pt-C(Vulcan) and Pt-C(Mo_2C) materials as noted in Table II.

Material	Scherrer		Topas	
	***d*, nm**	**Fr%**	***d*, nm**	***a*, Å**
1	8.92	100	8.4	3.923
2	5.07	100	6.3	3.923
3	3.87			3.991
		60.6	1.2	4.031
		39.3	3.0	3.920
		0.2	20.6	3.923
4	4.11			4.026
		81.6	1.1	4.056
		11.5	3.2	3.916
		6.8	12.2	3.923
5	2.24	100	1.9	3.939
6	4.13			3.956
		69.9	1.4	3.972
		30.1	4.6	3.919
7	3.09	100	1.8	3.959
8	2.11	100	1.9	3.927
Pt-Vulcan	5.63			3.914

6.1.3.Pt-CeO_2-C materials

X-ray diffraction patterns for Pt-CeO_2-C materials are shown in Fig. 4. Several peaks corresponding to various Pt orientations can be seen in Fig. 4a. A wide peak at about $2\theta = 25°$, was attributed to the Vulcan XC72 carbon support. The peaks are significantly higher and sharper in the case of materials synthesised in acidic conditions. Very noticeable is the lack of diffraction peaks attributable to CeO_2 in case of material EG-1.

The materials synthesised in basic conditions exhibit peaks corresponding to CeO_2 ((111) at 28.5°, (200) at 33°, (220) at 47.5° and (311) at 56°), as well as wide and low Pt peaks. This shows that the acidic conditions support the formation of larger Pt crystallites, whereas in basic conditions smaller Pt nanoparticles precipitate, in accordance with literature data [106]. The peaks attributable to CeO_2 are usually wide and have low intensity. The diffractograms of C + CeO_2 materials (Fig. 4b) might indicate that under heat treatment conditions the support material had the effect of making the CeO_2 particles less crystalline. However, the peaks that can be seen in case of the C + CeO_2 support material that has not undergone heat treatment, are not present in the diffractograms of EG-2. The diffractogram of EG-6 does not have peaks attributable to CeO_2 either, as well as having Pt peaks with very low intensity. This indicates that subsequent microwave synthesis conditions also influence the crystallinity of

CeO_2. The material NBH-1 also lacks peaks that are attributable to CeO_2 but has several very small peaks of unknown origin and composition, supposedly resulting from the $NaBH_4$ assisted synthesis of Pt clusters, although the SEM-EDX data (discussed later) did show the existence of Ce but no other additives.

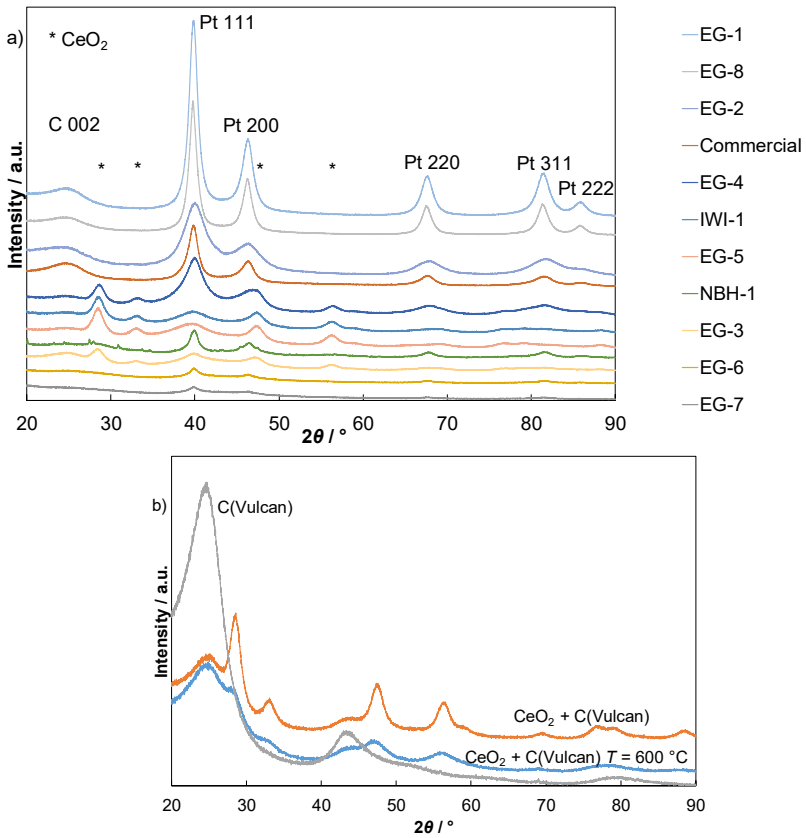

Figure 4. X-ray diffraction data of (**a**) studied materials (noted in figure), and (**b**) C(Vulcan) carbon support, CeO_2 + C(Vulcan) and CeO_2 + C(Vulcan) T = 600 °C materials.

The crystallite size of Pt nanoclusters was calculated according to Eq. 9. The Pt(220) reflection was used to calculate the values of β.

Full spectrum analysis using Topas software was conducted to calculate the lattice parameters and the sizes of Pt crystallites. The results are shown in Table VI. One of the more evident trends is that larger sizes of crystallites were calculated in case of materials synthesised using acidic conditions, as well as in the case of NBH-1. It must be noted that there is a discrepancy in the sizes of crystallites calculated using the Scherrer equation and using Topas software, especially in case of EG-6, which might be caused by the small CeO_2 clusters in

the materials, or by the presence of different Pt crystallites. Some of the differences are possibly due to the different presumptions inherent in different calculation methods. The calculated lattice parameter for Pt nanoclusters was 3.926±0.012 nm and it depends somewhat on the size of crystallites expressed on the surface of the catalysts.

Table VI. Results calculated from XRD data for Pt-rare-earth metal oxide based materials.

Material	Topas		Scherrer
	a / Å	d_{XRD} / nm	d_{XRD} / nm
EG-1	3.923	7.6	5.9
EG-2	3.917	2.9	2.8
EG-3	3.943	3.0	3.4
EG-4	3.931	2.8	2.8
EG-5	3.947	1.8	3.3
EG-6	3.919	4.2	10
EG-7	3.923	8.5	8.3
NBH-1	3.914	8.0	7.1
IWI-1	3.933	1.9	4.1
Pt-PrO_x-C 300		1.8	
Pt-PrO_x-C 525		0.8 [(1)] 5.0 [(1)]	
Pt-PrO_x-C 700		(0.9) [(2)]	
Pt-PrO_x-C 1100		(1.6) [(2)]	
Pt-C blank		1.3	
Commercial Pt-Vulcan	3.914		5.6

[(1)] Calculations indicated a bi-modal crystallite size distribution for Pt-PrO_x-C 525.
[(2)] Crystallite sizes in brackets are as calculated by Topas software, but most probably have a large error as described in the text.

6.1.4. Pt-PrO_x-C materials

X-ray diffractograms are shown in Fig. 5. In Fig. 5a the synthesised material $Pr(OH)_3$-C shows very intensive peaks in the whole range of measurement, with the most intensive peaks at $2\theta = 27.5°$, 28.5°, 40°, 49°, all attributable to $Pr(OH)_3$. The diffractogram indicates that the material is crystalline.

In case of the PrO_x-C materials, it can be seen that the heat treatment has a very profound effect on the materials. In case of PrO_x-C 300, with the exception of one slightly higher peak at $2\theta = 28°$, only very small peaks are visible. While the stable phase at room temperature in atmospheric conditions is Pr_6O_{11}, the aforementioned peak is also attributable to various other praseodymium oxides, for example Pr_9O_{16} or Pr_7O_{12}. Differentiating between different praseodymium oxide phases is very difficult based only on XRD data, as they exhibit peaks at very similar diffraction angles, and as such are not discussed in depth here, but rather referred to as PrO_x, with the x somewhat uncertain [107]. In case of PrO_x-C 300, the small sharp peaks in the diffractogram at $2\theta = 38.5°$, 45°, 65°,

78° were determined to be reflections from the aluminium sample holder. The small wide peaks at $2\theta = 46°$, 55° are attributable to PrO_x. Peaks attributable to $Pr(OH)_3$ are not visible. Overall, even at 300 °C in ambient air, the crystalline $Pr(OH)_3$ has been heat-treated to yield praseodymium oxides. However, the low temperature has rendered the resulting PrO_x clusters amorphous.

The subsequent material, PrO_x-C 525 is very analogous to PrO_x-C 300, even though a higher temperature and an argon atmosphere were used during the heat treatment. However, the peaks attributable to PrO_x are slightly higher and wider, and there are no peaks resulting from the aluminium sample holder.

The material PrO_x-C 700 is also similar to the previous materials. However, the peaks are more pronounced, indicating that due to the higher temperature of the treatment, the PrO_x clusters are more crystalline. In addition, at $2\theta = 32.5°$ another peak attributable to PrO_x is visible, which in case of the previous materials was almost visible as a small shoulder on the wide peak at $2\theta = 28°$.

The diffractogram for the material PrO_x-C 1100 is remarkably different from the previous materials. A variety of peaks can be seen. The most important difference with regard to the previous materials is the existence of sharp intensive peaks at $2\theta = 27°$, 29.5°, 30.5°, 40.5°, 47° etc. that are indicative of a Pr_2O_3 phase in the material. In addition, some peaks, for example at $2\theta = 29°$, 31.5° could be attributed to metallic praseodymium particles. A variety of peaks attributable to other praseodymium oxides than Pr_2O_3 are visible as well, although some of the more intensive peaks seen in case of previous materials are not present. The existence of Pr_2O_3 was to be expected, as it has been shown that at low oxygen partial pressures, Pr_2O_3 will be produced from PrO_x above 1063 °C [107]. As was shown by the diffractogram of PrO_x-C 300, the precursor $Pr(OH)_3$ will lose water to form PrO_x already at low temperatures. The presence of other praseodymium oxides than Pr_2O_3 is most probably caused by the absorption of oxygen after the heat treatment [107,108]. The presence of peaks attributable to praseodymium metal in the diffractogram might be caused by the reduction of some of the PrO_x by a small amount of the carbon support.

The X-ray diffractograms measured on the materials after the deposition of Pt can be seen in Fig. 5b. In case of Pt-PrO_x-C 300, only two wide peaks are visible. One peak, roughly at $2\theta = 26°$ corresponds to the carbon support material. This peak is also visible on all the other diffractograms in both Fig. 5a and Fig. 5b. At roughly $2\theta = 40°$ a wide peak corresponding to Pt is visible. The low intensity wide peak indicates that the Pt particles are very small.

In case of the material Pt-PrO_x-C 525, the diffractogram is very similar to the previous material. However, the peak corresponding to Pt is slightly sharper.

In case of the material Pt-PrO_x-C 700, the peaks at $2\theta = 26°$ and 40° are in agreement with data measured for the previous materials. However, there are some other small peaks which could indicate the presence of praseodymium chlorides or oxychlorides which could result from the chlorides from H_2PtCl_6 used for the deposition of Pt reacting with praseodymium oxides during synthesis.

The material Pt-PrO_x-C 1100 exhibits the carbon and platinum peaks discussed previously, as well as a variety of other smaller peaks, some of which correspond to praseodymium oxides or chlorides as discussed previously.

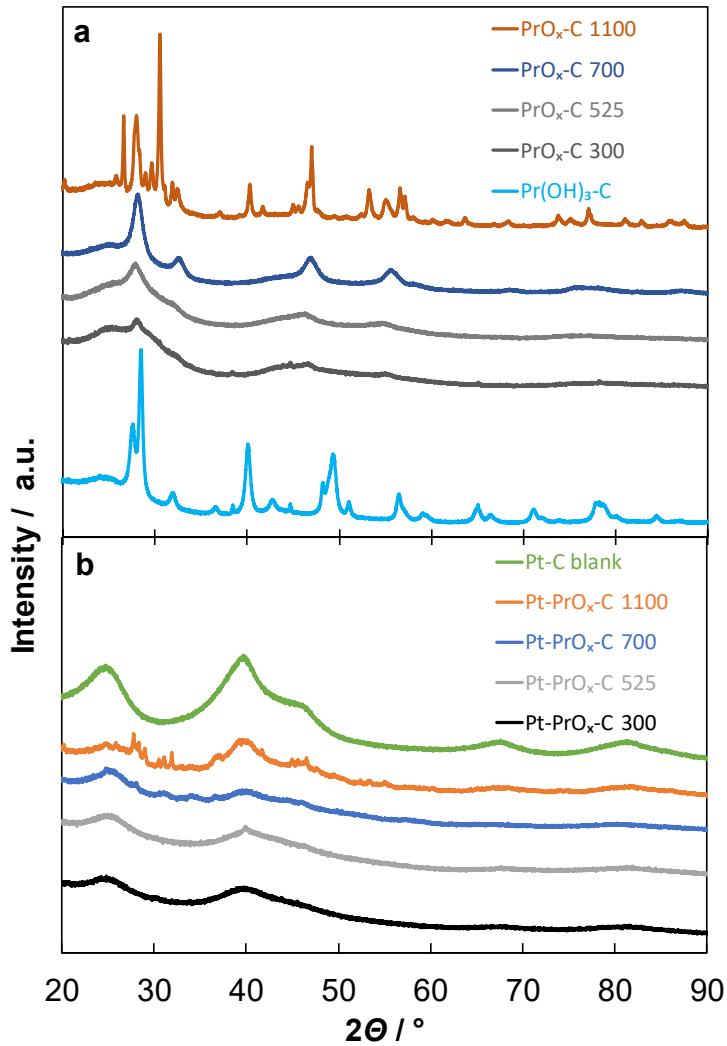

Figure 5. X-ray diffractograms of (**a**) catalyst supports PrO_x-C and $Pr(OH)_3$-C, and (**b**) catalysts Pt-PrO_x-C and Pt-C noted in figures

Overall, it is clearly visible that the deposition of Pt has a profound effect on the praseodymium oxides on the carbon support. Due to the synthesis occurring at elevated temperatures and in an inert gas and hydrogen mixture, the praseodymium oxides undergo additional phase transformations and evidently lose crystallinity. There are also some indications that the chlorides from the Pt

precursor might affect the praseodymium oxides. However, the wide and low peaks corresponding to Pt indicate that the synthesised Pt crystallites are very small.

For comparison, a diffractogram for the material Pt-C blank can be seen in Fig. 5b. In addition to the aforementioned carbon peak, wide peaks corresponding to Pt are seen. In case of this material, reflections corresponding to other Pt crystal planes are more pronounced than in case of the previous materials.

The size of the crystallites was estimated using full spectrum analysis with TOPAS software and are shown in Table VI. In case of Pt-PrO_x-C 700 and 1100, the peaks from praseodymium species made calculations very difficult, and as such, the sizes of crystallites for these materials are shown, but with a large probable error.

In case of $Pr(OH)_3$, the size of the crystallites was estimated to be in the order of 20 nm. In case of praseodymium oxides, calculations could not be performed, as there were no peaks corresponding to just one specific praseodymium oxide species.

6.2. Nitrogen sorption measurements

6.2.1. C(Mo_2C) materials

The results of low temperature N_2 sorption measurements are given in Table VII and the pore size distribution is shown in Fig. 6. It is clearly visible that the specific surface area (S_{BET}) strongly depends on the residual amount of Mo_2C in the C(Mo_2C) + Mo_2C composite materials. S_{BET} systematically increases with decreasing Mo_2C weight percentage in the studied materials. As Mo_2C is not porous and has a very low specific surface area, the increase in S_{BET} is fully attributable to the C(Mo_2C) component in the composite materials, although the increase in S_{BET} is not exactly proportional to the increase of the weight percentage of the carbon phase in the composite materials.

The total micropore area (S_{micro}) and micropore volume (V_{micro}) strongly depend on the chlorination time applied. Even though a nearly maximal surface area is obtained with a partial chlorination in the case of $C_{97\%}$, not all the mesopores have been fully opened, making this material relatively microporous. $C_{100\%}$ on the other hand has been fully chlorinated and all of the pores have been opened, making $C_{100\%}$ the most mesoporous of the materials. Overall, V_{meso} decreases systematically with the decrease of chlorination time, while the ratio of micropore volume to total pore volume (i.e. relative microporosity, V_{micro}/V_{tot}) is nearly constant throughout most of the studied composite materials (Table VII). In case of the composite materials with lower carbon content, the porous structure is similar, while $C_{97\%}$, $C_{98\%}$ and $C_{100\%}$ have somewhat different porosity.

The pore size distribution (Fig. 6) is very similar throughout the studied composite materials in the microporous region. The differences in the pore size distribution are mainly limited to the mesopore region (2 nm < d < 50 nm [109]).

Table VII. Results of nitrogen sorption measurements of C(Mo_2C) + Mo_2C composite materials.

Material	S_{BET} / $m^2\ g^{-1}$	S_{micro} / $m^2\ g^{-1}$	V_{tot} / $cm^3\ g^{-1}$	V_{micro} / $cm^3\ g^{-1}$	V_{meso} / $cm^3\ g^{-1}$	V_{micro}/V_{tot}
$C_{100\%}$	2020	1660	1.83	1.07	0.76	0.58
$C_{98\%}$	2010	1710	1.72	1.11	0.61	0.65
$C_{97\%}$	1970	1780	1.57	1.18	0.39	0.75
$C_{69\%}$	1050	910	0.92	0.59	0.33	0.64
$C_{63\%}$	970	850	0.83	0.54	0.29	0.65
$C_{40\%}$	370	320	0.31	0.22	0.09	0.71
$C_{18\%}$	180	170	0.17	0.11	0.06	0.65

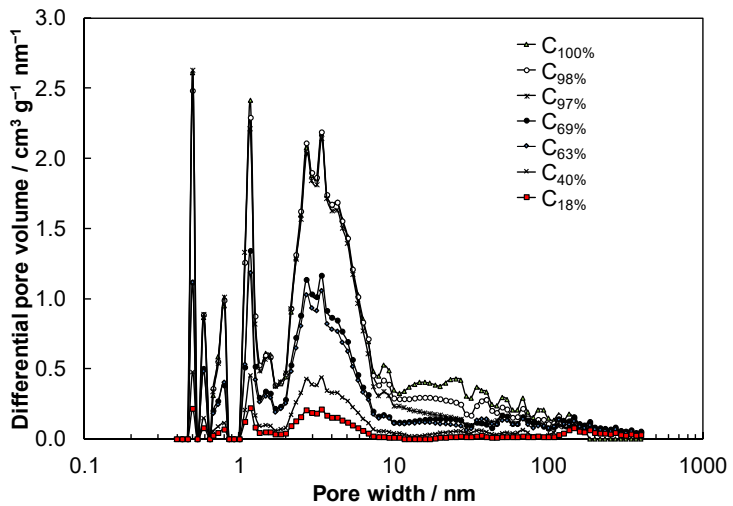

Figure 6. The pore size distribution of C(Mo_2C) + Mo_2C composite materials (marked in the legend). The percentage in the legend shows the weight percentage of C(Mo_2C) in C(Mo_2C) + Mo_2C composite material.

For the materials with almost maximum S_{BET} ($C_{100\%}$, $C_{98\%}$, $C_{97\%}$), the difference in the relative amount of mesopores above 10 nm is larger than the corresponding difference in micropores and smaller mesopores. The pore size distribution within the region 2 nm < w < 10 nm is practically overlapping for the materials with carbon content over 97%. This result agrees well with the data in Table VII. The maximum amount of mesopores has been obtained for material $C_{100\%}$.

Based on the relative microporosity data (Table VII) it could be speculated that micro- and mesopores are opened in steps, i.e. once a portion of micropores and smaller mesopores have been opened, a higher probability exists, that the pore walls between them are chlorinated, leading to the formation of larger mesopores, whereafter the step of opening of micropores is repeated. This could

explain how partial chlorination can lead to different microporosity in materials synthesised from the same precursor and having similar S_{BET}.

6.2.2.Pt-C(Vulcan) and Pt-C(Mo_2C) materials

Low temperature nitrogen adsorption/desorption measurements were performed and type IV adsorption isotherms, based on the Brunauer classification, were established [109,110] for the materials under study. The adsorption/desorption isotherms also demonstrate small hysteresis, characteristic of microporous-mesoporous carbon materials. The calculated porosity parameters (S_{BET}, S_{meso}, V_{tot}, etc.) are shown in Table VIII.

The results of N_2 sorption measurements for materials synthesised on Vulcan are comparable with the commercial Pt-Vulcan and undecorated Vulcan material, however S_{BET} has decreased for all materials following Pt deposition. The relative micropore area (S_{micro}/S_{BET}) has noticeably decreased and S_{meso} values are larger for these materials than for undecorated Vulcan material, whereas the volume of mesopores has noticeably decreased after the deposition of Pt, perhaps indicating that the Pt nanoparticles have preferentially deposited into the depths of larger mesopores.

Material 8, synthesised on the C(Mo_2C) support material, has a noticeably larger surface area, yet S_{meso} is comparable to materials synthesised on Vulcan. Comparison with the nitrogen sorption data for material $C_{100\%}$ (Table VII) indicates that the deposition of Pt nanoparticles has occurred almost entirely in the mesopores. This is supported by the increase in V_{micro} value, indicating that Pt nanoparticles are blocking some of the mesopores.

Table VIII. Results of nitrogen sorption measurements of Pt-C(Vulcan) and Pt-C(Mo_2C) materials as noted in Table II. Commercial Pt-Vulcan and Vulcan are shown for reference.

Material	S_{BET} / $m^2\ g^{-1}$	S_{meso} / $m^2\ g^{-1}$	S_{micro}/S_{BET}	V_{tot} / $cm^3\ g^{-1}$	V_{meso} / $cm^3\ g^{-1}$
1	171	111	0.35	0.201	0.180
2	187	107	0.43	0.210	0.176
3	225	145	0.35	0.266	0.239
4	197	115	0.42	0.219	0.188
5	197	124	0.37	0.229	0.205
6	190	118	0.38	0.221	0.195
7	160	101	0.37	0.192	0.168
8	1800	170	0.91	1.460	0.260
Pt-Vulcan	180	73	0.59	0.411	0.359
Vulcan	240	90	0.63	0.830	0.760

As shown in Fig. 7., the materials synthesised by microwave-assisted method have a bimodal pore size distribution in the microporous region, not present in the unmodified catalyst support material.

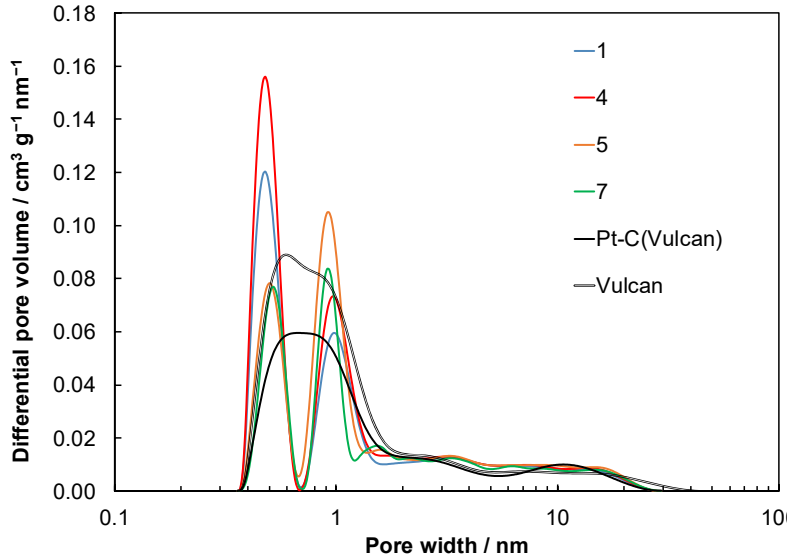

Figure 7. The pore size distribution of different Pt-C(Vulcan) materials as noted in Table II. Commercial Pt-Vulcan and Vulcan are shown for reference.

6.2.3.Pt-CeO_2-C materials

The shape of the measured adsorption isotherms based on the Brunauer classification was type IV [111]. The adsorption/desorption isotherms had a small hysteresis which is characteristic of microporous-mesoporous carbon materials [96–98]. The pore size distribution of the materials is shown in Fig. 8. The materials that have undergone microwave treatment have a very specific bimodal pore size distribution in the microporous region (pore width < 2 nm), with two peaks at 0.5 nm and 1 nm. While EG-3 has another smaller peak at around 25 nm, EG-2 has a very specific wide peak in the mesoporous region (pore width > 2 nm). The Vulcan XC72 support material and the Commercial Pt-Vulcan material do not have the bimodal pore size distribution in the microporous region.

The results of N_2 sorption measurements are shown in Table IX. The Vulcan XC72 support material has the highest surface area, as the addition of Pt and CeO_2 nanoclusters has the effect of decreasing the surface area. EG-6 has a rather low surface area, as well as a very low S_{micro}/S_{BET} ratio. The rest of the materials synthesised using the microwave heating method have similar S_{micro}/S_{BET} ratios.

The Vulcan XC72 support material exhibits the highest total pore volume, while the synthesised materials have a roughly similar total pore volume at about four times less than the support material. The commercial Pt-Vulcan

material has a medium total pore volume. The volume of mesopores is roughly similar for the synthesised materials, but with a value several times lower than that of the support material. It is interesting that the ratio of V_{micro}/V_{tot} has somewhat increased for the synthesised materials, indicating that the Pt and CeO_2 clusters are microporous.

Table IX. Results of nitrogen sorption measurements of Pt-CeO_2-C materials.

Material	S_{BET} / $m^2\ g^{-1}$	S_{micro} / $m^2\ g^{-1}$	S_{micro}/S_{BET}	V_{tot} / $cm^3\ g^{-1}$	V_{micro} / $cm^3\ g^{-1}$	V_{micro}/V_{tot}
EG-1	144	54	0.37	0.179	0.026	0.14
EG-2	212	72	0.34	0.270	0.050	0.19
EG-3	170	75	0.44	0.195	0.034	0.18
EG-4	139	58	0.42	0.162	0.026	0.16
EG-5	148	64	0.43	0.176	0.030	0.17
EG-6	114	16	0.14	0.203	0.006	0.03
NBH-2	125	56	0.45	0.144	0.026	0.18
IWI-1	99	26	0.26	0.140	0.011	0.08
EG-7	171	60	0.35	0.201	0.021	0.11
Pt-Vulcan	180	107	0.59	0.411	0.052	0.13
Vulcan	242	148	0.61	0.833	0.068	0.08

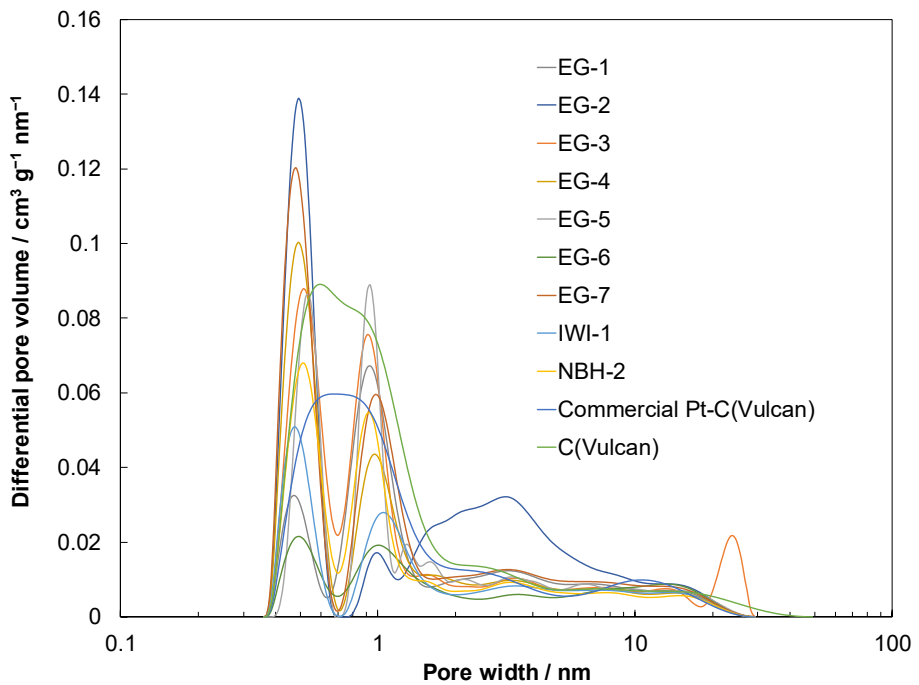

Figure 8. The pore size distribution of the catalyst support and different synthesised Pt-CeO_2-C catalysts (noted in figure)

6.3. Raman spectroscopy results

Raman spectra (Fig. 9) of the C(Mo_2C)+Mo_2C materials were measured from various particles that were visually separable under an optical microscope. The inset in Fig. 9 shows Raman spectra taken from particles with a completely chlorinated surface (black under optical microscope). A clear presence of amorphous carbon particles in all the materials is evident by the distinctive wide D-band at ~1350 cm^{-1} and G-band at ~1580 cm^{-1} [112,113]. The spectra taken from particles with a partially chlorinated surface (brighter and larger under optical microscope), are shown in Fig. 9. These spectra show a presence of Mo_2C, although its peaks are of low intensity. The presence of MoO_3 [114] clashes with XRD data, where another form of molybdenum oxide was seen, but it is very probable that this was oxidised during the measurements by the high energy laser used in the Raman spectroscopy study [115]. For materials $C_{100\%}$ and $C_{97\%}$, particles with a partially chlorinated surface were not found in the sample.

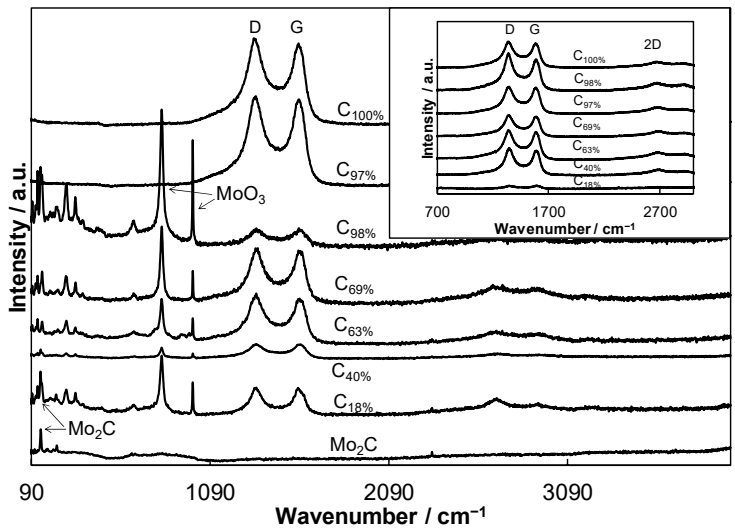

Figure 9. Raman spectra of C(Mo_2C) + Mo_2C composite materials and Mo_2C powder (marked in figure). The percentage shows the weight percentage of C(Mo_2C) in C(Mo_2C) + Mo_2C composite materials. Raman spectra are taken from particles with a partially chlorinated surface. Peaks corresponding to Mo_2C and MoO_3 are indicated with arrows. The inset shows Raman spectra taken from particles of C(Mo_2C) + Mo_2C composite materials with a fully chlorinated surface. The D, G and 2D in the figure mark D-, G- and 2D-bands of carbon, respectively.

6.4. Scanning electron microscopy data

6.4.1. Pt-CeO_2-C materials

In case of the Pt-CeO_2-C material EG-2, very good dispersion of the Pt nanoparticles was seen (Fig. 10a), as well as very uniform size of the Pt nanoparticles on the support material. The size of the nanoparticles is in the range of 2 to 4 nm. The nanoparticles can also be seen inside the porous structure of the catalyst support material. The dimensions of the carbon particles range from 10 nm to 100 nm. In case of the material NBH-1 (Fig. 10b), the Pt nanoparticles are comparatively more agglomerated and not as well dispersed. This is in accord with the XRD data (Table VI).

SEM-EDX data was used to confirm the existence of CeO_2 particles which are not distinguishable on the micrographs.

6.4.2. Pt-PrO_x-C materials

In case of $Pr(OH)_3$-C material (Fig. 11a), $Pr(OH)_3$ nanorods are visible on the micrographs, however they tend to be somewhat unevenly distributed and agglomerated at times.

The nanorods are visible also after the heat treatment and Pt deposition in case of the material Pt-PrO_x-C 700 (Figs 11b and 11c). The dimensions of the nanorods are similar to those in the precursor material. This indicates that the changes in X-ray diffractograms due to Pt deposition as discussed previously are due to changes in crystallinity rather than morphology. Pt particles are only visible at higher magnifications, indicating that the Pt particles are very small and evenly distributed.

EDX data for $Pr(OH)_3$-C indicates that the $Pr(OH)_3$ constituted roughly 20% by weight. In case of Pt-PrO_x-C 700, the mass percentage of PrO_x was 20% and the mass percentage of Pt around 15%. In addition, some chlorine was detected, which most probably resulted from the precursor material (H_2PtCl_6) used for the deposition of Pt.

The commercial Pt-C, shown in Fig. 11d, exhibits an uneven distribution of Pt clusters with a wide variety of sizes.

6.5. High resolution transmission electron microscopy data

HRTEM micrographs show areas of Mo_2C in an amorphous partially chlorinated carbon matrix (Figs 12a and 12c). The Mo_2C particles are not of a core-shell type, but rather surrounded by unordered amorphous carbon. This could be explained by the same reaction scheme as was proposed in the discussion of N_2 sorption results. In some areas, atomic lattices of the Mo_2C precursor still present in the chlorinated product can be seen (Fig. 12c), with the distance between two Mo atoms at around 2.6 Å. Some small graphitic areas are evident in carbons that were chlorinated for a longer time (Fig. 12b).

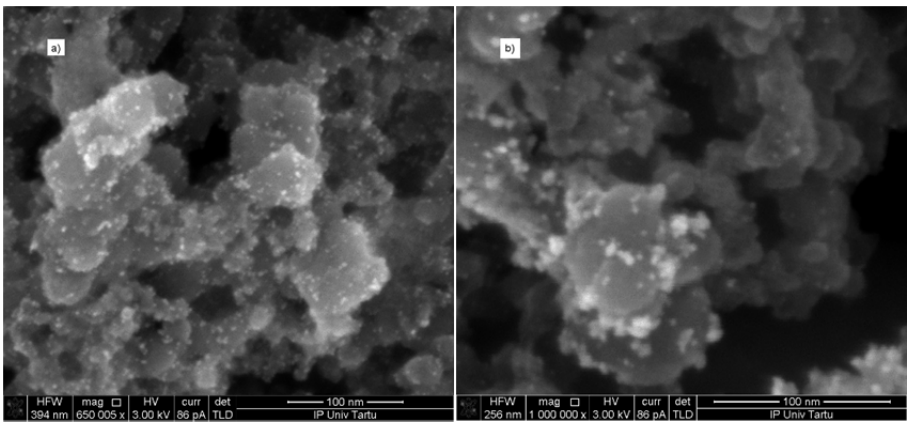

Figure 10. Scanning electron microscopy micrograph of Pt-CeO_2-C catalysts: **(a)** the synthesised EG-2 material and **(b)** the synthesised NBH-1 material.

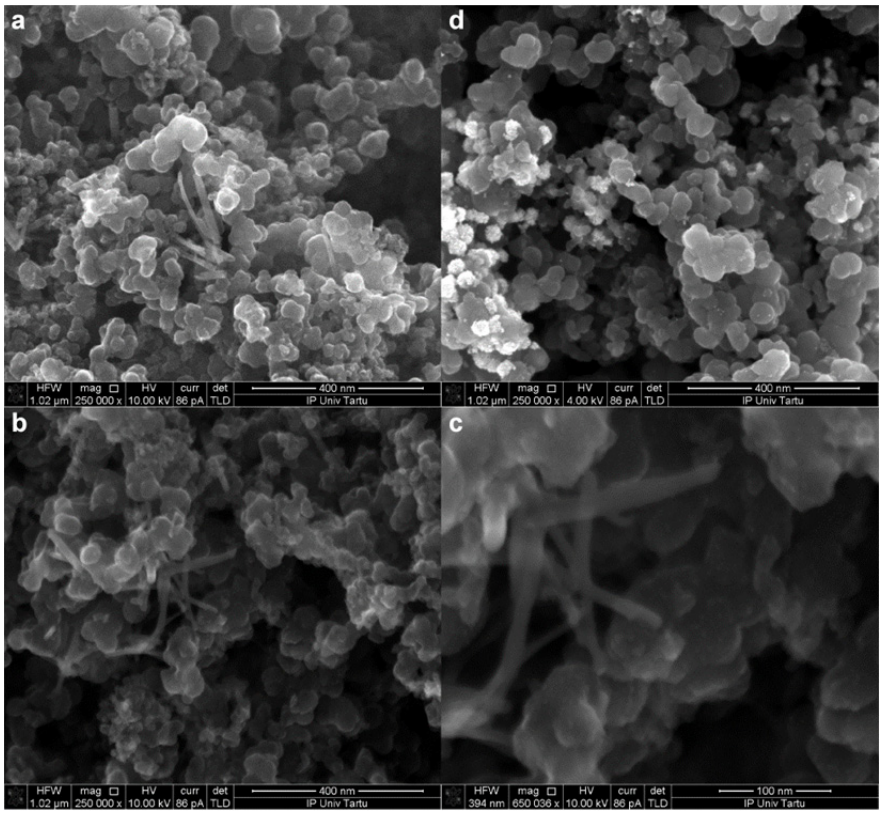

Figure 11. Scanning electron microscopy micrographs measured for different materials: **(a)** $Pr(OH)_3$-C, **(b)** and **(c)** Pt-PrO_x-C 700 at different magnifications, **(d)** commercial Pt-C.

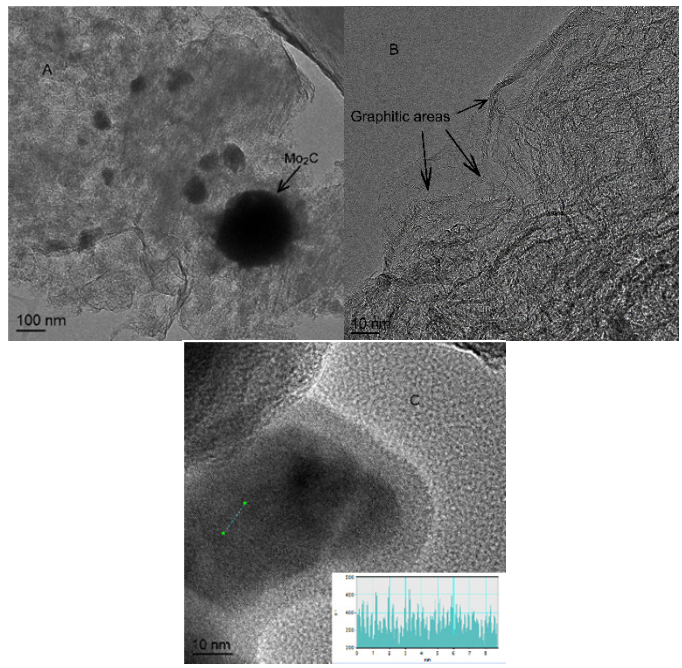

Figure 12. (**a**) and (**b**) high resolution transmission electron microscopy (HRTEM) micrographs of $C(Mo_2C) + Mo_2C$ composite material $C_{69\%}$. (**c**) HRTEM micrograph of $C(Mo_2C) + Mo_2C$ composite material $C_{40\%}$. The inset shows the transmitted electron intensity profile along the bright line on the figure. The percentage shows the weight percentage of $C(Mo_2C)$ in the $C(Mo_2C) + Mo_2C$ composite material.

6.6. Thermogravimetric analysis results

The process of converting $Pr(OH)_3$ to PrO_x was separately studied using thermogravimetric analysis (TGA) in nitrogen atmosphere and in synthetic air. The data are shown in Fig. 13a.

The material $Pr(OH)_3$-C is stable up to 225 °C. At higher temperatures $Pr(OH)_3$ transforms into PrO_x with the loss of water. The mass loss is about 3.25 wt%. The further mass loss at higher temperatures than 400 °C in the nitrogen atmosphere is probably caused by the cleaning of the chemically modified carbon surface, i.e. separation of functional groups from the surface of carbon. Of course, the composition of PrO_x could change during the temperature treatment; however, the corresponding changes in mass are small. In synthetic air, the carbon starts to oxidize at 400 °C (Fig. 13a) and the oxidation is complete at 720 °C. The total mass loss in synthetic air was 81 wt%. Further temperature increase did not cause any visible mass loss. To record the mass changes associated with various forms of praseodymium oxide the mass of the sample should be substantially higher. According to the TGA data, the material $Pr(OH)_3$-C contain 23.1±0.5 wt% $Pr(OH)_3$. In the calculations, it was assumed that in the presence of oxygen, the stable form is Pr_7O_{12} in the temperature

range from 700 to 1000 °C [107] and the mass loss caused from further oxidation of carbon was not taken into account.

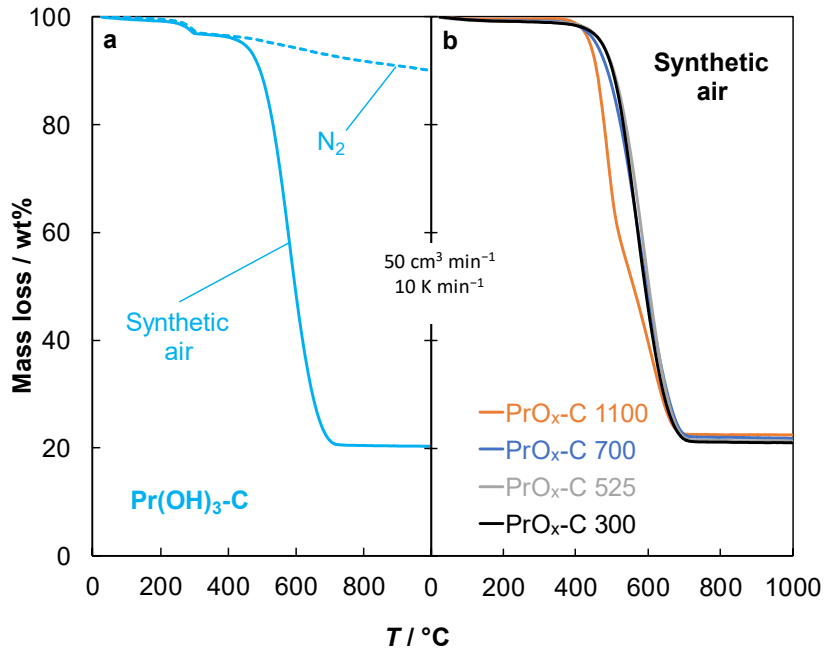

Figure 13. Thermogravimetry of materials **(a)** $Pr(OH)_3$-C and **(b)** PrO_x-C. The atmosphere is noted in figure. The heating rate was 10 K min^{-1} and gas flow rate was 50 cm^3 min^{-1}.

The aim was to synthesize the material PrO_x-C at temperatures 300, 525, 700 and 1100 °C, so the decomposition of hydroxide was studied at these temperatures (Table IV). As decomposition of carbon was not seen at 300 °C in synthetic air, the synthesis of PrO_x-C 300 was performed in ambient air i.e., in well-oxygenated conditions. The other materials were synthesised in an inert atmosphere to avoid the oxidation of carbon.

The PrO_x-C materials were decomposed in synthetic air to establish their quantitative composition (Fig. 13b). After burning off the carbon, the weight loss at 800 °C was very similar for all PrO_x-C materials. It was assumed that after heating in synthetic air, the stable form of praseodymium oxide at elevated temperatures is Pr_7O_{12} [116]. Pr_6O_{11} was considered as the stable form at room temperature. According to the calculations, the materials PrO_x-C contained about 22.0±0.7 wt% Pr_6O_{11} (Table X). However, the exact composition of PrO_x is unknown. There is a trend that the amount of PrO_x in PrO_x-C is slightly higher at increased calcination temperatures. This is probably caused by some inadvertent decomposition of carbon during calcination. As for PrO_x-C 300 the amount of carbon is close to the expected value, it proves that during the preparation of this material in air the carbon was not oxidised.

Table X. The composition of Pt-PrO_x-C materials calculated from thermogravimetry (TGA) and microwave plasma – atomic emission spectrometry (MP-AES) results.

Material	Method: TGA	Material	Method: TGA		Method: MP-AES	
	wt% of Pr_6O_{11}		wt% of Pr_6O_{11}	wt% of Pt	wt% of Pr_6O_{11}	wt% of Pt
PrO_x-C 300	21.5	Pt-PrO_x-C 300	18.4	14.6		
PrO_x-C 525	21.4	Pt-PrO_x-C 525	18.2	14.9	16.7	16.6
PrO_x-C 700	22.4	Pt-PrO_x-C 700	18.8	16.1	16.4	14.2
PrO_x-C 1100	22.7	Pt-PrO_x-C 1100	18.2	19.8	15.2	19.0
		Pt-C blank		16.3		15.1

The deposition of Pt onto the PrO_x-C materials using reduction of the H_2PtCl_6 complex with hydrogen was also studied using TGA. A sample of PrO_x-C 525 was impregnated with a solution of H_2PtCl_6 in ethanol. After impregnation, the sample was dried in a vacuum oven for 12 h at 50 mbar. Starting from 25 °C the sample started to lose weight (Fig. 14a). The initial weight loss was caused by the loss of crystallisation water. The decomposition of the $[PtCl_6]^{2-}$ complex started from 135 °C and the speed of deposition started to decrease from 190 °C towards higher temperatures. From the weight loss of the second step, approximate platinum content in the material received was calculated. About 80 wt% of the platinum precursor was decomposed during 50 min starting from the decomposition of the complex. It was concluded that 180 min at 200 °C is enough to deposit all platinum from the complex into the structure of the PrO_x-C materials.

This was also confirmed by burning of the carbon from the synthesised Pt-PrO_x-C catalysts (Fig. 14b). The decomposition of the catalysts started at 400 °C and proceeded in two steps. The carbon was burned off at 600 °C. A slight decrease in mass (about 1 wt%) also takes place at higher temperatures. Using the same assumptions as previously regarding the PrO_x-C materials, the phase composition of the catalysts was calculated (Table X). The Pt-PrO_x-C catalysts contained 18.4±0.3 wt% Pr_6O_{11} and the platinum amount somewhat increased from 14.6 to 19.8 wt% going from Pt-PrO_x-C 300 to Pt-PrO_x-C 1100. The atomic ratio of Pt and Pr was about 1 : 1.7 for materials Pt-PrO_x-C 300, Pt-PrO_x-C 525 and Pt-PrO_x-C 700; and slightly lower 1 : 1.3 for material Pt-PrO_x-C 1100.

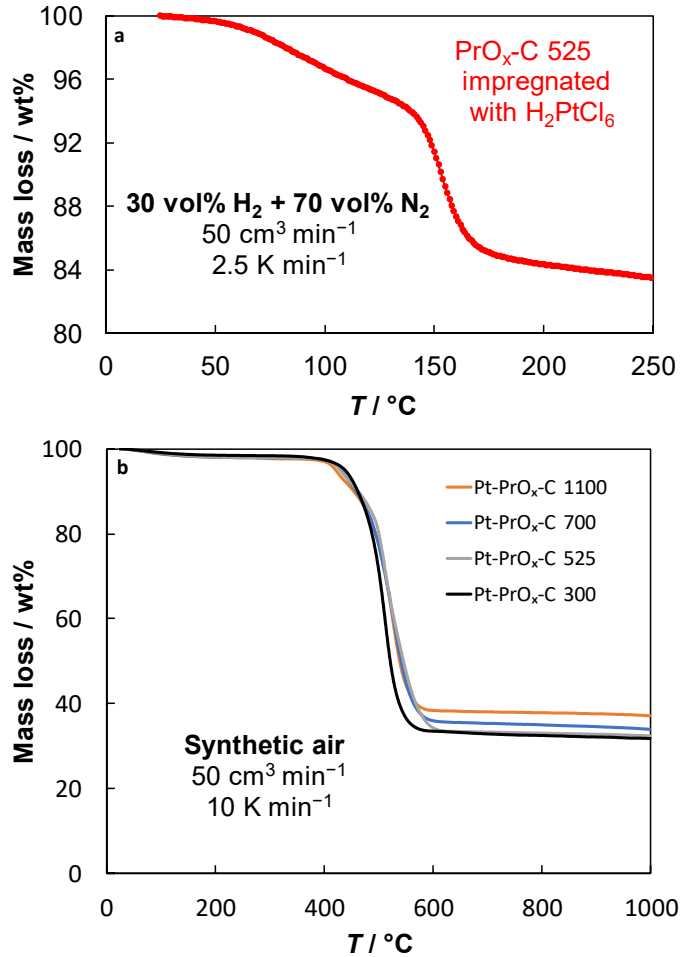

Figure 14. Thermogravimetry of (**a**) PrO_x-C 525 impregnated with H_2PtCl_6 in hydrogen and (**b**) materials Pt-PrO_x-C in synthetic air. The heating rate and gas flow rate is noted in figure.

6.7. Microwave plasma atomic emission spectroscopy

The results of MP-AES measurements are shown in Table X. Weight percentages of Pr_6O_{11} are calculated from the results of measurements of Pr as single element. Differences with the TGA results are rather small, below ±3%. However, the weight percentage of Pr_6O_{11} is consistently lower in case of MP-AES when compared to TGA results, which might arise from the difficulties of dissolving the catalyst material. However overall, the results of MP-AES and TGA are in good agreement.

6.8. Inductively coupled plasma mass spectrometry

ICP-MS was used to measure the content of molybdenum in the solutions of dissolved C(Mo_2C) + Mo_2C composite materials. Based on these results, the weight percentage of C(Mo_2C) in the composite materials was calculated assuming that all molybdenum was in the form of molybdenum carbide. The content of C(Mo_2C) in the composite materials is shown in Table XI. Although other methods of physical characterisation have shown the existence of other molybdenum compounds in the studied composite materials, their content was very low, and the error caused by these compounds is assumed to be irrelevant.

6.9. Electrochemical measurements data

6.9.1. Electrochemical characterisation of C(Mo_2C)+Mo_2C materials

6.9.1.1. Stability of C(Mo_2C)+Mo_2C materials

Although pure C(Mo_2C) is a very stable material with a wide region of ideal polarizability [117], reports on the stability of Mo_2C as a component of composite materials are somewhat conflicting, but ultimately indicate that Mo_2C dissolves from composite materials in acidic media [83,88–91].

The studied C(Mo_2C) + Mo_2C composite materials behaved similarly. To visualise the dissolution of molybdenum containing species, separate experiments were carried out at a very low potential sweep rate, but not used in the electrochemical measurements discussed later. Fig. 15a shows the very high anodic oxidation peak for material $C_{63\%}$, which we attribute to the oxidation of Mo_2C to $HMoO_4^-$. This is also supported by the appearance of gas bubbles on the electrode surface, which are most probably CO_2 and/or CO generated by the oxidation of carbidic carbon in Mo_2C [87]. At these low potential sweep rates, the currents arising from the dissolution of molybdenum containing species diminished rapidly with subsequent potential sweep cycles. Apparently the entire Mo_2C precursor is dissolved out from the composite material in the sulphuric acid solution at potentials less negative than −0.15 V vs. MSE.

During the electrode stabilisation “cycles” before electrochemical experiments, the electrode was submerged into the solution under a potential E = 0.1 V vs. MSE. Under these conditions most of the Mo_2C dissolved before the beginning of stabilisation “cycles”. Fig. 15b shows the j vs. E curves measured after the electrode (material $C_{63\%}$) had been in the solution for some minutes.

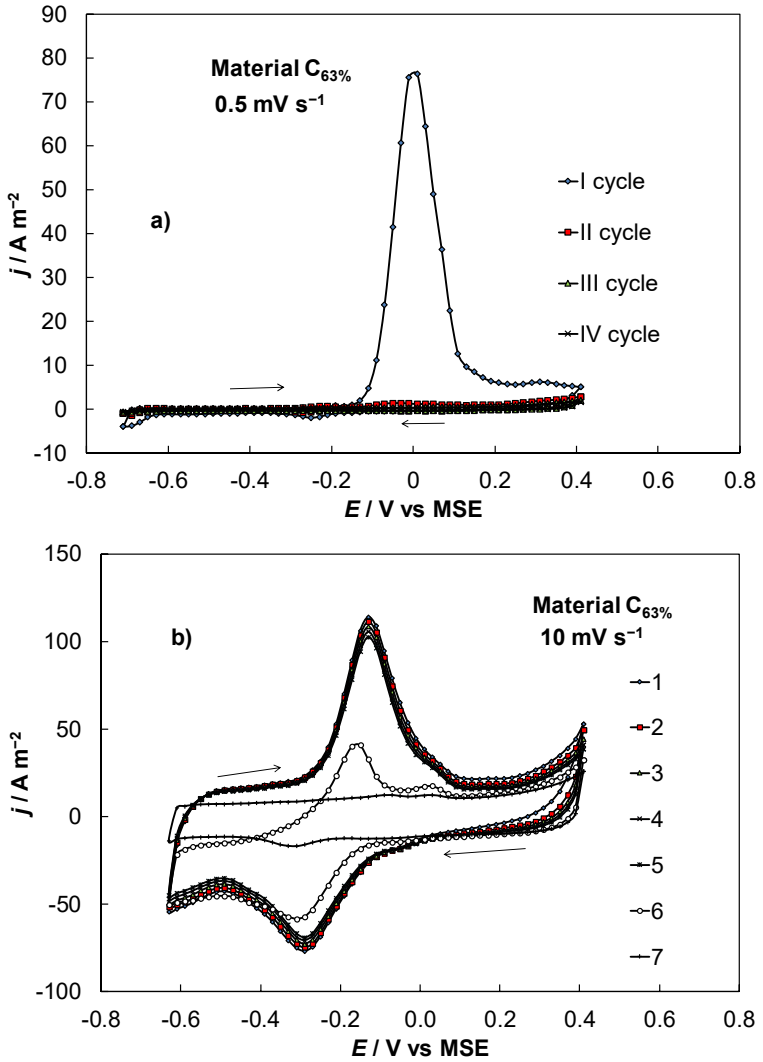

Figure 15. (a) Dissolution of Mo_2C from $C(Mo_2C)$ + Mo_2C composite material $C_{63\%}$ in 0.5 M H_2SO_4 solution at a potential sweep rate of 0.5 mV s^{-1} in an argon saturated solution. **(b)** The current density (j) vs. potential (E) curves measured during the stabilisation "cycles" for $C(Mo_2C)$ + Mo_2C composite material $C_{63\%}$ in 0.5 M H_2SO_4 solution using the RDE method. The electrode rotation speed was 800 revolutions per minute. The potential sweep rate was 10 mV s^{-1}. The curves are designated as follows: 1–5 correspond to the five j vs. E curves measured in the first "cycle" in an argon saturated solution, curve 6 corresponds to the fifth j vs. E curve measured during the second "cycle" (in an oxygen saturated solution), and curve 7 corresponds to the fifth j vs. E curve measured during the third "cycle" (again in an argon saturated solution).

The distinctive Mo_2C oxidation peak at $E = 0$ V vs. MSE is almost absent. Instead, the wide cathodic reduction and anodic oxidation peaks around $E = -0.3$ V and $E = -0.1$ V vs. MSE, respectively, are most probably caused by the redox equilibria between various molybdenum compounds (most probably in oxide forms) [118], most of which are intermediary products of the dissolution of Mo_2C. Although the peaks are quite persistent during the first stabilisation "cycle" in an argon-saturated solution, they rapidly decayed after switching to oxygen, as the dissolution products of Mo_2C are converted into soluble compounds which diffuse out of the porous structure. Usually after the second "cycle" in argon, all electrode materials attained the surface conditions and electrochemical behaviour characteristic of almost perfectly capacitive electrodes [119]. The "cyclings" in oxygen saturated solution helped to achieve the stable surface state more quickly.

The abovementioned processes occurred minimally in case of composite materials with low Mo_2C content. More importantly, for all electrodes, the cyclic voltammetry (CV) curves measured in the beginning of the experiment (after the end of the stabilisation "cycles") and at the end of the electrochemical measurements (8 hours later) are very similar, i.e., stationary currents are achieved, as would be expected of the studied materials.

6.9.1.2. Cyclic voltammetry measurements

The CV results are shown in Fig. 16 as gravimetric capacitance,

$$C = I/mv, \tag{11}$$

where m is the mass of material deposited onto the GCDE and I is the measured current. In case of materials with low Mo_2C content, the CV curves mostly exhibit the rectangular shape characteristic of capacitive electrodes [119]. At potentials more positive than $E = 0.2$ V vs. MSE, the carbon surface starts to oxidise. During the reverse scan the surface is reduced back. This reduction process does not have a separable peak but causes the increase of reduction current density. It transpires that higher content of C(Mo_2C) in these composite materials makes the surface more easily oxidisable, i.e., the oxidation peak at $E > 0.2$ V vs. MSE is more pronounced. This could hint towards the composite materials with higher carbon content having a higher number of active centres on the surface. This highlights the difference between chlorinating Mo_2C and dissolving it from the composite materials. During chlorination, only molybdenum is taken out of the materials, leaving highly active nanoscale carbon facets in the material, whereas dissolving Mo_2C from the studied composite materials only leaves larger pores with less active surface. There is an oxidation/reduction peak around $E = -0.2$ V vs. MSE that indicates a quinone/hydroquinone equilibrium on the surface [120]. In case of $C_{18\%}$ with a high Mo_2C content and very low surface area (and capacitance), the current peaks are more pronounced, but considering the low carbon content in this

material, it could be possible that these are caused by reversible oxidation/ reduction of molybdenum oxides within the porous structure. At potentials more negative than $E = -0.7$ V vs. MSE the slow water decomposition starts [25].

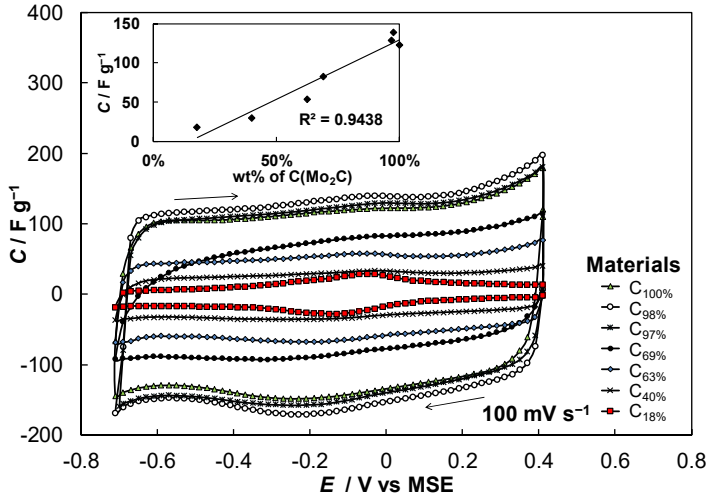

Figure 16. The dependence of gravimetric capacitance on the electrode potential for different $C(Mo_2C) + Mo_2C$ composite materials (the weight percentage of $C(Mo_2C)$ in $C(Mo_2C) + Mo_2C$ composite materials is marked in the legend), calculated from cyclic voltammetry data measured in 0.5 M H_2SO_4 solution saturated with argon. The potential sweep rate was 100 mV s^{-1}. The inset shows the dependence of gravimetric capacitance on the weight percentage of $C(Mo_2C)$ in $C(Mo_2C) + Mo_2C$ composite materials at potential $E = 0.1$ V vs. MSE.

Table XI. The dependence of specific capacitance of $C(Mo_2C) + Mo_2C$ composite materials in 0.5 M H_2SO_4 solution, saturated with argon, on the content of $C(Mo_2C)$ in the $C(Mo_2C) + Mo_2C$ composite materials.

Material	C wt% [(1)]	C_{CV} / F g^{-1} [(2)]	C_S / F g^{-1} [(3)]	C_P / F g^{-1} [(3)]
$C_{100\%}$	100%	123	120	118
$C_{98\%}$	98%	139	138	137
$C_{97\%}$	97%	129	117	116
$C_{69\%}$	69%	83	73	72
$C_{63\%}$	63%	54	50	50
$C_{40\%}$	40%	30	28	28
$C_{18\%}$	18%	18	15	15

[(1)] C wt% shows the weight percentage of $C(Mo_2C)$ in the $C(Mo_2C) + Mo_2C$ composite materials, calculated from ICP-MS measurements.
[(2)] The gravimetric capacitance values C_{CV} have been calculated from CV data at $E = 0.1$ V vs. MSE at potential sweep rate $v = 100$ mV s^{-1}.
[(3)] The values of series and parallel capacitances (C_S and C_P respectively) have been calculated from electrochemical impedance spectroscopy data at $E = 0.1$ V vs. MSE at ac frequency $f = 10$ mHz.

The capacitance values calculated from CV data are shown in Table XI and are in good accord with impedance data. With the increase of Mo_2C content in the $C(Mo_2C) + Mo_2C$ composite materials, the capacitance values decrease as the specific surface area drops drastically. Although $C_{98\%}$ and $C_{97\%}$ have a slightly higher capacitance than $C_{100\%}$, the capacitance values are in good accord with specific surface area data given in Table VII. The increase in capacitance correlates well with the increase of carbon content in the $C(Mo_2C) + Mo_2C$ composite materials. However, as most of the Mo_2C is dissolved during the stabilisation process in the beginning of the experiment, the dependence of capacitance on the carbon content is not quite linear (inset in Fig. 16). As discussed earlier, dissolution of Mo_2C from the composite materials might result in a slightly changed porous structure. As such, the specific surface area of the composite materials measured by low temperature N_2 sorption is probably not quite the same as the surface area of the material on the electrode in solution after electrochemical stabilisation. However, due to the minuscule amount of the composite materials deposited onto the electrodes, determination of specific surface area after electrochemical measurements is not feasible.
Another aspect to note is the higher capacitance values of $C_{98\%}$ and $C_{97\%}$ compared to $C_{100\%}$ (Table XI). This is probably also caused by the dissolution of Mo_2C from the composite materials. Due to the very small amount of Mo_2C in the materials (especially volumetrically), the electrochemical stabilisation of $C_{98\%}$ and $C_{97\%}$ could result in higher specific surface area on the electrode in solution, compared to during N_2 sorption measurements.

Electrochemically, the materials behave similarly, so molybdenum containing species have a very limited influence on the j vs. E dependencies. It also indicates that the properties of the synthesised carbon do not change substantially during the stepwise chlorination process. This is in agreement with N_2 sorption measurements (Fig. 6), Raman spectroscopy (inset in Fig. 9) and HRTEM (Fig. 12) data.

The cyclic voltammograms measured at different potential sweep rates coincide well and are shown in Fig. 17 for material $C_{63\%}$. The wide current peak seen at $E = -0.2$ V vs. MSE does not depend on the potential sweep rate and the charge (calculated through integration) under anodic and cathodic peaks is equal, indicating nearly reversible redox processes at carbon electrode interface. At more positive potentials than $E = 0.2$ V vs. MSE, the capacitance increases with decreasing electrode potential sweep rate, indicating that the oxidation of the electrode surface is a mixed kinetics process at these potentials.

The dependencies of current density on potential sweep rate in logarithmic scale (inset A in Fig. 17) are linear at different potentials and the slope value is around unity, except at vertex potentials. This indicates that the electrode behaves capacitively in almost the whole region of potentials studied, and that the peak around $E = -0.2$ V vs. MSE is caused by the reversible oxidation and reduction of surface functional groups, i.e., mainly by the quinone/hydroquinone redox process equilibrium. The intercept of these dependencies is nearly constant, demonstrating that the capacitance depends very weakly on the

potential. The log j vs. log v dependencies (inset B in Fig. 17) are also linear for different electrode materials at constant potential and the intercepts describe the capacitive behaviour following the same trend as the data shown in Table XI.

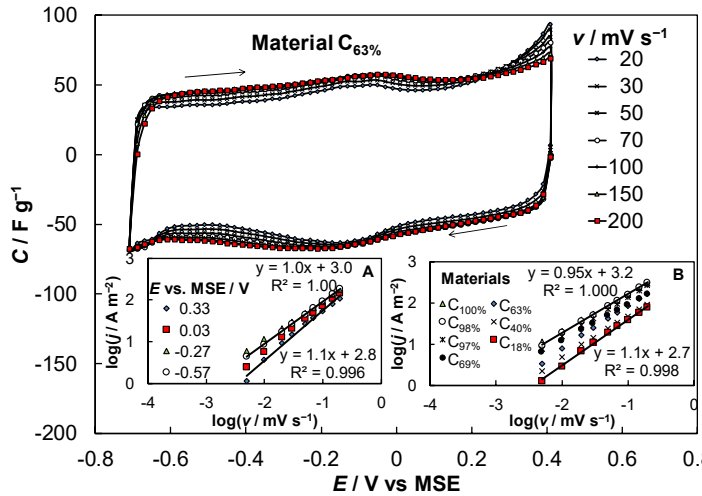

Figure 17. The dependence of gravimetric capacitance on the electrode potential for different potential sweep rates (marked in the legend) for C(Mo_2C) + Mo_2C composite material $C_{63\%}$, calculated from cyclic voltammetry data measured in 0.5 M H_2SO_4 solution saturated with argon. Insets show the dependence of current density on the potential sweep rate in logarithmic scale for C(Mo_2C) + Mo_2C composite material $C_{63\%}$ at four different potentials (marked in the legend) (**A**) and for different C(Mo_2C) + Mo_2C composite materials (marked in the legend) at potential E = −0.1 V vs. MSE (**B**).

6.9.1.3. Electrochemical impedance spectroscopy

The Bode plots (phase angle (φ) vs. log f and impedance modulus ($|Z|$) vs. log f plots) and Nyquist plots (Z'' vs. Z' plots) measured during the electrode stabilisation "cycles" of material $C_{63\%}$ are shown in Fig. 18a and Fig. 18b, respectively. The following equations were used:

$$\tan \varphi = Z''/Z' \quad (12)$$

$$|Z|^2 = (Z')^2 + (Z'')^2 \quad (13)$$

The first measured impedance spectrum differs from the later spectra. At lower frequencies the phase angle is about −80°. The dependence of phase angle on frequency has a different shape at medium frequencies ($f \approx$ 10 Hz ... 300 Hz) which is caused by diffusional mass transport limitations inside the pores [121]. Nyquist plots (inset in Fig. 18b) show the same effect, as the slope has an angle of −45° in a wider frequency range and does not become vertical at lower frequencies. The Nyquist plots measured during the second and later "cycles" coincide. The phase angle reaches −86° and diffusional limitations are not

pronounced. The behaviour of Bode and Nyquist plots are controlled by the charging and discharging of carbon surface. The electrolyte resistance (R_s) determined from the high frequency region of Nyquist plots (inset in Fig. 18b) is the same for both argon and oxygen saturated solutions.

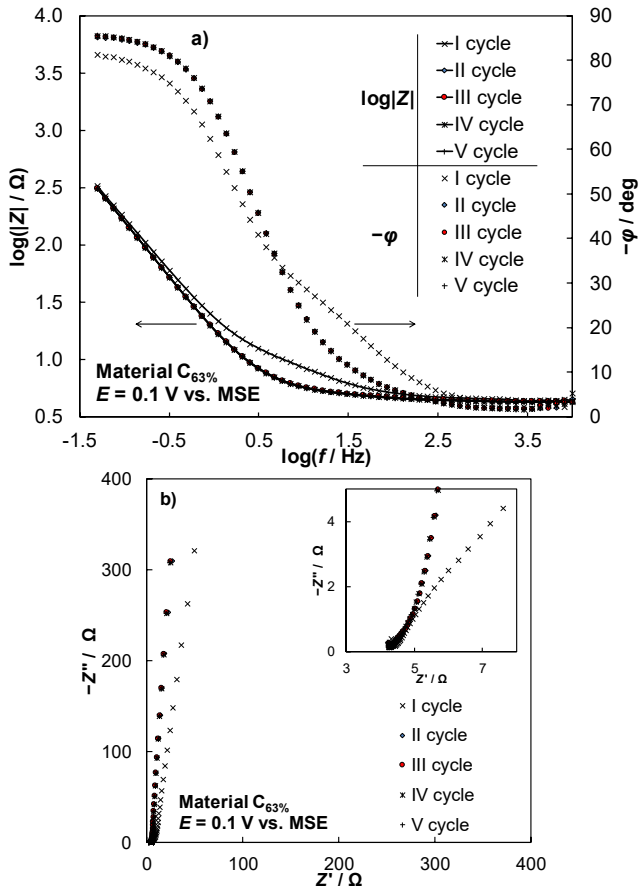

Figure 18. Impedance spectra measured during the stabilisation "cycles" for the $C(Mo_2C) + Mo_2C$ composite material $C_{63\%}$ in 0.5 M H_2SO_4 solution at potential $E = 0.1$ V vs. MSE. "Cycles" I, III, V were measured in an argon saturated solution and "cycles" II and IV in an oxygen saturated solution. (**a**) Bode plots and (**b**) Nyquist plots. High frequency area is magnified in the inset of (**b**).

Fig. 19 shows the electrochemical impedance spectroscopy (EIS) data for different materials at potential $E = 0.1$ V vs. MSE in argon saturated solution after the electrodes had been stabilised. All materials exhibit capacitive behaviour. At lower frequencies the absolute value of the phase angle $|\varphi|$ is over 82° and the Nyquist plots are almost parallel with the imaginary axis (Z''). At high frequencies, the Nyquist plots coincide well (inset in Fig. 19b), i.e., the

R_s does not depend on the carbon content in the composite material and is between 3.5 Ω and 4.5 Ω.

The Bode plots (Fig. 19a) show that as the carbon content increases, the change from resistive behaviour ($\varphi = 0°$) to capacitive behaviour ($\varphi = -90°$) shifts towards lower frequencies. This is caused by the increase of the time constant:

$$\tau = R_s C_{edl} \tag{14}$$

As the electrolyte resistance is almost constant, the increase in the time constant by about one magnitude is caused by the increase of capacitance.

The impedance spectra measured at different potentials 0.4 V, 0.1 V, −0.3 V and −0.5 V vs. MSE (not shown for brevity) coincide well, except at potential $E = 0.4$ V vs. MSE, where oxidation of the carbon surface occurs. This indicates that the behaviour of the materials is mostly determined by the charging and discharging of the carbon surface. The electrolyte resistance is independent of potential.

The dependence of series and parallel capacitances (C_S and C_P) on the frequency is shown in Fig. 20. The following equations were used [15,121–123]:

$$C_S = -1/(2\pi f Z'') \tag{15}$$
$$C_P = -Z''/(2\pi f |Z|^2) \tag{16}$$

At low frequencies C_S and C_P curves coincide, as is expected of capacitive electrodes. The calculated series and parallel capacitance values at $f = 10$ mHz are shown in Table XI. Material $C_{98\%}$ has slightly higher capacitance, but materials $C_{100\%}$ and $C_{97\%}$ with similar specific surface area, have comparable capacitance values.

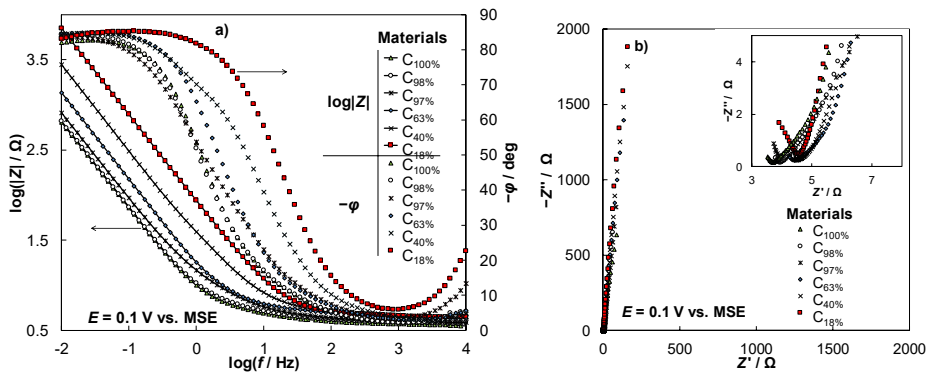

Figure 19. Impedance spectra measured after stabilisation for different $C(Mo_2C) + Mo_2C$ composite materials (wt% of $C(Mo_2C)$ in $C(Mo_2C) + Mo_2C$ composite materials marked in legend). Measurements were performed in 0.5 M H_2SO_4 solution saturated with argon at potential $E = 0.1$ V vs. MSE. (**a**) Bode plots and (**b**) Nyquist plots. High frequency area is magnified in the inset of (**b**).

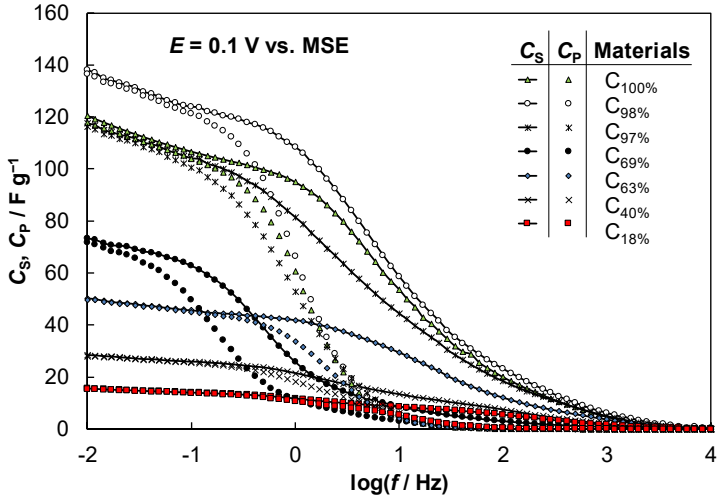

Figure 20. The dependence of series (C_S) and parallel (C_P) capacitance on frequency, calculated from electrochemical impedance spectroscopy data measured for different $C(Mo_2C) + Mo_2C$ composite materials (wt% of $C(Mo_2C)$ in $C(Mo_2C) + Mo_2C$ composite materials marked in legend). Measurements were performed in 0.5 M H_2SO_4 solution saturated with argon at potential $E = 0.1$ V vs. MSE.

6.9.2. Electrochemical characterisation of Pt-C(Vulcan) and Pt-C(Mo_2C) materials

6.9.2.1. Determination of Pt mass percentage

The content of Pt in the synthesised catalysts was determined using electrochemical dissolution of Pt in deaerated 6M HCl solution.

The amount of deposited Pt was highest for materials 1 and 2 (Table XII), which were deposited in an acidic reaction mixture. In the case of Vulcan based catalysts, the Pt content was always lower than 20% in alkaline reaction mixtures. This could be explained using the point of zero charge (PZC) of the support [124]. The pH value of the suspension at PZC is such that the surface charge is zero. For Vulcan XC72 the pH at PZC is equal to about 7 [125]. At pH = 2, the surface of Vulcan carbon is positively charged and it enables the strong electrostatic adsorption of negatively charged $[PtCl_6]^{2-}$ anions, i.e. the deposition of Pt is facilitated. On the other hand, at pH from 12 to 13, the $[PtCl_6]^{2-}$ anions are repelled from the negatively charged carbon surface and the resulting loading of Pt is less than expected. However, in alkaline conditions, the crystallite size of the deposited Pt nanoclusters is two to four times smaller (Table V) and hence the ECSA is higher. The oxidation of Vulcan in nitric acid causes the functionalisation of carbon surface with oxygen containing groups and further decreases the pH value at PZC. As the electrostatic repulsion of the $[PtCl_6]^{2-}$ anions from the negatively charged surface of Vulcan* was even higher at pH ≈ 13, the Pt loading was lowest for this material.

Remarkably, for the C(Mo_2C) based material, nearly nominal loading of Pt was achieved. While the PZC of the catalyst support C(Mo_2C)750 °C is unknown, it seems to be higher compared to Vulcan XC72. It is possible that the very high S_{BET} (Table VII and Table VIII) also has an influence on the amount of Pt deposited onto the material.

6.9.2.2. Cyclic voltammetry measurements

The cyclic voltammograms given in Fig. 21, represented as gravimetric capacitance, C_{CV}, show behavior characteristic of Pt-decorated carbon materials. There are two distinct regions corresponding to hydrogen adsorption/desorption and oxygen adsorption/desorption. Between these regions there is a so-called edl region. The gravimetric capacitance almost does not depend on the electrode potential sweep rate (Fig. 21a). The C_{CV} values and the shapes of C_{CV}, E-plots (Fig. 21b) depend noticeably on the electrode material under study. The highest hydrogen adsorption/desorption ($H_{ads/des}$) peaks were calculated for materials 3–5, i.e., adsorption/desorption kinetics and ECSA is highest with Pt nanoparticles deposited at pH = 12.3-12.5 and with small to medium $H_2PtCl_6{\times}6H_2O$ concentration. For these materials the dispersion of the Pt nanoparticles is also very high (c.f. Table V). For materials synthesised at low pH, i.e., catalysts 1 and 2, the peaks are not very well developed and the dispersion of Pt is low. The highest C_{CV} values within the so-called edl region were measured for the Pt-C(Mo_2C) (material 8). For materials deposited onto Vulcan and Vulcan*, the capacitance is about two times lower in this region caused by the much lower specific surface area (Table VIII) compared to C(Mo_2C). In the region of $H_{ads/des}$ the capacitance was integrated to get the total charge from which the charge of edl charging/discharging was subtracted to get hydrogen adsorption and desorption charges [126]. These values were used to estimate the ECSA values (Table XII). Material no. 5 had the highest ECSA value (94 m^{-2} g^{-1}) i.e., high reaction mixture pH and moderately high concentration of $H_2PtCl_6{\times}6H_2O$ enable the formation of smaller Pt nanoparticles.

6.9.2.3. Oxygen reduction reaction measurements

The RDE data measured for all the studied materials are given in Fig. 22a. The values of diffusion limiting current density, j_d, are in agreement with theoretical values for most materials. However, the values of j_d for materials no. 2 and 7 are somewhat lower, possibly because the catalyst layers deposited on electrodes were not uniform. The dispersion of the catalyst particles in the deposition suspension depended also on the synthesis conditions. The values of half-wave potential, $E_{1/2}$, do not depend noticeably on the material, except for the Pt-C(Vulcan*). For the other materials, the average value of $E_{1/2}$ is about 0.86 V vs. RHE. Thus, treatment of the surface of the commercial Vulcan XC72 carbon support with HNO_3 acid did not improve the electrochemical activity of the Pt-nanoclusters decorated material.

Table XII. Summary of electrochemical parameters calculated from CV and RDE measurements data for Pt-C(Vulcan) and Pt-C(Mo_2C) materials as noted in Table II.

Material	Pt wt%	ECSA / $m^2\ g^{-1}$	j_d / A m^{-2}	MA at 0.9 V / mA mg^{-1}	SA at 0.9 V / µA cm^{-2}
1	23.7 ± 2.1	20 ± 3	-60.33 ± 1.46	161 ± 31	822 ± 81
2	21.2 ± 3.2	21 ± 3	-57.04 ± 0.12	155 ± 14	792 ± 56
3	13.6 ± 2.1	82 ± 10	-60.17 ± 0.54	348 ± 50	428 ± 45
4	14.7 ± 2.4	83 ± 13	-60.22 ± 0.44	348 ± 36	424 ± 33
5	12.8 ± 2.7	94 ± 13	-60.22 ± 0.29	385 ± 92	449 ± 54
6	16.4 ± 2.8	72 ± 14	-59.58 ± 0.32	242 ± 61	336 ± 31
7	8.6 ± 3.2	34 ± 11	-57.46± 0.18	136 ± 45	477 ± 37
8	18.4 ± 2.8	52 ± 13	-59.43 ± 0.19	255 ± 82	439 ± 19

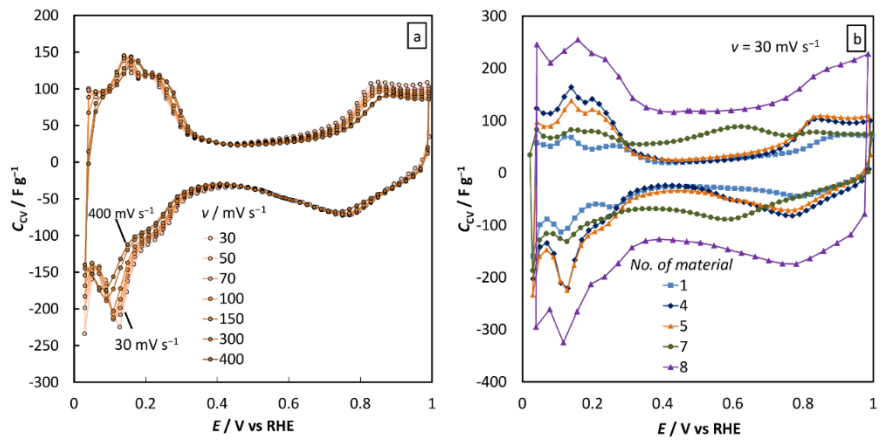

Figure 21. Calculated gravimetric capacitance, C_{CV}, vs. potential, E, plots for (**a**) Pt-C(Vulcan) material 5 at different potential scan rates (noted in figure) and (**b**) different materials (notation of materials given in Table II) in 0.1M $HClO_4$ solution saturated with N_2 at potential scan rate 0.03 V s^{-1}.

The RDE data for the deposited catalyst layers can be analyzed using the so-called two layers model, which takes into account the diffusion in the electrolyte boundary-layer and in the Nafion film [22,99,100,126–128]:

$$\frac{1}{j_c} = \frac{1}{j_{kin}} + \frac{1}{j_f} + \frac{1}{j_d} \tag{17}$$

where j_c is current density corrected for the edl charging currents, j_{kin} is kinetic current density, j_f is film diffusion limited current density and j_d is diffusion

limited current density. Since the thickness of Nafion layer in the electrode was small and the calculated film diffusion limited current density was high, i.e. the diffusion of the O_2 molecules in the Nafion layer was not the limiting step [117], it was assumed that the RDE data can be analyzed by applying the classical Koutecky-Levich equation to calculate the kinetic current densities [22,127,129]:

$$j_{\mathrm{kin}} = \frac{j_{\mathrm{L}} j_{\mathrm{c}}}{j_{\mathrm{L}} - j_{\mathrm{c}}}, \tag{18}$$

where j_{L} is the measured limiting current density. Based on the data in Table XII, catalytically the most active material was material no. 5 with the highest value of ECSA, mass activity and quite high specific activity.

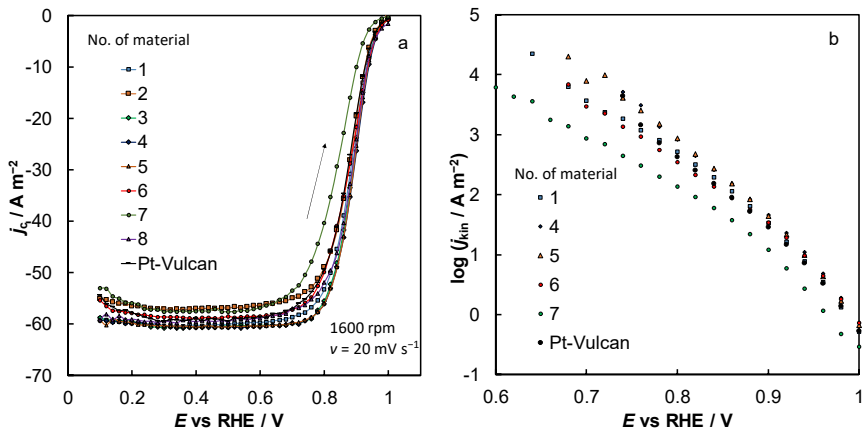

Figure 22. Rotating disc electrode data (corrected with background current densities) from positive-going sweeps at 0.02 V s^{-1} (**a**) j_c, E-plots at 1600 rev min^{-1} and (**b**) Tafel-like plots for different materials (notation of materials given in Table II) in 0.1 M $HClO_4$ O_2-saturated solution.

Tafel-like plots are shown in Fig. 22b, applying j_{kin} values obtained using Eq. 18. The Tafel-like plots indicate that there are two nearly linear regions with slope values −58 ± 5 mV dec^{-1} (low current density region) and −93 ± 11 mV dec^{-1} (high current density region). The values of slopes do not depend on material, thus the mechanism and limiting steps for different materials are the same within these fixed current density regions (i.e., at low and high current density regions, respectively).

6.9.2.4. Electrochemical impedance spectroscopy

Electrochemical impedance spectroscopy data, given in Fig. 23a, show nearly ideal capacitive behavior for all materials at low *ac* frequencys $f < 0.1$ Hz in N_2

saturated solution. The high frequency series resistance, R_s, values are practically independent of the catalyst material (i.e., material synthesis conditions applied) under study. The value of R_s varies from 2.6 Ω (Pt-C(Vulcan*) to 4.2 Ω (Pt-C(Vulcan) synthesised at pH = 2). The values of series capacitance (C_s) and parallel capacitance (C_p) were calculated from EIS data using Eq. 15 and 16, respectively, and are given in Fig. 23b. The materials 7 (Pt-C(Vulcan*)) and 8 (Pt-C(Mo_2C)) exhibit the highest values of capacitance at $f \rightarrow 0$ (~70 F g^{-1} for material 7 and ~112 F g^{-1} for material 8). All the other materials under study have rather low capacitance values ranging from 13 to 19 F g^{-1}.

Thus, in addition to PEMFC electrodes, the Pt-C(Mo_2C) and Pt-C(Vulcan*) materials could be used as electrodes for combined hybrid (pseudocapacitive) supercapacitors, i.e., for combined energy conversion/storage device.

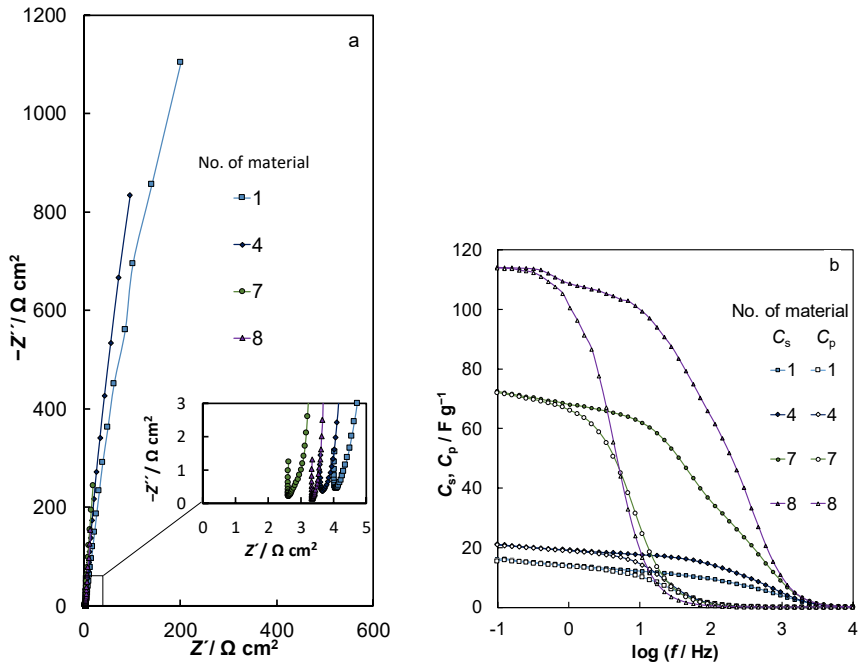

Figure 23. (**a**) Nyquist plots and (**b**) C_s, log f- and C_p, log f-plots for different materials (noted in Table II) in 0.1 M $HClO_4$ N_2-saturated solution at E = 0.45 V vs RHE.

6.9.3. Electrochemical characterisation of Pt-rare-earth metal oxide based materials

6.9.3.1. Platinum dissolution profiles of Pt-CeO_2-C materials

For detailed analysis of the weight of Pt deposited, the electrochemical dissolution of Pt followed by quantitative analysis has been conducted.

The dissolution of platinum from the studied catalysts in 6 M HCl is visualised in Fig. 24. There are one or two characteristic current peaks for every studied material. The dissolution peak potential correlates with the crystallite size (Table VI). The catalysts with smaller crystallite sizes also tend to dissolve at less positive potentials. The dissolution peak is almost absent for materials with big crystallites, i.e., for materials EG-6 and EG-7 ($d_{XRD} > 8$ nm). The catalysts EG-4 (two peaks), EG-6 and IWI-1 (peaks with shoulder) have also very sharp XRD maxima which indicates that the material consists of several crystallites. In agreement with X-ray data, the dissolution overpotentials of different crystallites are also different.

The Pt dissolution peaks were integrated to find out the weight percentage of platinum deposited onto the catalysts (Table III). Generally, the platinum content was lower than the nominal (assumed) value. In microwave assisted method the platinum content was higher for materials which were synthesised at pH > 12. Very good results were also achieved if hydrogen was used as the reducing agent. Applying sodium borohydride method, about 75% of platinum was successfully deposited onto the porous carbon support.

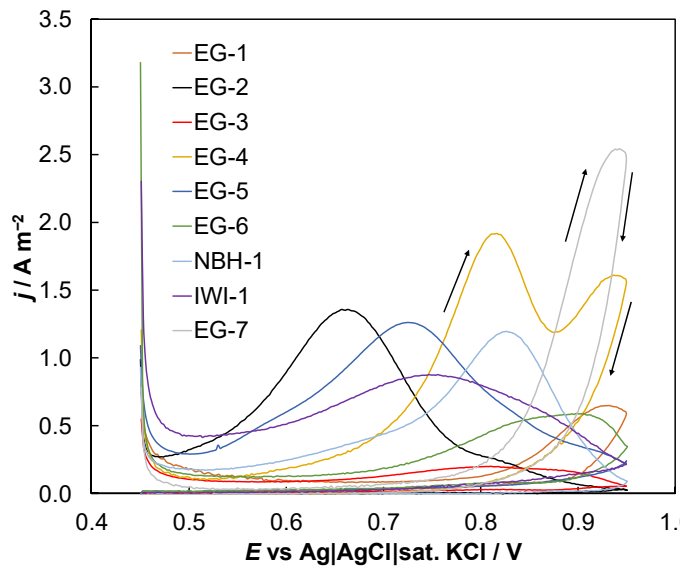

Figure 24. The anodic dissolution currents of Pt (first potential sweep) from the Pt based Pt-CeO_2-C catalyst electrode surface in 6 M HCl solution at potential sweep rate 1 mV s^{-1}.

6.9.3.2. Cyclic voltammetry of Pt-CeO_2-C materials

The characteristic cyclic voltammograms (presented as gravimetric capacitance, electrode potential, *C* vs. *E* curves) at different potential sweep rates measured in an argon saturated 0.5 M H_2SO_4 solution are given in Fig. 25a, using the material EG-4 as an example. The different characteristic regions are visible. The hydrogen adsorption-desorption peaks in the potential range from −0.675 V to −0.35 V, the so-called electrical double-layer (edl) area from −0.35 V to roughly 0 V and the oxidation of Pt particles and the subsequent reduction back to Pt from 0 V to 0.3 V [130] are seen in Fig. 25a.

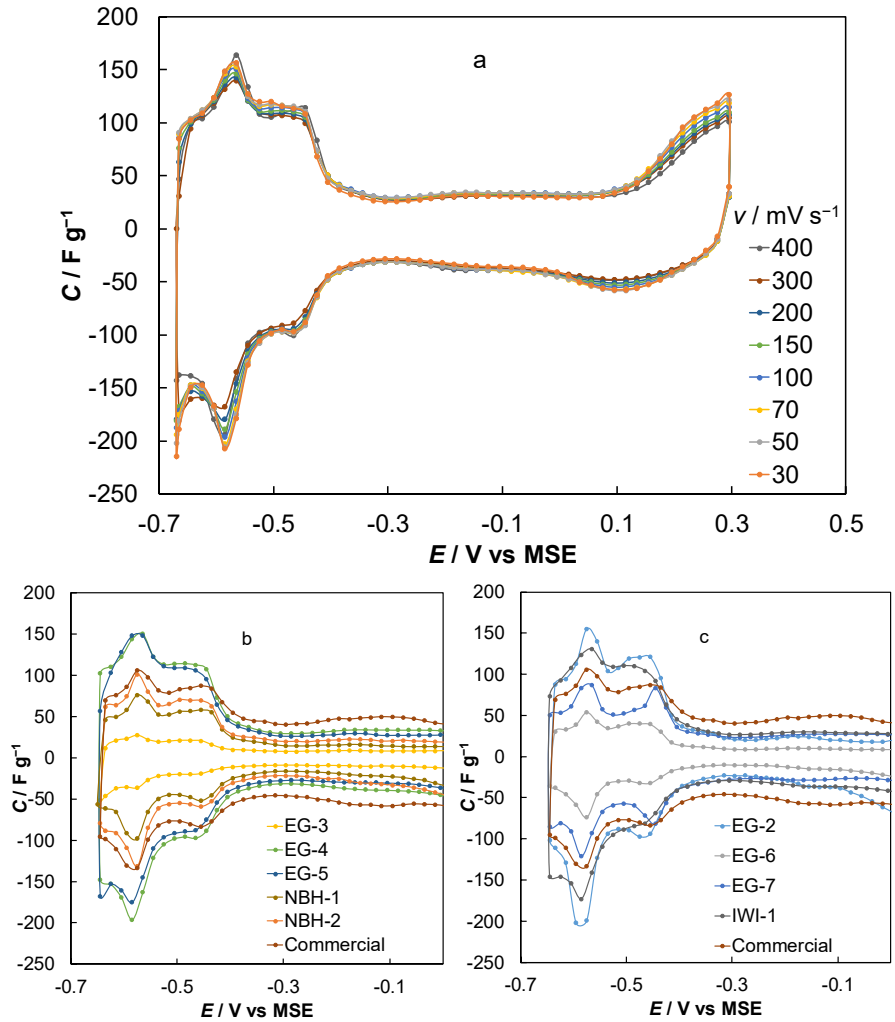

Figure 25. Cyclic voltammograms (calculated as gravimetric capacitance) of **(a)** catalyst EG-4 at different scanning rates, *v*, (noted in figure) in 0.5 M H_2SO_4 argon saturated solution, and **(b)** and **(c)** (divided for clarity) of studied Pt-CeO_2-C catalysts (noted in figure) at constant scanning rate (100 mV s^{-1}) in argon saturated 0.5 M H_2SO_4 solution.

Figs 25b and 25c show the *C*, *E*-curves for the studied material at one constant potential sweep rate. The figure is magnified to show the $H_{ads/des}$ and edl regions. It is visible that the commercial Pt-Vulcan material has the highest gravimetric capacitance in the edl region, whereas EG-3 and EG-6 have the lowest gravimetric capacitance. The rest of the materials exhibit rather similar gravimetric capacitance values, however, it must be noted, that NBH-1 has a slightly lower capacitance value than NBH-2. The material EG-1 exhibited very low electrochemical activity and is not shown in the figures.

Most of the materials exhibit sharp peaks at around −0.58 V vs. MSE and the highest peaks are in case of materials EG-2, EG-4, EG-7, and IWI-1. For some materials, another peak or shoulder is also distinguishable. The peaks were integrated to calculate ECSA and the diameter of spherical Pt nanoparticles as discussed in literature [131]. The results are given in Table XIII. The lowest ECSA was calculated in case of EG-7, synthesised in acidic conditions. EG-2, synthesised in basic conditions using the microwave synthesis method, has the highest ECSA, followed by IWI-1, synthesised using H_2 as the reducing agent.

In comparison to the dimensions of Pt crystallites calculated using the Scherrer equation from the XRD data (Table VI), the diameters calculated from CV data are slightly larger. EG-6 is the only material, where the Scherrer equation gives a larger Pt particle diameter than that calculated from CVs. The materials with the highest ECSA (EG-2 and IWI-1) have the smallest difference in the diameters of the Pt particles calculated using different methods, indicating a more uniform dispersion of the Pt nanoparticles on the carbon support. The rest of the materials most probably have less uniform particle sizes including both very small and very large Pt agglomerates, which the two methods take into account differently.

Table XIII. Calculated parameters from electrochemical measurement data for Pt-CeO_2-C materials.

Material	ECSA / $m^2\ g^{-1}$	d_{CV} / nm	i_{chron} / A g_{Pt}^{-1}	i_{max} / A g_{Pt}^{-1}	i_{ECSA} / mA cm_{Pt}^{-2}
EG-2	79.1	3.5	1.108	352	0.45
EG-3	37.9	7.5	0.188	192	0.51
EG-4	35.1	8.0	0.331	240	0.68
EG-5	45.2	6.2	0.414	279	0.62
EG-6	52.6	5.3	0.771	257	0.49
EG-7	22.3	12.8	0.220	275	1.23
NBH-1	37.3	7.5	0.279	131	0.35
NBH-2	30.1	9.3	0.683	164	0.54
IWI-1	60.7	4.6	0.638	324	0.53
Comm.	29.0	9.6	0.211	210	0.72

i_{chron} chronoamperometry current after 1800 s at potential $E = -0.2$ V vs. MSE *
i_{max} maximum gravimetric peak current of anodic scan *
i_{ECSA} peak current density of anodic scan normalised to ECSA *
* measured in 1 M CH_3OH + 0.5 M H_2SO_4 solution saturated with argon

6.9.3.3. Cyclic voltammetry of Pt-PrO$_x$-C materials

Cyclic voltammograms of the synthesised materials measured in 0.5 M H_2SO_4 solution saturated with argon are shown in Fig. 26. Different characteristic regions are visible. In the potential region from −0.67 V to −0.3 V hydrogen adsorption-desorption peaks are visible. The so-called electrical double layer (edl) area is visible in the region from −0.3 V to 0 V. The oxidation / reduction of Pt particles is visible the region from 0 V to 0.3 V. At around E = −0.2 V vs. MSE, a shallow wide peak can be seen, which could be attributed to reversible oxidation and reduction of surface oxygen groups on the carbon support (such as for example the quinone-hydroquinone redox couple) [132].

The Pt-C blank material differs from the Pt-PrO$_x$-C materials, as the vertex potential −0.67 V vs. MSE is slightly too negative for the material, and the hydrogen evolution reaction starts to occur. The Pt-C blank material also exhibits slightly higher currents in the edl area, as well as higher $H_{ads/des}$ peaks compared to the Pt-PrO$_x$-C materials. The Pt-PrO$_x$-C materials behave very similarly to each other, with some minor differences in the current densities. The $H_{ads/des}$ peak currents slightly increase with increasing calcination temperature of the support material. The materials calcined at 700 and 1100 degrees have a more pronounced hydrogen peak at around −0.5 V compared to the materials calcined at lower temperatures. This might indicate that the calcination also affects the carbon support in a way that allows for better dispersion of Pt nanoclusters in the subsequent deposition of Pt.

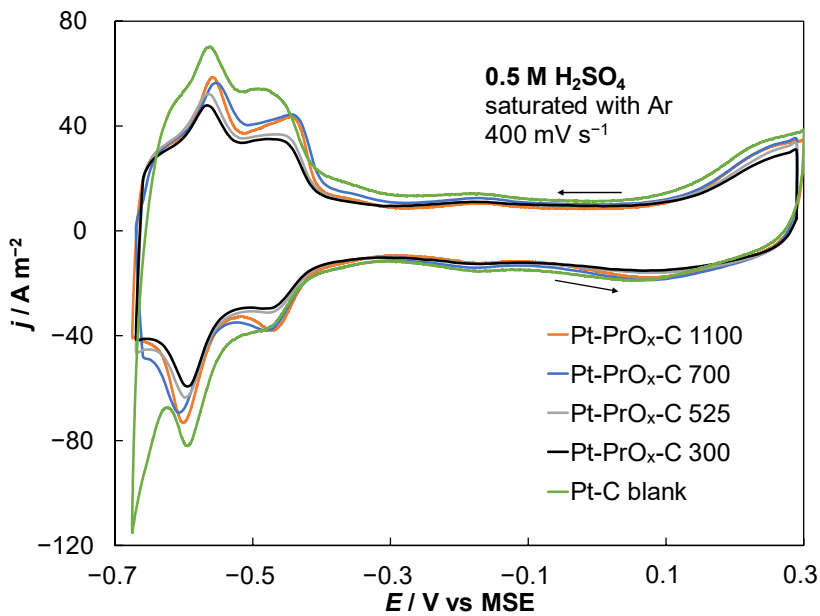

Figure 26. Cyclic voltammograms for different materials (noted in figure) measured in 0.5 M H_2SO_4 solution saturated with argon. The potential sweep rate is noted in figure. The current densities are given with regard to the geometric surface area of the electrode.

The hydrogen adsorption/desorption peaks measured at various potential sweep rates were integrated to calculate the ECSA and the diameter of spherical Pt nanoparticles as described in the literature [131]. The results are shown in Table XIV, and data for a Pt-CeO_2-C (IWI-1) material are shown for comparison. The results for the synthesised materials are rather similar overall, with Pt-PrO_x-C 525 having the lowest ECSA. The diameter of the Pt particles calculated from CVs is somewhat larger than those calculated from XRD data using TOPAS software. In addition to the inherent differences between the two methods, this could be due to the conditioning of the electrodes at the beginning of the measurements influencing the Pt cluster size, or potentially the effect of the chlorine residue as detected in some of the physical characterisation methods. However, as no chlorine was present in the Pt-C blank material, which has a very similar ECSA to the other materials, this does not seem to be the case. The praseodymium oxide does not seem to affect the shape of the CVs.

Table XIV. Parameters calculated from electrochemical measurements and X-ray diffraction data for Pt-PrO_x-C materials.

Material	ECSA / $m^2\ g^{-1}$	d_{CV} / nm	d_{XRD} / nm	i_{max} / A g_{Pt}^{-1}	j_{max} / mA cm^{-2}	i_{ECSA} / mA cm_{Pt}^{-2}
Pt-PrO_x-C 300	52	5.6	1.8	320	4.59	0.62
Pt-PrO_x-C 525	45	6.2	0.8 [1] 5.0 [1]	313	5.63	0.69
Pt-PrO_x-C 700	52	5.4	(0.9) [2]	323	5.51	0.62
Pt-PrO_x-C 1100	58	4.9	(1.6) [2]	331	5.95	0.57
Pt-CeO_2-C	61	4.6	1.9	324	4.37	0.53
Pt-C blank	55	5.1	1.3	234	4.21	0.42
Pt-C commercial	29	9.6	5.6	210	2.85	0.72

[1] Calculations indicated a bi-modal crystallite size distribution for Pt-PrO_x-C 525.
[2] Crystallite sizes in brackets are as calculated by Topas software, but most probably have a large error as described in the text.
i_{max} maximum gravimetric peak current of anodic scan *
j_{max} peak current density of anodic scan*
i_{ECSA} peak current density of anodic scan normalised to ECSA *
* measured in 1 M CH_3OH + 0.5 M H_2SO_4 solution saturated with argon

6.9.3.4. Methanol oxidation reaction on Pt-CeO_2-C materials

The results of CV measurements in 0.5 M H_2SO_4 + 1 M CH_3OH solution are shown in Fig. 27. The highest currents for methanol oxidation are seen in case of EG-2 (with the highest ECSA). The positive-going sweep exhibits a high, two-humped peak with a main maximum at 0.2 V vs. MSE. The negative-going sweep shows higher currents, with the peak potential roughly coinciding with the potential of the first hump ($E \approx 0.05$ V vs MSE) in the positive-going sweep. The materials EG-5 and EG-7 have similar current values. The material EG-6 has a similar anodic peak current value but inferior cathodic peak current as well as higher methanol oxidation overpotential.

The commercial catalyst material has a somewhat different *i* vs. *E* curve shape with very wide maxima, medium currents and high methanol oxidation overpotential. The material NBH-1, synthesised using the $NaBH_4$ method, exhibits very low methanol oxidation activity. It must be noted that after heating the material NBH-1 at 600 °C, the acquired material (noted as NBH-2) exhibits higher currents than NBH-1, indicating that the heat treatment has a slight activating effect. However, the high oxidation overpotential has not decreased with the heat treatment, i.e., the overall activity of the material was not noticeably improved.

As the hump before the main methanol oxidation peak in the positive-going potential sweep is roughly at the same potential as the negative-going peak, it is reasonable to believe that the hump in the positive going sweep is of the same origin as the peak in the negative going potential sweep, which has been suggested to be the result of the oxidation of adsorbed CO [6,133]. However, more recently, the two different peaks in the positive and negative going potential scans have been suggested to both have their origins in the oxidation of adsorbed methanol, rather than CO [134,135], and the hysteresis between the peak currents arising from the OH_{ad} blocking the surface on the negative going scan. Only after some of the OH_{ad} has been reduced, i.e. cleaning the electrode surface, the adsorption and oxidation of methanol is started [135].

In a perhaps counterintuitive sense, as we assume CeO_2 to function as the provider of oxygen-containing surface functional groups (as discussed in the literature overview [56,69]), it leads us to expect comparatively higher negative-going peak currents for Pt-CeO_2 catalysts than for the pure Pt catalysts (this is mostly true for the catalysts in this study). As the adsorbed oxygen-containing groups are necessary for the oxidation of methanol to CO_2, but the decrease of OH_{ad} on Pt sites is also necessary for the methanol oxidation to occur, we assume that the higher oxidation currents in the negative-going sweep are not the result of low CO tolerance of the catalyst, but increased methanol oxidation activity due to the availability of both free sites for methanol adsorption and adsorbed oxygen-containing surface groups on the catalyst material. As for PtRu catalysts, a similar suggestion has been made for the very low currents of the negative-going peak, in that the removal of OH_{ad} is less facile on PtRu catalysts, leading to lower peak currents at more negative potentials [135]. It must also be noted that the ratio of peak currents for the anodic and cathodic sweeps depends on the positive vertex potential [135] as well as on the potential sweep rate (based on results of this study not shown for brevity).

The peak currents of the positive-going sweep are given in Table XIII, as gravimetric peak current densities, i_{max}, and also normalised to the ECSA of the electrodes, i_{ECSA}. As can be seen, the i_{ECSA} values are higher for materials without CeO_2 additives, which could be assumed to be caused by the lower conductivity of Pt-CeO_2 catalysts. However, the author considers the gravimetric currents to be a more important measure of catalytic activity.

Currents measured in chronoamperometry experiments after 1800 s holding at potential −0.2 V vs. MSE are shown in Fig. 28 and given in Table XIII. The

highest currents were achieved in case of EG-2, while EG-6, IWI-1 and NBH-2 also exhibit high currents.

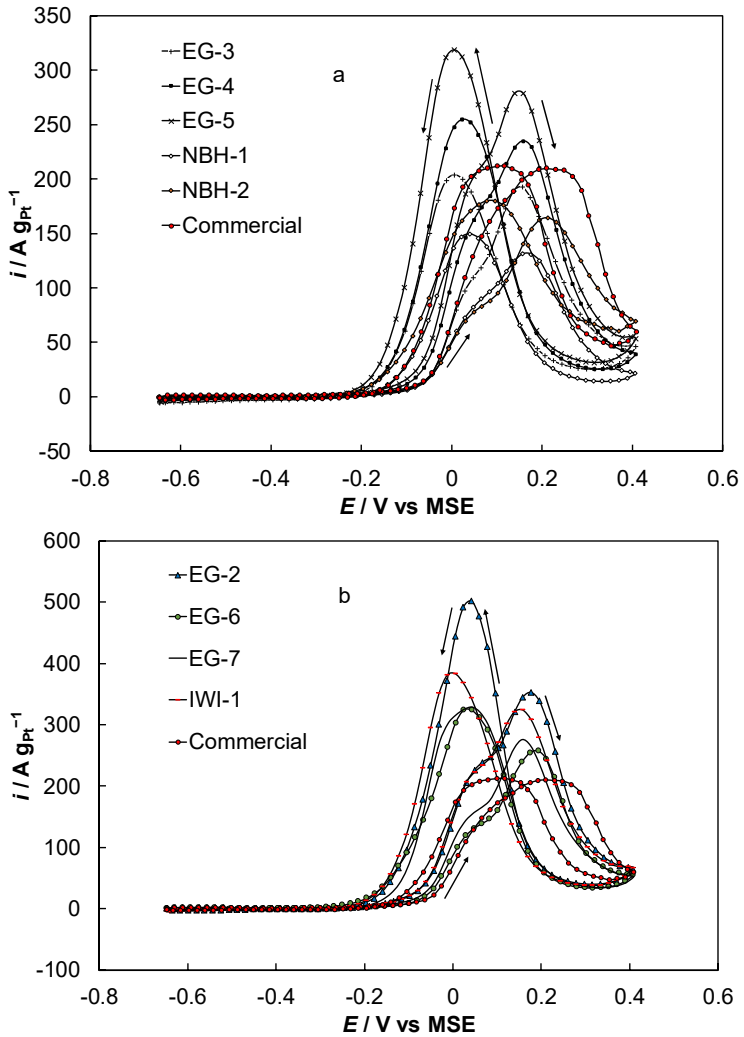

Figure 27. (**a**) and (**b**) (divided for clarity) cyclic voltammograms of the Pt-CeO_2-C catalysts (noted in figure) measured in 1 M CH_3OH + 0.5 M H_2SO_4 saturated with argon at potential sweep rate 10 mV s^{-1}.

Literature concerning Pt-CeO_2 catalysts is extensive and for example both higher [61] and lower [54] methanol oxidation currents have been shown. It is apparent that the preparation conditions of the catalyst materials play a major role in the activity of the studied electrode materials. The crystallinity and amount of ceria in the catalysts can affect the activity in different and opposite ways, i.e., while it provides oxygen-containing surface groups for methanol

oxidation, it also affects the conductivity of the catalyst material. Very good results have been obtained by varying the calcination temperatures of CeO_2-C support material containing 6% ceria [61]. It is possible that in the current study the higher content of ceria had a hampering effect on methanol oxidation due to lower conductivity of the electrode surface.

Of equal importance is the synthesis route of Pt nanoparticles, as for example the synthesis using $NaBH_4$ can exhibit lower activity due to larger Pt particles, while microwave synthesis and reduction with hydrogen at elevated temperatures can produce very small and uniform Pt nanoparticles that exhibit high activity. This is also influenced by the catalyst support material structure, which is another important aspect that needs to be studied in detail.

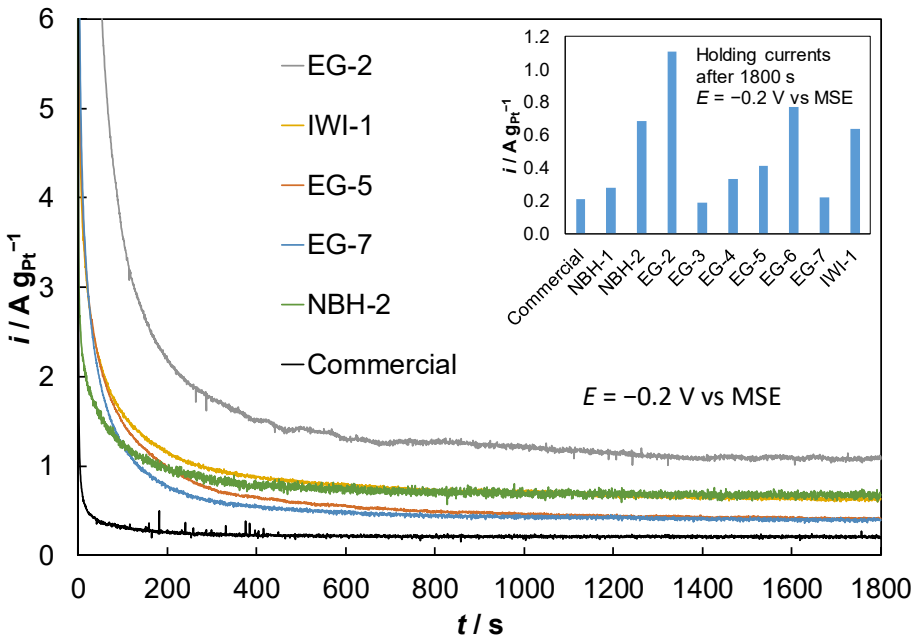

Figure 28. Chronoamperometry *i* vs. *t* curves of the Pt-CeO_2-C catalysts (noted in figure) measured in 1 M CH_3OH + 0.5 M H_2SO_4 solution saturated with argon at a potential $E = -0.2$ V vs. MSE. The inset shows the holding currents for the studied materials after 1800 s.

6.9.3.5. Methanol oxidation reaction on Pt-PrO_x-C materials

Cyclic voltammograms for the synthesised materials measured in 0.5 M H_2SO_4 + 1 M CH_3OH solution are shown in Fig. 29a and 29b. Selected data are also shown in Table XIV. Data for a Pt-CeO_2-C catalyst material (IWI-1 from previous chapter) are shown for comparison, along with a commercial Pt-C material. The shapes of the CVs for the Pt-REO materials are very similar. The positive-going potential sweep exhibits a peak at around 0.15 V vs. MSE, with a

small hump (pre-peak) at around 0 V vs. MSE, before the main peak. The hump coincides with the peak for the negative-going potential sweep. The negative-going peak exhibits higher currents than the positive-going sweep in case of the Pt-REO materials, in contrast with the commercial Pt-C material, where the current peaks are roughly equal, and the Pt-C blank material, where negative-going sweep exhibits lower currents.

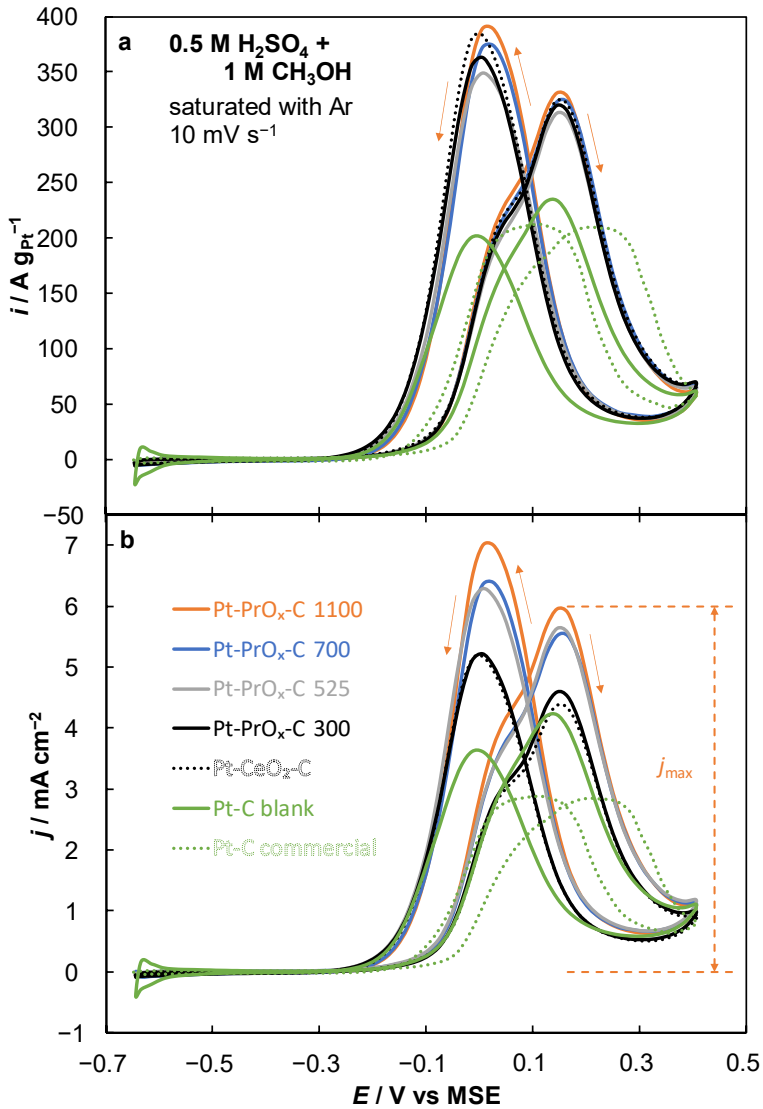

Figure 29. Cyclic voltammograms for Pt-PrO_x-C and reference materials (noted in figure) measured in 0.5 M H_2SO_4 + 1 M CH_3OH solution saturated with argon. The potential sweep rate is 10 mV s^{-1}. The currents are normalised (**a**) to the mass of the platinum on the electrode and (**b**) to the geometric surface area of the electrodes.

In Fig. 29a the currents are normalised to the mass of platinum on the electrode. All the Pt-REO materials exhibit nearly the same gravimetric currents in the positive-going potential sweep, in the range from 313 A g_{Pt}^{-1} to 331 A g_{Pt}^{-1}. In the negative going sweep, the peak currents are higher and somewhat more separated. In case of the Pt-PrO_x-C materials, the negative-going peak currents follow the same trend as in the positive-going sweep, however the Pt-CeO_2-C material exhibits relatively higher current in the negative-going peak compared to the Pt-PrO_x-C materials. Both the Pt-C blank and the commercial Pt-C material exhibit markedly lower currents.

In Fig. 29b the currents are normalised to the geometric surface area of the electrode. Interestingly, the differences between the materials are more pronounced. Most noticeable is the fact that all Pt-PrO_x-C materials perform better than the Pt-CeO_2-C material. In case of the PrO_x-C materials, the methanol oxidation activity as expressed by the current peak at $E = 0.15$ V, is higher for the materials calcined at higher temperatures. The material Pt-PrO_x-C 300 exhibits only slightly higher activity than Pt-CeO_2-C, however materials calcined at higher temperatures are noticeably more active, albeit with smaller differences between them. The materials Pt-PrO_x-C 525 and 700 exhibit nearly similar activities, however Pt-PrO_x-C 525 has slightly higher currents in the positive going sweep and slightly lower currents in the negative going sweep when compared to the material Pt-PrO_x-C 700. It must be noted that Pt-PrO_x-C 1100 has the highest activity, but also slightly higher Pt content. The material Pt-C blank has the lowest activity of the synthesised materials.

The same order of activity for the studied materials has been established based on chronoamperometry results measured at $E = -0.2$ V vs. MSE and are shown in Fig. 30. The currents decreased rapidly at the beginning of the measurement until reaching a plateau roughly after 400 s, depending on the material under study. Overall, the results are similar to the CV measurements. The highest currents at the end of the 1800 s holding were measured in case of Pt-PrO_x-C 1100 and 700, with the currents reaching a plateau at around 0.91 A g_{Pt}^{-1} and 0.86 A g_{Pt}^{-1} respectively. The rest of the Pt-PrO_x-C materials behaved similarly along with the Pt-CeO_2-C material, with the current plateaus slightly above 0.6 A g_{Pt}^{-1}. The Pt-C blank material had a slightly lower activity, and the commercial Pt-C material had the lowest activity, over four times lower than for Pt-PrO_x-C 1100. When calculated as current densities per geometric surface area of the electrode, the difference between these two materials is nearly six times.

While these measurements reinforce the fact that praseodymium oxide is a suitable and beneficial additive to Pt for the oxidation of methanol on platinum-based complex catalysts, some aspects should be discussed further. The values of methanol oxidation peak currents normalised to ECSA (i_{ECSA}, shown in Table XIV) are highest in case of the commercial Pt-C material and lowest in case of Pt-C blank while the gravimetric current densities, i_{max}, on both of these materials is similarly low. The lowest i_{ECSA} for the Pt-PrO_x-C materials was calculated in case of Pt-PrO_x-C 1100, which had the highest methanol oxidation

activity. While higher i_{ECSA} values are often taken as a measure of higher catalytic activity, in this case this is evidently not true. The role of praseodymium oxide in these catalysts as a provider of oxygen-containing surface functional groups, necessary for the oxidation of methanol, will not be taken into account in the measurement of hydrogen underpotential deposition (i.e., ECSA). It is possible that CO stripping voltammetry would take this more into account.

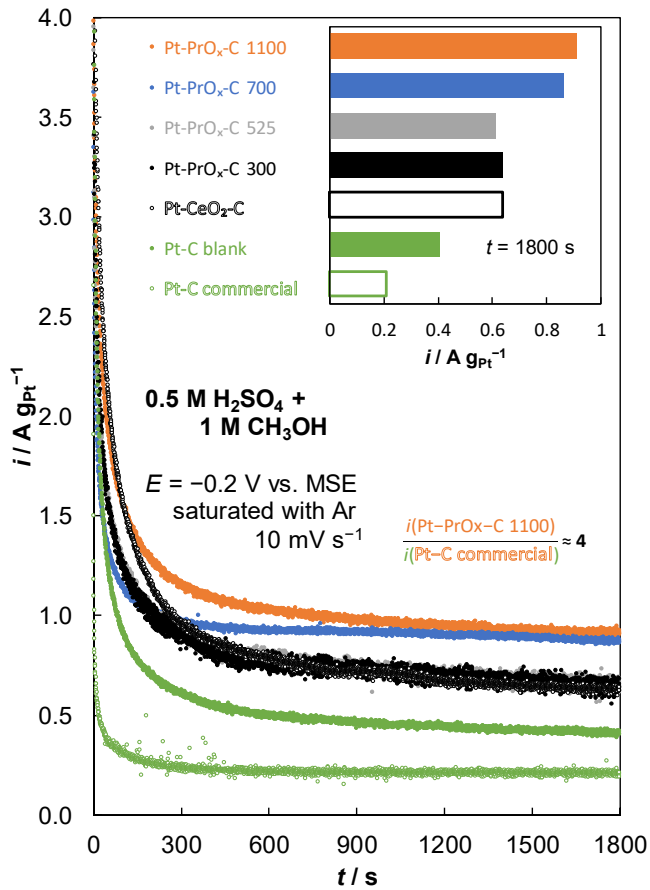

Figure 30. Chronoamperometry results for Pt-PrO$_x$-C and reference materials (noted in figure) measured in 0.5 M H_2SO_4 + 1 M CH_3OH solution saturated with argon at E = −0.2 V vs. MSE. The different materials are noted in figure. The inset shows the final current densities after 1800 s.

The onset potential of methanol oxidation on Pt-PrO$_x$-C complex catalysts is shifted towards less anodic potentials when compared to the commercial Pt-C catalyst. Surprisingly, the onset potential for Pt-C blank material is rather close to the Pt-PrO$_x$-C materials, although still slightly more anodic. This is most

probably explained by very good dispersion of small Pt nanoclusters on the catalyst surface, especially when compared to the commercial Pt-C material. The ECSA values calculated from CV data illustrates this well, as the ECSA value for the Pt-C blank is similar to the ECSA values calculated in case of the Pt-PrOx-C materials and nearly two times higher than in case of the commercial Pt-C. However, even though the onset potential is improved in case of Pt-C blank when compared to the commercial Pt-C material, the higher current values in case of the Pt-REO materials for both of the current peaks still illustrates the beneficial nature of additives in complex catalysts when compared to pure Pt-based catalysts.

Some of the physical characterisation methods indicated the presence of chlorine in the catalyst materials after the deposition of platinum. As chloride ions adsorb specifically on the Pt surface, this could affect the catalytic activity of the materials. One of the materials was additionally washed with a copious amount of water, however the methanol oxidation currents remained the same, indicating that the chlorine does not have a noticeable influence on the catalytic activity. This is corroborated by the fact, that all the Pt containing catalyst materials had very similar ECSA values, including the Pt-C blank, where no traces of chlorine were found. Additionally, while it is possible that washing with water did not dissolve all chlorine containing compounds and acid leaching should be performed, this would have a profound effect on the catalyst as a whole and would be a scope for a different study. As such the results here are shown without any specific effort to remove any possible chlorine containing compounds.

The shape of the CVs measured in the methanol solution offers another point of consideration. For catalysts not containing rare-earth metal oxides, the negative-going potential sweep exhibits lower currents than the positive-going potential sweep. The opposite is true for the Pt-REO catalysts. As has been discussed earlier in literature as well as in this work, the higher current peak at around $E = 0$ V in the negative-going potential sweep is to be expected for REO containing catalysts. While the ratio of the positive- and negative-going peaks has been suggested as a measure of catalytic activity (in that higher positive-going peak vs. negative-going peak indicates a more active catalyst), this is probably a somewhat simplified explanation. While the negative-going peak has been viewed as arising from the oxidation of the platinum catalyst poisons such as carbon monoxide lingering on the surface from the methanol oxidation during the positive-going sweep [6,133], it has been shown that this peak in essence is also a peak attributable to methanol oxidation rather than to the oxidation of CO or other methanol oxidation intermediates [134,135]. The reason being that for methanol oxidation both adsorbed oxygen-containing groups as well as free sites for the adsorption of methanol are required on the catalyst surface. In the positive-going sweep, the Pt surface is oxidised or covered with OH_{ad} near the positive vertex potential, inhibiting the methanol oxidation reaction. In the negative-going sweep, as the Pt metal surface is liberated from surface compounds, the surface is now suitable for methanol

adsorption, and as the REO surface has enough oxygen containing groups, the methanol oxidation can now occur at a high rate, as is evident from the high peak currents. The removal of oxygenated species from the surface of Pt-C catalysts is more difficult, leading to lower peak current values in the negative-going potential sweep. Similar results have been observed in case of PtRu catalysts, where the catalyst is easily oxidised, resulting in lower negative-going peak currents [135].

6.9.3.6. Electrochemical impedance spectroscopy

EIS results measured in 0.5 M H_2SO_4 and 0.5 M H_2SO_4 + 1 M CH_3OH solutions for material EG-3 are shown in Fig. 31. Two equivalent circuits (shown in Fig. 32) based on physical processes were used to model the EIS data. The fitted data are shown in Fig. 31 as solid lines. The modelling parameters are given in Table XV.

The Nyquist plots representing EIS data measured in 0.5 M H_2SO_4 saturated with argon (Fig. 31a) exhibit mostly capacitive behaviour, although surprisingly at lower frequencies, the spectra deviate from purely capacitive behaviour. The corresponding Bode plots (Fig. 31b) show very similar behaviour for all the studied potentials. The (absolute values of) phase angles ($-\theta$) reach maxima of over 80° in the frequency range 0.1 ... 10 Hz.

After the addition of methanol, the Nyquist plot (Fig. 31c) at $E = -0.4$ V is very similar to that measured before the addition of methanol. However, at the potential $E = -0.2$ V the spectrum is showing the beginning of a formation of a half-circle, as the methanol oxidation is starting to occur. At the potential $E = 0.03$ V (the peak potential of the negative-going scan on CVs) the spectrum changes dramatically, exhibiting pseudo-inductive behaviour. Based on literature data [133,136,137], this indicates a reaction mechanism with one adsorbed intermediate, although in case of methanol oxidation, many intermediates likely exist, but the turnover rate of all but one intermediate is very fast. The spectrum at the potential $E = 0.18$ V (the peak potential for the positive potential direction scan on CVs) does not extend further than the second quadrant. It must be noted that significant noise was present at lower frequencies (< 0.1 Hz). The overall shape however indicates a wider circle than at $E = 0.03$ V, most probably caused by decreased surface coverage of CO as a result of the reaction with adsorbed oxygen-containing species [136].

The Bode plot (Fig. 31d) shows correspondingly different spectra for the studied potentials. Very noticeable for potential $E = 0.03$ V is the (negative) phase angle increasing up to 180° and then switching its sign at $f = 0.14$ Hz. In case of $E = 0.18$ V, the (negative) phase angle increases to roughly 150°. The spectra for $E = -0.4$ V and $E = -0.2$ V are analogous to those measured before the addition of methanol.

The experimental EIS data calculated using two equivalent circuits (Fig. 32) is shown in Table XV. Circuit A was used to fit impedance data measured

before the addition of methanol and also for impedance data measured at potentials $E = -0.4$ V and $E = -0.2$ V after the addition of methanol.

Circuit A is semi-empirical, where R_S is the uncompensated solution resistance, C_1 is the high-frequency, i.e. electrical double layer (so-called „true“) capacitance ($f \rightarrow \infty$), R_1 is the charge transfer resistance, CPE_1 is a constant phase element representing mixed adsorption kinetics on the inhomogeneous electrode surface, R_2 is the mass transfer resistance and C_2 is the adsorption capacitance. Circuit B has been used previously [133,137,138] to fit impedance data of methanol oxidation.

In circuit B, R_S is the uncompensated solution resistance, CPE_1 is a constant phase element, representing double layer capacitance (while taking into account the inhomogeneity of the electrode surface), R_1 is the charge transfer resistance for the methanol oxidation step, R_2 and L_1 are the charge transfer resistance and inductance due to the oxidation of the adsorbed CO layer, respectively [137].

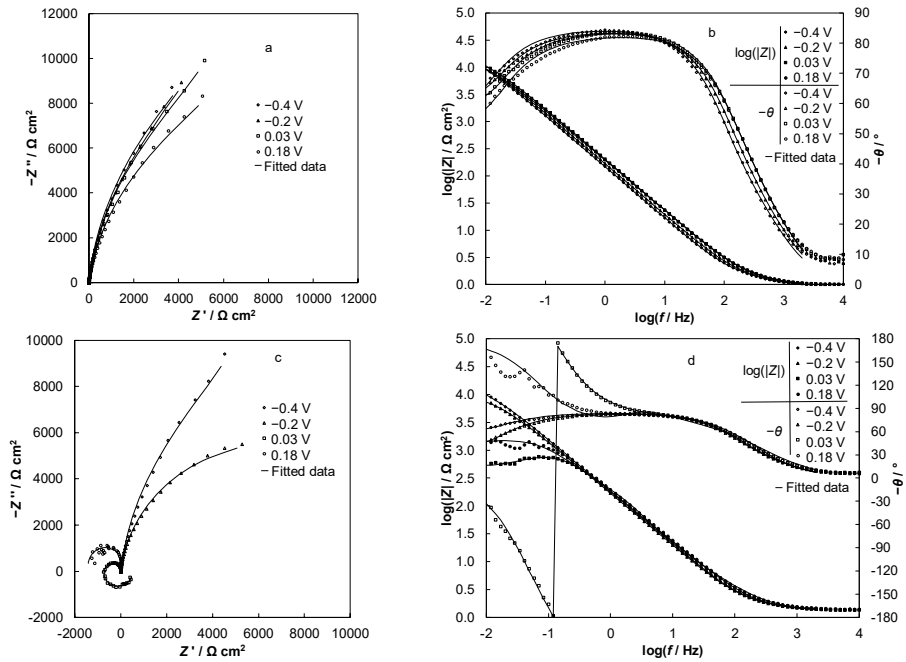

Figure 31. (**a**) Nyquist plots and (**b**) Bode plots measured at different potentials (noted in figure) in 0.5 M H_2SO_4 solution saturated with argon for Pt-CeO_2-C material EG-3 and (**c**) Nyquist plots and (**d**) Bode plots measured at different potentials (noted in figure) in 1 M CH_3OH + 0.5 M H_2SO_4 solution saturated with argon for Pt-CeO_2-C material EG-3. The fitted data are shown in the figures as solid lines. The impedance values are normalised to apparent electrode area.

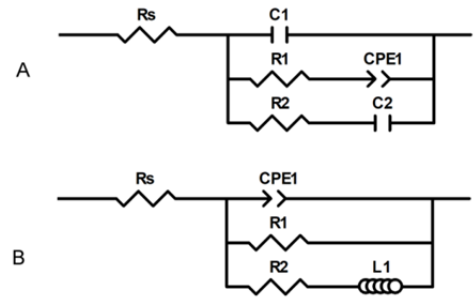

Figure 32. Equivalent circuits **A** and **B** used for modelling methanol oxidation reaction electrochemical impedance spectroscopy data.

The modelling parameters of the CPE are given according to the following equation:

$$Z_{\mathrm{CPE}} = A^{-1} (\mathrm{j}\omega)^{-\alpha} \tag{19}$$

In case of solutions containing MeOH, Circuit B is applied at $E \geq 0.03$ V.

Comparatively low χ^2 and Δ^2 values have been calculated for both circuits, with the exception of fitting data at $E = 0.18$ V in MeOH containing solution. The modelling parameters, given in Table XV, show that the series high-frequency resistance, R_S, is independent of the potential, but slightly increases after the addition of MeOH (explained by decreasing electrolyte conductivity). The high-frequency capacitance, C_1, very weakly decreases with the increase of electrode potential, as well with the addition of MeOH, explained by the decrease of dielectrical permittivity of the electrical double-layer. In Circuit A, the charge-transfer resistance, R_1, has a maximal value at $E = 0.03$ V for a solution not containing MeOH. Very high mass-transfer (i.e. low-frequency) resistance values, R_2, have been calculated for some materials using Circuit A. The values decrease slightly with the increase of the electrode potential. With the addition of MeOH, the values remain high, but decrease more rapidly with increasing potential.

For Circuit B, the R_1 values are negative and have high values at potentials where the Faradic oxidation reaction of MeOH and intermediates are taking place. The R_2 values, associated with the charge-transfer resistance of CO oxidation, are comparable in magnitude with R_1 values, although with a positive sign. The inductance value L_1 is rather high in case of $E = 0.03$ V and remarkably lower at $E = 0.18$ V. The values for A_2 are comparable to the C_1 values for Circuit A. For both circuits, the α values are lower than 0.9, indicating a well pronounced energetic inhomogeneity of electrode surface under study [139,140].

Table XV. Modelling parameters used for fitting electrochemical impedance spectroscopy data measured for material EG-3.

Circuit A (Fig. 32)									
E **/ V**	**R_S / Ω cm²**	**C_1 / mF cm^{-2}**	**R_1 / Ω cm²**	**A_1 / mF cm^{-2} s$^{\alpha-1}$ ***	**α_1 ***	**R_2 / Ω cm²**	**C_2 / mF cm^{-2}**	**$\chi^2 \cdot 10^3$**	**Δ^2**
Measured in 0.5 M H_2SO_4 saturated with Ar									
−0.40	1.018 ± 0.005	0.48 ± 0.01	1.805 ± 0.099	0.73 ± 0.01	0.898 ± 0.002	26409 ± 549	2.13 ± 0.20	0.60	0.080
−0.20	1.006 ± 0.005	0.42 ± 0.01	1.803 ± 0.102	0.66 ± 0.01	0.883 ± 0.002	25180 ± 447	1.58 ± 0.08	0.42	0.056
0.03	1.009 ± 0.006	0.36 ± 0.01	1.975 ± 0.142	0.54 ± 0.01	0.876 ± 0.002	24891 ± 417	1.52 ± 0.07	0.47	0.082
0.18	1.017 ± 0.007	0.35 ± 0.01	1.845 ± 0.168	0.61 ± 0.01	0.859 ± 0.003	20389 ± 359	2.37 ± 0.16	0.62	0.063
Measured in 1 M CH_3OH + 0.5 M H_2SO_4 saturated with Ar									
−0.40	1.381 ± 0.010	0.40 ± 0.01	1.784 ± 0.201	0.59 ± 0.01	0.886 ± 0.003	23582 ± 539	1.55 ± 0.10	0.87	0.116
−0.20	1.372 ± 0.007	0.42 ± 0.01	1.836 ± 0.142	0.66 ± 0.01	0.879 ± 0.002	11700 ± 107	7.35 ± 0.51	0.46	0.061

Circuit B (Fig. 32)								
E **/ V**	**R_S / Ω cm²**	**A_2 / mF cm^{-2} s$^{\alpha-1}$ ***	**α_2 ***	**R_1 / Ω cm²**	**R_2 / Ω cm²**	**L_1 / H cm²**	**χ^2**	**Δ^2**
Measured in 1 M CH_3OH + 0.5 M H_2SO_4 saturated with Ar								
0.03	1.411 ± 0.015	1.07 ± 0.01	0.898 ± 0.002	−581.8 ± 6.3	273.7 ± 2.2	1493 ± 21	0.005	0.644
0.18	1.284 ± 0.043	1.84 ± 0.07	0.803 ± 0.007	−97.1 ± 11.9	104.4 ± 13.7	5 ± 1	0.040	5.364

χ^2 – the square of the standard deviation between the original data and the calculated spectrum

Δ^2 – the weighted sum of squares.

* The modelling parameters of the constant phase elements are given according to Eq. 19.

7. SUMMARY

Pt-CeO_2-C and Pt-PrO_x-C catalysts were synthesised to study the methanol oxidation reaction on Pt-rare-earth metal oxide based catalysts. Electrochemical and physical characterisation of the materials were performed. Various aspects of the catalyst support material preparation were studied, e.g. the calcination temperature of the rare-earth oxide material. Methods for the deposition of Pt particles were developed. The influence of the synthesis parameters of the ethylene glycol method, such as the Pt precursor concentration, reaction mixture pH, etc, on the size and dispersion of Pt nanoclusters were studied and discussed. In addition, deposition of Pt by reduction of Pt precursor using hydrogen or sodium borohydride was studied, and the results were compared.

The oxygen reduction reaction was studied on Pt catalysts deposited onto various carbon supports by the ethylene glycol method. The influence of Pt synthesis conditions on catalyst properties was investigated using electrochemical and physical characterisation methods.

In addition, the structure and stability of molybdenum carbide derived carbon materials, developed in University of Tartu, were studied for application as catalyst support material.

Various physical characterisation methods were used to analyse the studied materials, such as X-ray diffraction, scanning electron microscopy, microwave plasma atomic emission spectrometry, thermogravimetric analysis, low-temperature nitrogen adsorption etc. Electrochemical methods, such as cyclic voltammetry, rotating disk electrode method, chronoamperometry and electrochemical impedance spectroscopy were used to study the stability and catalytic activity of the synthesised materials.

The partially chlorinated C(Mo_2C)+Mo_2C composite materials were found to contain β-Mo_2C crystalline phase and an amorphous microporous-mesoporous carbon phase. Very high surface area values were determined for materials with lower Mo_2C content. Electrochemically the materials exhibit capacitive behaviour in a wide potential range with high gravimetric capacitance values. The unchlorinated Mo_2C was found to dissolve completely during electrochemical measurements, which had some influence on the final microporous-mesoporous structure of the carbon material. Electrochemical impedance spectroscopy data suggested that the high-frequency series resistance is not dependent on the Mo_2C content. As such, these materials offer an interesting option for use as electrode materials in high energy density supercapacitors or as fuel cell catalyst support materials. This was also tested by depositing Pt using the ethylene glycol method onto the Mo_2C-derived carbon catalyst support, and decent electrochemically active surface area values and oxygen reduction reaction mass and specific activity values were achieved.

The synthesis of rare-earth metal oxide modified carbon support materials (CeO_2-C and PrO_x-C) was performed using various methods, such as deposition using the ethylene glycol method, co-deposition with Pt or calcination of rare-

earth precursor material at various temperatures. The deposition of Pt onto the synthesised rare-earth containing catalyst support materials was performed using various methods, of which both the ethylene glycol method at high reaction mixture pH as well as the incipient wetness impregnation method (i.e., reduction with hydrogen) were found to yield very small, well-dispersed Pt nanoclusters.

Physical characterisation of rare-earth metal oxide modified materials was performed and the influence of synthesis methods on the crystallinity, morphology and stoichiometry was studied. The praseodymium oxide based materials exhibited a nanorod structure, with the crystallinity and specific oxide form dependent on the calcination temperature. The nanorods were visualised using scanning electron microscopy.

Electrochemically, the Pt-rare-earth metal oxide materials exhibited good activity towards methanol oxidation as well as very good stability. The electrochemical activity was found to depend on the synthesis conditions of the rare-earth metal oxide (i.e. synthesis method, calcination temperature, etc) as well as on the conditions of Pt deposition. The highest activity towards methanol oxidation was found for material Pt-PrO_x-C 1100, which had a decent Pt electrochemically active surface area as well as a partially crystalline praseodymium oxide phase containing several praseodymium oxide forms.

Aspects of electrocatalysis of methanol oxidation were briefly discussed and in case of rare-earth metal oxide based materials, the ability to provide adsorbed oxygen-containing species on the rare-earth metal oxide surface was suggested to positively influence the methanol electrooxidation on the Pt catalyst surface.

8. REFERENCES

[1] M. Kauw, R.M.J. Benders, C. Visser, Green methanol from hydrogen and carbon dioxide using geothermal energy and/or hydropower in Iceland or excess renewable electricity in Germany, *Energy* 90 (2015) 208–217. https://doi.org/10.1016/j.energy.2015.06.002.

[2] T. Elmer, M. Worall, S. Wu, S.B. Riffat, Fuel cell technology for domestic built environment applications: State of-the-art review, *Renewable and Sustainable Energy Reviews* 42 (2015) 913–931. https://doi.org/10.1016/j.rser.2014.10.080.

[3] J. Kotowicz, D. Węcel, A. Kwilinski, M. Brzęczek, Efficiency of the power-to-gas-to-liquid-to-power system based on green methanol, *Applied Energy* 314 (2022) 118933. https://doi.org/10.1016/j.apenergy.2022.118933.

[4] M.K. Debe, Electrocatalyst approaches and challenges for automotive fuel cells, *Nature* 486 (2012) 43–51. https://doi.org/10.1038/nature11115.

[5] S. Shahgaldi, J. Hamelin, Improved carbon nanostructures as a novel catalyst support in the cathode side of PEMFC: a critical review, *Carbon* 94 (2015) 705–728. https://doi.org/10.1016/j.carbon.2015.07.055.

[6] T. Iwasita, Electrocatalysis of methanol oxidation, *Electrochim. Acta* 47 (2002) 3663–3674. https://doi.org/10.1016/S0013-4686(02)00336-5.

[7] N. Kakati, J. Maiti, S.H. Lee, S.H. Jee, B. Viswanathan, Y.S. Yoon, Anode Catalysts for Direct Methanol Fuel Cells in Acidic Media: Do We Have Any Alternative for Pt or Pt–Ru?, *Chem. Rev.* 114 (2014) 12397–12429. https://doi.org/10.1021/cr400389f.

[8] M. Oezaslan, F. Hasché, P. Strasser, Pt-Based Core–Shell Catalyst Architectures for Oxygen Fuel Cell Electrodes, *J. Phys. Chem. Lett.* 4 (2013) 3273–3291. https://doi.org/10.1021/jz4014135.

[9] S. Sharma, B.G. Pollet, Support materials for PEMFC and DMFC electrocatalysts-A review, *J. Power Sources* 208 (2012) 96–119. https://doi.org/10.1016/j.jpowsour.2012.02.011.

[10] E. Härk, R. Jäger, E. Lust, Effect of Platinum Nanoparticle Loading on Oxygen Reduction at a Pt Nanocluster-Activated Microporous–Mesoporous Carbon Support, *Electrocatalysis* 6 (2014) 242–254. https://doi.org/10.1007/s12678-014-0238-6.

[11] K. Vaarmets, J. Nerut, E. Härk, E. Lust, Electrochemical and physical characterisation of Pt-nanocluster activated molybdenum carbide derived carbon electrodes, *Electrochimica Acta* 104 (2013) 216–227. https://doi.org/10.1016/j.electacta.2013.04.097.

[12] P. Teppor, R. Jäger, M. Paalo, A. Adamson, M. Härmas, O. Volobujeva, J. Aruväli, R. Palm, E. Lust, Peat as a carbon source for non-platinum group metal oxygen electrocatalysts and AEMFC cathodes, *Int. J. Hydrogen Energy* 47 (2022) 16908–16920. https://doi.org/10.1016/j.ijhydene.2022.03.199.

[13] W. Lobjakas, J. Nerut, H. Kasuk, A. Adamson, T. Thomberg, J. Aruväli, P. Valk, P. Teppor, M. Koppel, V. Mikli, O. Volobujeva, E. Lust, Investigation of Oxygen Reduction on Platinum Nanoparticles Deposited Onto Peat-Derived Carbon Carrier, *ECS Trans.* 108 (2022) 49. https://doi.org/10.1149/10807.0049ecst.

[14] A. Jänes, T. Thomberg, H. Kurig, E. Lust, Nanoscale fine-tuning of porosity of carbide-derived carbon prepared from molybdenum carbide, *Carbon* 47 (2009) 23–29. https://doi.org/10.1016/j.carbon.2008.07.010.

[15] A. Jänes, T. Thomberg, E. Lust, Synthesis and characterisation of nanoporous carbide-derived carbon by chlorination of vanadium carbide, *Carbon* 45 (2007) 2717–2722. https://doi.org/10.1016/j.carbon.2007.09.041.
[16] T. Thomberg, A. Jänes, E. Lust, Energy and power performance of electrochemical double-layer capacitors based on molybdenum carbide derived carbon, *Electrochimica Acta* 55 (2010) 3138–3143. https://doi.org/10.1016/j.electacta.2010.01.075.
[17] I. Tallo, T. Thomberg, K. Kontturi, A. Jänes, E. Lust, Nanostructured carbide-derived carbon synthesized by chlorination of tungsten carbide, *Carbon* 49 (2011) 4427–4433. https://doi.org/10.1016/j.carbon.2011.06.033.
[18] O.T. Holton, J.W. Stevenson, The Role of Platinum in Proton Exchange Membrane Fuel Cells, *Platin Met Rev* 57 (2013) 259–271. https://doi.org/10.1595/147106713X671222.
[19] C. Song, J. Zhang, Electrocatalytic Oxygen Reduction Reaction, in: J. Zhang (Ed.), PEM Fuel Cell Electrocatalysts and Catalyst Layers, Springer London, 2008: pp. 89–134. http://link.springer.com/chapter/10.1007/978-1-84800-936-3_2 (accessed April 30, 2015).
[20] M. Winter, R.J. Brodd, What Are Batteries, Fuel Cells, and Supercapacitors?, *Chem. Rev.* 104 (2004) 4245–4270. https://doi.org/10.1021/cr020730k.
[21] V. Ramani, H.R. Kunz, J.M. Fenton, The polymer electrolyte fuel cell, *Interface* 13 (2004) 17–19.
[22] A.J. Bard, L.R. Faulkner, Electrochemical methods: fundamentals and applications, Wiley, New York, 2001.
[23] H.A. Gasteiger, S.S. Kocha, B. Sompalli, F.T. Wagner, Activity benchmarks and requirements for Pt, Pt-alloy, and non-Pt oxygen reduction catalysts for PEMFCs, *Applied Catalysis B: Environmental* 56 (2005) 9–35. https://doi.org/10.1016/j.apcatb.2004.06.021.
[24] I.E.L. Stephens, A.S. Bondarenko, U. Grønbjerg, J. Rossmeisl, I. Chorkendorff, Understanding the electrocatalysis of oxygen reduction on platinum and its alloys, *Energy & Environmental Science* 5 (2012) 6744. https://doi.org/10.1039/c2ee03590a.
[25] M. Gara, R.G. Compton, Activity of carbon electrodes towards oxygen reduction in acid: A comparative study, *New Journal of Chemistry* 35 (2011) 2647. https://doi.org/10.1039/c1nj20612e.
[26] H.A. Hansen, V. Viswanathan, J.K. Nørskov, Unifying Kinetic and Thermodynamic Analysis of 2 e^- and 4 e^- Reduction of Oxygen on Metal Surfaces, *J. Phys. Chem. C* 118 (2014) 6706–6718. https://doi.org/10.1021/jp4100608.
[27] R. Jäger, E. Härk, P. Kasatkin, P. Pikma, U. Joost, P. Paiste, J. Aruväli, T. Kallio, H. Jiang, E. Lust, Carbide derived carbon supported Pt nanoparticles with optimum size and amount for efficient oxygen reduction reaction kinetics, *J. Electrochem. Soc.* 164 (2017) F448.
[28] D. Banham, J. Zou, S. Mukerjee, Z. Liu, D. Yang, Y. Zhang, Y. Peng, A. Dong, Ultralow platinum loading proton exchange membrane fuel cells: Performance losses and solutions, *Journal of Power Sources* 490 (2021) 229515. https://doi.org/10.1016/j.jpowsour.2021.229515.
[29] N.M. Markovic, T.J. Schmidt, V. Stamenkovic, P.N. Ross, Oxygen reduction reaction on Pt and Pt bimetallic surfaces: a selective review, *Fuel Cells* 1 (2001) 105–116.

[30] V.R. Stamenkovic, B. Fowler, B.S. Mun, G. Wang, P.N. Ross, C.A. Lucas, N.M. Marković, Improved Oxygen Reduction Activity on Pt_3Ni (111) via Increased Surface Site Availability, *Science* 315 (2007) 493–497. https://doi.org/10.1126/science.1135941.
[31] T. Yoshida, K. Kojima, Toyota MIRAI Fuel Cell Vehicle and Progress Toward a Future Hydrogen Society, *Electrochem. Soc. Interface* 24 (2015) 45. https://doi.org/10.1149/2.F03152if.
[32] J. Greeley, I.E.L. Stephens, A.S. Bondarenko, T.P. Johansson, H.A. Hansen, T.F. Jaramillo, J. Rossmeisl, I. Chorkendorff, J.K. Nørskov, Alloys of platinum and early transition metals as oxygen reduction electrocatalysts, *Nature Chemistry* 1 (2009) 552–556. https://doi.org/10.1038/nchem.367.
[33] M. Escudero-Escribano, A. Verdaguer-Casadevall, P. Malacrida, U. Grønbjerg, B.P. Knudsen, A.K. Jepsen, J. Rossmeisl, I.E.L. Stephens, I. Chorkendorff, Pt5Gd as a Highly Active and Stable Catalyst for Oxygen Electroreduction, *J. Am. Chem. Soc.* 134 (2012) 16476–16479. https://doi.org/10.1021/ja306348d.
[34] A. Velázquez-Palenzuela, F. Masini, A.F. Pedersen, M. Escudero-Escribano, D. Deiana, P. Malacrida, T.W. Hansen, D. Friebel, A. Nilsson, I.E.L. Stephens, I. Chorkendorff, The enhanced activity of mass-selected PtxGd nanoparticles for oxygen electroreduction, *Journal of Catalysis* 328 (2015) 297–307. https://doi.org/10.1016/j.jcat.2014.12.012.
[35] P. Teppor, R. Jäger, M. Paalo, R. Palm, O. Volobujeva, E. Härk, Z. Kochovski, T. Romann, R. Härmas, J. Aruväli, A. Kikas, E. Lust, Peat-derived carbon-based non-platinum group metal type catalyst for oxygen reduction and evolution reactions, *Electrochem. Commun.* 113 (2020) 106700. https://doi.org/10.1016/j.elecom.2020.106700.
[36] P.E. Kasatkin, R. Jäger, E. Härk, P. Teppor, I. Tallo, U. Joost, K. Šmits, R. Kanarbik, E. Lust, Fe-N/C catalysts for oxygen reduction based on silicon carbide derived carbon, *Electrochemistry Communications* 80 (2017) 33–38. https://doi.org/10.1016/j.elecom.2017.05.001.
[37] O. Faye, J. Szpunar, U. Eduok, A critical review on the current technologies for the generation, storage, and transportation of hydrogen, *International Journal of Hydrogen Energy* 47 (2022) 13771–13802. https://doi.org/10.1016/j.ijhydene.2022.02.112.
[38] J.V. Ashurst, T.M. Nappe, Methanol Toxicity, in: StatPearls, StatPearls Publishing, Treasure Island (FL), 2023. http://www.ncbi.nlm.nih.gov/books/NBK482121/ (accessed June 29, 2023).
[39] Z. Nekoukar, Z. Zakariaei, F. Taghizadeh, F. Musavi, E.S. Banimostafavi, A. Sharifpour, N. Ebrahim Ghuchi, M. Fakhar, R. Tabaripour, S. Safanavaei, Methanol poisoning as a new world challenge: A review, *Annals of Medicine and Surgery* 66 (2021) 102445. https://doi.org/10.1016/j.amsu.2021.102445.
[40] R. Paasma, K.E. Hovda, D. Jacobsen, Methanol poisoning and long term sequelae – a six years follow-up after a large methanol outbreak, *BMC Clinical Pharmacology* 9 (2009) 5. https://doi.org/10.1186/1472-6904-9-5.
[41] D. Bayer, F. Jung, B. Kintzel, M. Joos, C. Cremers, D. Martin, J. Bernard, J. Tübke, On the Use of Potential Denaturing Agents for Ethanol in Direct Ethanol Fuel Cells, *International Journal of Electrochemistry* 2011 (2011) e154039. https://doi.org/10.4061/2011/154039.
[42] C.M. Zalitis, J. Sharman, E. Wright, A.R. Kucernak, Properties of the hydrogen oxidation reaction on Pt/C catalysts at optimised high mass transport conditions

and its relevance to the anode reaction in PEFCs and cathode reactions in electrolysers, *Electrochimica Acta* 176 (2015) 763–776. https://doi.org/10.1016/j.electacta.2015.06.146.
[43] O.A. Petrii, The Progress in Understanding the Mechanisms of Methanol and Formic Acid Electrooxidation on Platinum Group Metals (a Review), *Russ J Electrochem* 55 (2019) 1–33. https://doi.org/10.1134/S1023193519010129.
[44] S. Wasmus, A. Küver, Methanol oxidation and direct methanol fuel cells: a selective review, *Journal of Electroanalytical Chemistry* 461 (1999) 14–31. https://doi.org/10.1016/S0022-0728(98)00197-1.
[45] H.A. Gasteiger, N. Markovic, P.N. Ross, E.J. Cairns, Methanol electrooxidation on well-characterized platinum-ruthenium bulk alloys, *J. Phys. Chem.* 97 (1993) 12020–12029. https://doi.org/10.1021/j100148a030.
[46] E.V. Spinacé, A.O. Neto, M. Linardi, Electro-oxidation of methanol and ethanol using PtRu/C electrocatalysts prepared by spontaneous deposition of platinum on carbon-supported ruthenium nanoparticles, *Journal of Power Sources* 129 (2004) 121–126. https://doi.org/10.1016/j.jpowsour.2003.11.056.
[47] Y.-S. Wang, S.-Y. Yang, S.-M. Li, H.-W. Tien, S.-T. Hsiao, W.-H. Liao, C.-H. Liu, K.-H. Chang, C.-C.M. Ma, C.-C. Hu, Three-dimensionally porous graphene–carbon nanotube composite-supported PtRu catalysts with an ultrahigh electrocatalytic activity for methanol oxidation, *Electrochimica Acta* 87 (2013) 261–269. https://doi.org/10.1016/j.electacta.2012.09.013.
[48] Yu.V. Tolmachev, O.A. Petrii, Pt–Ru electrocatalysts for fuel cells: developments in the last decade, *J Solid State Electrochem* 21 (2017) 613–639. https://doi.org/10.1007/s10008-016-3382-5.
[49] P.J. Kulesza, I.S. Pieta, I.A. Rutkowska, A. Wadas, D. Marks, K. Klak, L. Stobinski, J.A. Cox, Electrocatalytic oxidation of small organic molecules in acid medium: Enhancement of activity of noble metal nanoparticles and their alloys by supporting or modifying them with metal oxides, *Electrochimica Acta* 110 (2013) 474–483. https://doi.org/10.1016/j.electacta.2013.06.052.
[50] I.A. Rutkowska, A. Wadas, P.J. Kulesza, Enhancement of oxidative electrocatalytic properties of platinum nanoparticles by supporting onto mixed WO3/ZrO2 matrix, *Applied Surface Science* 388 (2016) 616–623. https://doi.org/10.1016/j.apsusc.2016.02.241.
[51] P.K. Shen, A.C.C. Tseung, Anodic Oxidation of Methanol on Pt / WO 3 in Acidic Media, *J. Electrochem. Soc.* 141 (1994) 3082–3090. https://doi.org/10.1149/1.2059282.
[52] B.E. Hayden, D.V. Malevich, D. Pletcher, Platinum catalysed nanoporous titanium dioxide electrodes in H2SO4 solutions, *Electrochemistry Communications* 3 (2001) 395–399. https://doi.org/10.1016/S1388-2481(01)00182-5.
[53] I.A. Rutkowska, P.J. Kulesza, Electroanalysis of Ethanol Oxidation and Reactivity of Platinum-Ruthenium Catalysts Supported onto Nanostructured Titanium Dioxide Matrices, *J. Electrochem. Soc.* 163 (2016) H3052–H3060. https://doi.org/10.1149/2.0081604jes.
[54] Z. Tang, G. Lu, High performance rare earth oxides LnOx (Ln = Sc, Y, La, Ce, Pr and Nd) modified Pt/C electrocatalysts for methanol electrooxidation, *J. Power Sources* 162 (2006) 1067–1072. https://doi.org/10.1016/j.jpowsour.2006.07.052.
[55] Z. Tang, G. Lu, Synthesis and characterization of high performance Pt-(PrxCeyOz)/C catalysts for methanol electrooxidation, *Applied Catalysis B: Environmental* 79 (2008) 1–7. https://doi.org/10.1016/j.apcatb.2007.09.043.

[56] M. Takahashi, T. Mori, F. Ye, A. Vinu, H. Kobayashi, J. Drennan, Design of High-Quality Pt–CeO2 Composite Anodes Supported by Carbon Black for Direct Methanol Fuel Cell Application, *Journal of the American Ceramic Society* 90 (2007) 1291–1294. https://doi.org/10.1111/j.1551-2916.2006.01483.x.
[57] D.-J. Guo, Z.-H. Jing, A novel co-precipitation method for preparation of Pt-CeO2 composites on multi-walled carbon nanotubes for direct methanol fuel cells, *Journal of Power Sources* 195 (2010) 3802–3805. https://doi.org/10.1016/j.jpowsour.2009.12.115.
[58] D.-M. Gu, Y.-Y. Chu, Z.-B. Wang, Z.-Z. Jiang, G.-P. Yin, Y. Liu, Methanol oxidation on Pt/CeO2–C electrocatalyst prepared by microwave-assisted ethylene glycol process, *Applied Catalysis B: Environmental* 102 (2011) 9–18. https://doi.org/10.1016/j.apcatb.2010.11.018.
[59] X. Wang, X. Li, D. Liu, S. Song, H. Zhang, Green synthesis of Pt/CeO2/graphene hybrid nanomaterials with remarkably enhanced electrocatalytic properties, *Chemical Communications* 48 (2012) 2885–2887. https://doi.org/10.1039/C2CC17409J.
[60] H. Chen, J. Duan, X. Zhang, Y. Zhang, C. Guo, L. Nie, X. Liu, One step synthesis of Pt/CeO2–graphene catalyst by microwave-assisted ethylene glycol process for direct methanol fuel cell, *Materials Letters* 126 (2014) 9–12. https://doi.org/10.1016/j.matlet.2014.03.095.
[61] M. Wu, M. Han, M. Li, Y. Li, J. Zeng, S. Liao, Preparation and characterizations of platinum electrocatalysts supported on thermally treated CeO2–C composite support for polymer electrolyte membrane fuel cells, *Electrochimica Acta* 139 (2014) 308–314. https://doi.org/10.1016/j.electacta.2014.07.029.
[62] H. Xu, A.-L. Wang, Y.-X. Tong, G.-R. Li, Enhanced Catalytic Activity and Stability of Pt/CeO2/PANI Hybrid Hollow Nanorod Arrays for Methanol Electrooxidation, *ACS Catal.* 6 (2016) 5198–5206. https://doi.org/10.1021/acscatal.6b01010.
[63] S. Dai, J. Zhang, Y. Fu, W. Li, Histidine-assisted synthesis of CeO2 nanoparticles for improving the catalytic performance of Pt-based catalysts in methanol electrooxidation, *New J. Chem.* 42 (2018) 18159–18165. https://doi.org/10.1039/C8NJ03972K.
[64] G. Zhang, Z. Yang, W. Zhang, Y. Wang, Nanosized Mo-doped CeO 2 enhances the electrocatalytic properties of the Pt anode catalyst in direct methanol fuel cells, *Journal of Materials Chemistry A* 5 (2017) 1481–1487. https://doi.org/10.1039/C6TA09043E.
[65] L. Chen, J. Hu, J.S. Foord, Electrodeposition of a Pt–PrO2−x electrocatalyst on diamond electrodes for the oxidation of methanol, *Phys. Status Solidi A* 209 (2012) 1792–1796. https://doi.org/10.1002/pssa.201200049.
[66] Y. Yang, Z. Li, Y. Yu, X. Zhang, H. Wei, H. Chu, Understanding enhancing mechanism of Pr6O11 and Pr(OH)3 in methanol electrooxidation, *Journal of Rare Earths* 40 (2022) 85–92. https://doi.org/10.1016/j.jre.2020.10.011.
[67] C. Xu, P.K. Shen, Novel Pt/CeO2/C catalysts for electrooxidation of alcohols in alkaline media, *Chem. Commun.* 0 (2004) 2238–2239. https://doi.org/10.1039/B408589B.
[68] C. Xu, R. Zeng, P.K. Shen, Z. Wei, Synergistic effect of CeO2 modified Pt/C catalysts on the alcohols oxidation, *Electrochimica Acta* 51 (2005) 1031–1035. https://doi.org/10.1016/j.electacta.2005.05.041.

[69] T. Mori, D.R. Ou, J. Zou, J. Drennan, Present status and future prospect of design of Pt–cerium oxide electrodes for fuel cell applications, *Progress in Natural Science: Materials International* 22 (2012) 561–571. https://doi.org/10.1016/j.pnsc.2012.11.010.
[70] D.R. Ou, T. Mori, K. Fugane, H. Togasaki, F. Ye, J. Drennan, Stability of Ceria Supports in Pt–CeOx/C Catalysts, *J. Phys. Chem. C* 115 (2011) 19239–19245. https://doi.org/10.1021/jp205640k.
[71] E. Lust, P. Möller, I. Kivi, G. Nurk, S. Kallip, P. Nigu, K. Lust, Optimization of the cathode composition for the intermediate-temperature SOFC, *J. Electrochem. Soc.* 152 (2005) A2306–A2308.
[72] S. Ferro, Physicochemical and Electrical Properties of Praseodymium Oxides, *International Journal of Electrochemistry* 2011 (2011) 1–7. https://doi.org/10.4061/2011/561204.
[73] Y. Wang, T. Son Nguyen, C. Wang, X. Wang, Ethanol electrooxidation on Pt / C catalysts promoted with praseodymium oxide nanorods, *Dalton Transactions* 0 (2009) 7606–7609. https://doi.org/10.1039/B909324A.
[74] P.G. Corradini, E. Antolini, J. Perez, Structural and electrochemical characterization of carbon supported Pt–Pr catalysts for direct ethanol fuel cells prepared using a modified formic acid method in a CO atmosphere, *Phys. Chem. Chem. Phys.* 15 (2013) 11730–11739. https://doi.org/10.1039/C3CP51183A.
[75] H.Q.V. Nguyen, J. Nerut, H. Kasuk, M. Härmas, P. Valk, T. Romann, M. Koppel, P. Teppor, J. Aruväli, O. Korjus, O. Volobujeva, E. Lust, Optimisation of the ethylene glycol reduction method for the synthesis of platinum-ceria-carbon materials as catalysts for the methanol oxidation reaction, *J Solid State Electrochem* 27 (2023) 313–326. https://doi.org/10.1007/s10008-022-05326-4.
[76] A.-V. Prits, J. Nerut, H. Kasuk, M. Koel, S. Sepp, P. Valk, J. Aruväli, M. Koppel, V. Mikli, O. Volobujeva, E. Lust, (Digital Presentation) Carbon Aerogel Platinum-Praseodymium Oxide Nanocatalyst for Methanol Oxidation in 0.5 M Sulfuric Acid, *ECS Trans.* 108 (2022) 79. https://doi.org/10.1149/10807.0079ecst.
[77] E. Härk, S. Sepp, P. Valk, K. Vaarmets, J. Nerut, R. Jager, E. Lust, Impact of the Various Catalysts (Pt, Pt-Ru) Deposited onto Carbon Support to the Slow Oxygen Reduction Reaction Kinetics, *ECS Transactions* 45 (2013) 1–11. https://doi.org/10.1149/04521.0001ecst.
[78] A. Jänes, J. Eskusson, L. Mattisen, E. Lust, Electrochemical behaviour of hybrid devices based on Na2SO4 and Rb2SO4 neutral aqueous electrolytes and carbon electrodes within wide cell potential region, *J Solid State Electrochem* 19 (2015) 769–783. https://doi.org/10.1007/s10008-014-2668-8.
[79] T. Morishita, Y. Soneda, H. Hatori, M. Inagaki, Carbon-coated tungsten and molybdenum carbides for electrode of electrochemical capacitor, *Electrochimica Acta* 52 (2007) 2478–2484. https://doi.org/10.1016/j.electacta.2006.08.056.
[80] J. Patt, D.J. Moon, C. Phillips, L. Thompson, Molybdenum carbide catalysts for water–gas shift, *Catalysis Letters* 65 (2000) 193–195.
[81] A. Széchenyi, F. Solymosi, Production of Hydrogen in the Decomposition of Ethanol and Methanol over Unsupported Mo_2C Catalysts, *J. Phys. Chem. C* 111 (2007) 9509–9515. https://doi.org/10.1021/jp072439k.
[82] Y. Ma, G. Guan, P. Phanthong, X. Li, J. Cao, X. Hao, Z. Wang, A. Abudula, Steam reforming of methanol for hydrogen production over nanostructured wire-like molybdenum carbide catalyst, *International Journal of Hydrogen Energy* 39 (2014) 18803–18811. https://doi.org/10.1016/j.ijhydene.2014.09.062.

[83] E.C. Weigert, J. South, S.A. Rykov, J.G. Chen, Multifunctional composites containing molybdenum carbides as potential electrocatalysts, *Catalysis Today* 99 (2005) 285–290. https://doi.org/10.1016/j.cattod.2004.10.003.
[84] H. Vrubel, X. Hu, Molybdenum Boride and Carbide Catalyze Hydrogen Evolution in both Acidic and Basic Solutions, *Angew. Chem.* 124 (2012) 12875–12878. https://doi.org/10.1002/ange.201207111.
[85] Y. Liu, T.G. Kelly, J.G. Chen, W.E. Mustain, Metal Carbides as Alternative Electrocatalyst Supports, *ACS Catalysis* 3 (2013) 1184–1194. https://doi.org/10.1021/cs4001249.
[86] M. Pang, C. Li, L. Ding, J. Zhang, D. Su, W. Li, C. Liang, Microwave-Assisted Preparation of Mo_2C/CNTs Nanocomposites as Efficient Electrocatalyst Supports for Oxygen Reduction Reaction, *Industrial & Engineering Chemistry Research* 49 (2010) 4169–4174. https://doi.org/10.1021/ie901741c.
[87] L.A. Ilicheva, M.K. Frejd, V.A. Suprunov, N.A. Tyurina, Corrosion and electrochemical properties of molybdenum carbide in acid and alkaline solutions, *Soviet Powder Metallurgy Metal Ceramics* (1978) 594–598.
[88] M.C. Weidman, D.V. Esposito, Y.-C. Hsu, J.G. Chen, Comparison of electrochemical stability of transition metal carbides (WC, W_2C, Mo_2C) over a wide pH range, *Journal of Power Sources* 202 (2012) 11–17. https://doi.org/10.1016/j.jpowsour.2011.10.093.
[89] E.C. Weigert, D.V. Esposito, J.G. Chen, Cyclic voltammetry and X-ray photoelectron spectroscopy studies of electrochemical stability of clean and Pt-modified tungsten and molybdenum carbide (WC and Mo2C) electrocatalysts, *Journal of Power Sources* 193 (2009) 501–506. https://doi.org/10.1016/j.jpowsour.2009.04.020.
[90] R. Guil-López, M.V. Martínez-Huerta, O. Guillén-Villafuerte, M.A. Peña, J.L.G. Fierro, E. Pastor, Highly dispersed molybdenum carbide as non-noble electrocatalyst for PEM fuel cells: Performance for CO electrooxidation, *International Journal of Hydrogen Energy* 35 (2010) 7881–7888. https://doi.org/10.1016/j.ijhydene.2010.05.044.
[91] E.C. Weigert, N.A. Smith, B.G. Willis, A. Amorelli, J.G. Chen, PVD Synthesis and Characterization of Pt-Modified Molybdenum Carbides as Potential Electrocatalysts, *Electrochem. Solid-State Lett.* 8 (2005) A337–A340. https://doi.org/10.1149/1.1928235.
[92] G.S. Chai, S.B. Yoon, J.-S. Yu, J.-H. Choi, Y.-E. Sung, Ordered porous carbons with tunable pore sizes as catalyst supports in direct methanol fuel cell, *J. Phys. Chem. B* 108 (2004) 7074–7079. https://doi.org/10.1021/jp0370472.
[93] S. Sepp, K. Vaarmets, J. Nerut, I. Tallo, E. Tee, H. Kurig, J. Aruväli, R. Kanarbik, E. Lust, Performance of Polymer Electrolyte Membrane Fuel Cell Single Cells Prepared Using Hierarchical Microporous-Mesoporous Carbon Supported Pt Nanoparticles Activated Catalysts, *Electrochim. Acta* 203 (2016) 221–229. https://doi.org/10.1016/j.electacta.2016.03.158.
[94] C. Galeano, J.C. Meier, V. Peinecke, H. Bongard, I. Katsounaros, A.A. Topalov, A. Lu, K.J.J. Mayrhofer, F. Schüth, Toward Highly Stable Electrocatalysts via Nanoparticle Pore Confinement, *J. Am. Chem. Soc.* 134 (2012) 20457–20465. https://doi.org/10.1021/ja308570c.
[95] A.L. Patterson, The Scherrer Formula for X-Ray Particle Size Determination, *Phys. Rev.* 56 (1939) 978–982. https://doi.org/10.1103/PhysRev.56.978.

[96] P.I. Ravikovitch, A.V. Neimark, Characterization of nanoporous materials from adsorption and desorption isotherms, *Colloid. Surf A* 187–188 (2001) 11–21. https://doi.org/10.1016/S0927-7757(01)00614-8.
[97] J. Jagiello, J.P. Olivier, 2D-NLDFT adsorption models for carbon slit-shaped pores with surface energetical heterogeneity and geometrical corrugation, *Carbon* 55 (2013) 70–80. https://doi.org/10.1016/j.carbon.2012.12.011.
[98] J. Jagiello, J.P. Olivier, Carbon slit pore model incorporating surface energetical heterogeneity and geometrical corrugation, *Adsorption* 19 (2013) 777–783. https://doi.org/10.1007/s10450-013-9517-4.
[99] K. Shinozaki, J.W. Zack, R.M. Richards, B.S. Pivovar, S.S. Kocha, Oxygen Reduction Reaction Measurements on Platinum Electrocatalysts Utilizing Rotating Disk Electrode Technique I. Impact of Impurities, Measurement Protocols and Applied Corrections, *J. Electrochem. Soc.* 162 (2015) F1144–F1158. https://doi.org/10.1149/2.1071509jes.
[100] K. Shinozaki, J.W. Zack, S. Pylypenko, B.S. Pivovar, S.S. Kocha, Oxygen Reduction Reaction Measurements on Platinum Electrocatalysts Utilizing Rotating Disk Electrode Technique II. Influence of Ink Formulation, Catalyst Layer Uniformity and Thickness, *J. Electrochem. Soc.* 162 (2015) F1384–F1396. https://doi.org/10.1149/2.0551512jes.
[101] S. Sepp, J. Nerut, K. Vaarmets, R. Kanarbik, E. Härk, E. Lust, The Impact of Pt-Nanocluster Deposition and Nafion® Content on the Oxygen Electroreduction Kinetics on Molybdenum Carbide Derived Carbon Synthesized at 1000°C, *ECS Trans.* 61 (2014) 37–50. https://doi.org/10.1149/06126.0037ecst.
[102] E. Parthé, V. Sadogopan, The structure of dimolybdenum carbide by neutron diffraction technique, *Acta Crystallographica* 16 (1963) 202–205. https://doi.org/10.1107/S0365110X63000487.
[103] C. Liang, P. Ying, C. Li, Nanostructured β-Mo_2C Prepared by Carbothermal Hydrogen Reduction on Ultrahigh Surface Area Carbon Material, *Chemistry of Materials* 14 (2002) 3148–3151. https://doi.org/10.1021/cm020202p.
[104] J. Lu, H. Hugosson, O. Eriksson, L. Nordström, U. Jansson, Chemical vapour deposition of molybdenum carbides: aspects of phase stability, *Thin Solid Films* 370 (2000) 203–212. https://doi.org/10.1016/S0040-6090(00)00750-1.
[105] O. Guillén-Villafuerte, R. Guil-López, E. Nieto, G. García, J.L. Rodríguez, E. Pastor, J.L.G. Fierro, Electrocatalytic performance of different Mo-phases obtained during the preparation of innovative Pt-MoC catalysts for DMFC anode, *International Journal of Hydrogen Energy* 37 (2012) 7171–7179. https://doi.org/10.1016/j.ijhydene.2011.11.117.
[106] X. Li, W.-X. Chen, J. Zhao, W. Xing, Z.-D. Xu, Microwave polyol synthesis of Pt/CNTs catalysts: Effects of pH on particle size and electrocatalytic activity for methanol electrooxidization, *Carbon* 43 (2005) 2168–2174. https://doi.org/10.1016/j.carbon.2005.03.030.
[107] B.G. Hyde, D.J.M. Bevan, L. Eyring, On the praseodymium + oxygen system, *Phil. Trans. R. Soc. Lond. A* 259 (1966) 583–614. https://doi.org/10.1098/rsta.1966.0025.
[108] A. Netz, W.F. Chu, V. Thangadurai, R.A. Huggins, W. Weppner, Investigations of praseodymium oxide electrodes in lithium concentration cells, *Ionics* 5 (1999) 426–433. https://doi.org/10.1007/BF02376009.

[109] K.S.W. Sing, Reporting physisorption data for gas/solid systems with special reference to the determination of surface area and porosity (Recommendations 1984), *Pac* 57 (1985) 603–619. https://doi.org/10.1351/pac198557040603.
[110] J.U. Keller, R. Staudt, Adsorption isotherms, in: Gas Adsorption Equilibria, Springer US, 2005: pp. 359–413. http://link.springer.com/chapter/10.1007/0-387-23598-1_8 (accessed January 23, 2014).
[111] J. Rouquerol, D. Avnir, C.W. Fairbridge, D.H. Everett, J.M. Haynes, N. Pernicone, J.D.F. Ramsay, K.S.W. Sing, K.K. Unger, Recommendations for the characterization of porous solids (Technical Report), *Pure and Applied Chemistry* 66 (1994). https://doi.org/10.1351/pac199466081739.
[112] A.C. Ferrari, J. Robertson, Interpretation of Raman spectra of disordered and amorphous carbon, *Phys. Rev. B Condens. Matter Mater. Phys.* 61 (2000) 14095–14107. https://doi.org/10.1103/PhysRevB.61.14095.
[113] S. Urbonaite, L. Hälldahl, G. Svensson, Raman spectroscopy studies of carbide derived carbons, *Carbon* 46 (2008) 1942–1947. https://doi.org/10.1016/j.carbon.2008.08.004.
[114] T. Xiao, A.P.E. York, V.C. Williams, H. Al-Megren, A. Hanif, X. Zhou, M.L.H. Green, Preparation of Molybdenum Carbides Using Butane and Their Catalytic Performance, *Chemistry of Materials* 12 (2000) 3896–3905. https://doi.org/10.1021/cm001157t.
[115] L. Kumari, Y.-R. Ma, C.-C. Tsai, Y.-W. Lin, S.Y. Wu, K.-W. Cheng, Y. Liou, X-ray diffraction and Raman scattering studies on large-area array and nano-branched structure of 1D MoO_2 nanorods, *Nanotechnology* 18 (2007) 115717. https://doi.org/10.1088/0957-4484/18/11/115717.
[116] Y. Borchert, P. Sonström, M. Wilhelm, H. Borchert, M. Bäumer, Nanostructured Praseodymium Oxide: Preparation, Structure, and Catalytic Properties, *J. Phys. Chem. C* 112 (2008) 3054–3063. https://doi.org/10.1021/jp0768524.
[117] E. Lust, K. Vaarmets, J. Nerut, I. Tallo, P. Valk, S. Sepp, E. Härk, Influence of specific surface area and microporosity-mesoporosity of pristine and Pt-nano-clusters modified carbide derived carbon electrodes on the oxygen electro-reduction, *Electrochimica Acta* 140 (2014) 294–303. https://doi.org/10.1016/j.electacta.2014.04.054.
[118] J. Horkans, M.W. Shafer, Effect of Orientation, Composition, and Electronic Factors in the Reduction of O_2 on Single Crystal Electrodes of the Conducting Oxides of Molybdenum and Tungsten, *J. Electrochem. Soc.* 124 (1977) 1196–1202. https://doi.org/10.1149/1.2133527.
[119] B.E. Conway, Electrochemical supercapacitors: scientific fundamentals and technological applications, Springer, New York, 1999.
[120] M.J. Bleda-Martínez, D. Lozano-Castelló, E. Morallón, D. Cazorla-Amorós, A. Linares-Solano, Chemical and electrochemical characterization of porous carbon materials, *Carbon* 44 (2006) 2642–2651. https://doi.org/10.1016/j.carbon.2006.04.017.
[121] U. Retter, H. Lohse, Electrochemical Impedance Spectroscopy, in: F. Scholz (Ed.), Electroanalytical Methods, Springer Berlin Heidelberg, 2010: pp. 159–177. http://link.springer.com/chapter/10.1007/978-3-642-02915-8_8 (accessed February 2, 2015).
[122] E. Härk, J. Nerut, K. Vaarmets, I. Tallo, H. Kurig, J. Eskusson, K. Kontturi, E. Lust, Electrochemical impedance characteristics and electroreduction of oxygen

at tungsten carbide derived micromesoporous carbon electrodes, *J. Electroanal. Chem.* 689 (2013) 176–184. https://doi.org/10.1016/j.jelechem.2012.09.039.
[123] T. Thomberg, A. Jänes, E. Lust, Energy and power performance of vanadium carbide derived carbon electrode materials for supercapacitors, *J. Electroanal. Chem.* 630 (2009) 55–62. https://doi.org/10.1016/j.jelechem.2009.02.015.
[124] S. Lambert, N. Job, L. D'Souza, M.F.R. Pereira, R. Pirard, B. Heinrichs, J.L. Figueiredo, J.-P. Pirard, J.R. Regalbuto, Synthesis of very highly dispersed platinum catalysts supported on carbon xerogels by the strong electrostatic adsorption method, *Journal of Catalysis* 261 (2009) 23–33. https://doi.org/10.1016/j.jcat.2008.10.014.
[125] N. Lakshmi, N. Rajalakshmi, K.S. Dhathathreyan, Functionalization of various carbons for proton exchange membrane fuel cell electrodes: analysis and characterization, *J. Phys. D: Appl. Phys.* 39 (2006) 2785. https://doi.org/10.1088/0022-3727/39/13/022.
[126] T.J. Schmidt, H.A. Gasteiger, G.D. Stäb, P.M. Urban, D.M. Kolb, R.J. Behm, Characterization of High-Surface-Area Electrocatalysts Using a Rotating Disk Electrode Configuration, *J. Electrochem. Soc.* 145 (1998) 2354–2358. https://doi.org/10.1149/1.1838642.
[127] U.A. Paulus, T.J. Schmidt, H.A. Gasteiger, R.J. Behm, Oxygen reduction on a high-surface area Pt/Vulcan carbon catalyst: a thin-film rotating ring-disk electrode study, *Journal of Electroanalytical Chemistry* 495 (2001) 134–145. https://doi.org/10.1016/S0022-0728(00)00407-1.
[128] S.L. Gojković, S.K. Zečević, R.F. Savinell, O 2 Reduction on an Ink-Type Rotating Disk Electrode Using Pt Supported on High-Area Carbons, *J. Electrochem. Soc.* 145 (1998) 3713–3720. https://doi.org/10.1149/1.1838864.
[129] J. Suntivich, H. Gasteiger, N. Yabuuchi, Y. Shao-Horn, Electrocatalytic Measurement Methodology of Oxide Catalysts Using a Thin-Film Rotating Disk Electrode, *Journal of the Electrochemical Society* 157 (2010) B1263–B1268.
[130] V. Climent, J.M. Feliu, Thirty years of platinum single crystal electrochemistry, *J Solid State Electrochem* 15 (2011) 1297. https://doi.org/10.1007/s10008-011-1372-1.
[131] S. Trasatti, O.A. Petrii, Real Surface Area Measurements in Electrochemistry, *J. Electroanal. Chem.* 327 (1992) 353–376. https://doi.org/10.1016/0022-0728(92)80162-W.
[132] M.J. Bleda-Martínez, D. Lozano-Castelló, E. Morallón, D. Cazorla-Amorós, A. Linares-Solano, Chemical and electrochemical characterization of porous carbon materials, *Carbon* 44 (2006) 2642–2651. https://doi.org/10.1016/j.carbon.2006.04.017.
[133] F. Seland, R. Tunold, D.A. Harrington, Impedance study of methanol oxidation on platinum electrodes, *Electrochim. Acta* 51 (2006) 3827–3840. https://doi.org/10.1016/j.electacta.2005.10.050.
[134] A. M. Hofstead-Duffy, D.-J. Chen, S.-G. Sun, Y. J. Tong, Origin of the current peak of negative scan in the cyclic voltammetry of methanol electro- oxidation on Pt-based electrocatalysts: a revisit to the current ratio criterion, *J. Mater. Chem.* 22 (2012) 5205–5208. https://doi.org/10.1039/C2JM15426A.
[135] D.Y. Chung, K.-J. Lee, Y.-E. Sung, Methanol Electro-Oxidation on the Pt Surface: Revisiting the Cyclic Voltammetry Interpretation, *J. Phys. Chem. C* 120 (2016) 9028–9035. https://doi.org/10.1021/acs.jpcc.5b12303.

[136] R.E. Melnick, G.T.R. Palmore, Impedance Spectroscopy of the Electro-oxidation of Methanol on Polished Polycrystalline Platinum, *J. Phys. Chem. B* 105 (2001) 1012–1025. https://doi.org/10.1021/jp0030847.
[137] W.-Q. Bao, X.-D. He, Y. Wang, J.-B. He, Diffusion-restricted electrodeposition of platinum on solid carbon paste for electrocatalytic oxidation of methanol, *Catalysis Today* 264 (2016) 198–205. https://doi.org/10.1016/j.cattod.2015.07.013.
[138] I.-M. Hsing, X. Wang, Y.-J. Leng, Electrochemical Impedance Studies of Methanol Electro-oxidation on Pt/C Thin Film Electrode, *J. Electrochem. Soc.* 149 (2002) A615–A621. https://doi.org/10.1149/1.1467940.
[139] M.E. Orazem, N. Pébère, B. Tribollet, Enhanced Graphical Representation of Electrochemical Impedance Data, *J. Electrochem. Soc.* 153 (2006) B129–B136. https://doi.org/10.1149/1.2168377.
[140] V.M.-W. Huang, V. Vivier, M.E. Orazem, N. Pébère, B. Tribollet, The Apparent Constant-Phase-Element Behavior of a Disk Electrode with Faradaic Reactions A Global and Local Impedance Analysis, *J. Electrochem. Soc.* 154 (2007) C99–C107. https://doi.org/10.1149/1.2398894.

9. SUMMARY IN ESTONIAN

Metanooli oksüdeerumine plaatina-haruldase muldmetalli oksiidiga aktiveeritud katalüsaatoritel

Metanooli oksüdeerimise uurimiseks Pt-haruldane muldmetall katalüsaatoritel sünteesiti Pt-CeO_2-C ja Pt-PrO_x-C materjalid, mida karakteriseeriti füüsikaliste ning elektrokeemiliste uurimismeetodite abil. Uuriti haruldane muldmetall-süsinik katalüsaatorikandjate valmistamise erinevaid aspekte, näiteks haruldase muldmetalli oksiidi kaltsineerimistemperatuuri mõju. Töötati välja erinevaid meetodeid plaatina sadestamiseks süsinikkandjale.

Käesolevas töös uuriti ning kirjeldati etüleenglükooli abil sadestatud plaatina nanoosakeste omaduste sõltuvust sünteesitingimustest. Lisaks võrreldi etüleenglükooli meetodi abil sadestatud plaatina nanoosakestel saadud tulemusi vesiniku või naatriumboorhüdriidi abil sadestatud plaatina nanoosakestel mõõdetud tulemustega.

Etüleenglükooli abil sadestati plaatina nanoosakesi erinevatele süsinikkandjatele, ning uuriti hapniku redutseerumisreaktsiooni nendel katalüsaatormaterjalidel. Lisaks kirjeldati neid materjale erinevate füüsikaliste karakteriseerimismeetodite abil.

Tartu Ülikoolis välja töötatud molübdeeniumkarbiidist sünteesitud süsinike struktuuri ning elektrokeemilist stabiilsust uuriti kasutamaks neid katalüsaatorikandjatena erinevates elektrokeemilistes rakendustes.

Erinevate materjalide uurimiseks kasutati mitmesuguseid füüsikalisi karakteriseerimismeetodeid, näiteks röntgendifraktsioon, skaneeriv elektronmikroskoopia, mikrolaineplasma aatomemissioonspektromeetria, termogravimeetria, madaltemperatuurne lämmastiku adsorptsioon jpt. Sünteesitud materjalide elektrokeemilisi omadusi (katalüütiline aktiivsus, stabiilsus) uuriti tsüklilise voltamperomeetria, pöörleva ketaselektroodi meetodi, kronoamperomeetria ning elektrokeemilise impedantsspektroskoopia abil.

Osaliselt kloreeritud C(Mo_2C)+Mo_2C komposiitmaterjalide koostise uuringute tulemusel leiti, et materjalid koosnevad kristallilisest β-Mo_2C faasist ja amorfsest mikro-mesopoorsest süsinikufaasist. Madalama Mo_2C faasi sisaldusega materjalide puhul mõõdeti väga kõrged eripinna väärtused. Elektrokeemiliselt käitusid need materjalid väga laias potentsiaalivahemikus mahtuvuslikult, ning nende puhul mõõdeti väga kõrged mass-normaliseeritud mahtuvuse väärtused.

Kloreerimata Mo_2C faas lahustus elektrokeemiliste mõõtmiste käigus täielikult. Sellel oli teatav mõju materjalide lõplikule mikro-mesopoorsele struktuurile. Elektrokeemilise impedantsspektroskoopia tulemuste põhjal võib väita, et materjalide kõrgsageduslik järjestiktakistus ei sõltu Mo_2C sisaldusest, mistõttu on need materjalid sobilikud kasutamiseks kõrge energiatihedusega superkondensaatorite elektroodimaterjalidena või kütuseelementide katalüsaatorikandjatena. Selle uurimiseks sadestati Pt nanoosakesed etüleenglükooli meetodil molübdeenkarbiidist sünteesitud süsinikmaterjalile, ning saavutati arvesta-

tav elektrokeemiliselt aktiivse pindala väärtus ning üpris kõrge aktiivsus hapniku redutseerimise suhtes.

Haruldase muldmetalli oksiidiga modifitseeritud süsinikmaterjale sünteesiti erinevatel meetoditel, näiteks etüleenglükooli abil sadestamine, koossadestamine plaatinaga, ning haruldase muldmetalli hüdroksiidi kaltsineerimine erinevatel temperatuuridel. Pt nanoosakesed sadestati uuritud materjalidele erinevate meetodite abil ning leiti, et väga väikesed ning hästi jaotunud Pt osakesed saadi etüleenglükooli meetodil kõrge reaktsioonisegu pH juures ning samuti heksakloroplaatinahappe lahusega immutatud alusmaterjali kuumutamisel vesiniku juuresolekul.

Haruldase muldmetalli oksiidiga modifitseeritud materjalide sünteesitingimuste mõju materjalide kristalsusele, morfoloogiale ning stöhhiomeetriale uuriti erinevate füüsikaliste karakteriseerimismeetodite abil. Praseodüümoksiidiga modifitseeritud materjalide puhul tuvastati, et praseodüümoksiid on sadestunud nanovarrastena, mille kristalsus ja stöhhiomeetria sõltub sünteesitingimustest. Nanovardad visualiseeriti skaneeriva elektronmikroskoopia abil.

Elektrokeemiliste meetoditega tuvastati Pt-haruldase muldmetalli oksiidiga modifitseeritud materjalide hea stabiilsus ning kõrge aktiivsus metanooli oksüdeerimise suhtes. Elektrokeemiline aktiivsus sõltus nii haruldase muldmetalli oksiidi sünteesitingimustest (sünteesimeetod, kaltsineerimistemperatuur jne) kui ka Pt nanoosakeste sadestamise meetodist ning tingimustest. Kõrgeim aktiivsus metanooli oksüdeerimise suhtes tuvastati materjali Pt-PrO_x-C 1100 puhul, millel oli kõrge plaatina elektrokeemiliselt aktiivne pindala ning mis sisaldas osaliselt kristalset prasodüümoksiidi faasi, mis koosnes mitmest praseodüümoksiidi vormist.

Käesolevas töös arutati ka mõningate metanooli elektrokeemilise oksüdeerumise aspektide üle ning jõuti järeldusele, et haruldase muldmetalli oksiidiga modifitseeritud materjalide puhul annab aktiveeriva efekti nende omadus salvestada ning anda adsorbeerunud hapnikku sisaldavaid pindühendeid metanooli oksüdeerimiseks Pt nanoosakeste pinnal.

10. ACKNOWLEDGEMENTS

The author thanks

- Mr. J. Aruväli for XRD measurements,
- MSc R. Kanarbik for SEM measurements,
- PhD H. Kurig and PhD R. Palm for the low-temperature nitrogen sorption measurements
- PhD P. Paiste for ICP-MS measurements,
- PhD T. Romann for Raman measurements,
- PhD I. Tallo and PhD E. Tee for the synthesis of C(Mo_2C)+Mo_2C materials,
- PhD K. Vaarmets for Pt-C(Mo_2C) and Pt-C(Vulcan) electrochemical measurements,
- prof. K. Kontturi (Aalto University), PhD H. Jiang (Aalto University) and PhD E. Härk for HRTEM measurements,
- PhD K. Lust for comments and suggestions,
- Estonian Students Fund in USA for financial support, and
- Prof E. Lust and PhD J. Nerut for their aid, supervision, and extraordinary patience.

This work was funded by

- the Institutional Research Funding project IUT20-13 of the Estonian Ministry of Education and Research,
- the EU through the European Regional Development Fund Estonian Centre of Excellence Projects TK141 “Advanced materials and high-technology devices for energy recuperation systems” (2014-2020.4.01.15-0011) and 3.2.0101-11-0030,
- the Estonian Energy Technology Program Project 3.2.0501.10-0015 (SLOKT10209T),
- the Estonian Materials Technology project 3.2.1101.12-0019,
- grants ETF9352, ETF8267, and ETF8860,
- grants PUT55 and PUT1581, and
- grant PUT PRG676

In addition, the Graduate School of Functional Materials and Technologies receiving funding from the European Regional Development Fund in University of Tartu, Estonia.

11. PUBLICATIONS

CURRICULUM VITAE

Name: Peeter Valk
Date of birth: October 23, 1989
Citizenship: Estonian
Contact: Institute of Chemistry, University of Tartu
Ravila 14a, 50411, Tartu, Estonia
E-mail: peeter.valk@ut.ee

Education:

2015–…	University of Tartu, Institute of Chemistry, PhD student (Chemistry)
2012–2015	University of Tartu, Institute of Chemistry, MSc (Chemistry)
2009–2012	University of Tartu, Institute of Chemistry, BSc (Chemistry)

Professional employment:

2022–…	Auve Tech OÜ, Engineer
2012–…	University of Tartu, Institute of Chemistry, Chemist

Scientific publications:

1. E. Härk, S. Sepp, **P. Valk**, K. Vaarmets, J. Nerut, R. Jäger, and E. Lust, Impact of the Various Catalysts (Pt, Pt-Ru) Deposited onto Carbon Support to the Slow Oxygen Reduction Reaction Kinetics, *ECS Trans.*, **45**, 1–11 (2012).
2. S. Sepp, E. Härk, **P. Valk**, K. Vaarmets, J. Nerut, R. Jäger, and E. Lust, Impact of the Pt catalyst on the oxygen electroreduction reaction kinetics on various carbon supports, *J. Solid State Electrochem.*, **18**, 1223–1229 (2014).
3. E. Lust, K. Vaarmets, J. Nerut, I. Tallo, **P. Valk**, S. Sepp, and E. Härk, Influence of specific surface area and microporosity-mesoporosity of pristine and Pt-nanoclusters modified carbide derived carbon electrodes on the oxygen electroreduction, *Electrochim. Acta*, **140**, 294–303 (2014).
4. **P. Valk**, J. Nerut, R. Kanarbik, and E. Lust, Facile Synthesis of High Performance Platinum-Cerium Oxide Nanocatalysts for Methanol Oxidation, *ECS Trans.*, **75**, 1005–1012 (2016).
5. **P. Valk**, J. Nerut, I. Tallo, E. Tee, K. Vaarmets, T. Romann, H. Kurig, R. Palm, and E. Lust, Structure and stability of partially chlorinated molybdenum carbide composite materials synthesised via high temperature chlorination, *Electrochim. Acta*, **191**, 337–345 (2016).
6. K. Vaarmets, **P. Valk**, J. Nerut, I. Tallo, J. Aruväli, S. Sepp, and E. Lust, Rotating Disk Electrode Study of Carbon Supported Pt-nanoparticles Synthesized Using Microwave-Assisted Method, *ECS Trans.*, **80**, 743–755 (2017).

7. **P. Valk**, J. Nerut, R. Kanarbik, I. Tallo, J. Aruväli, and E. Lust, Synthesis and Characterization of Platinum-Cerium Oxide Nanocatalysts for Methanol Oxidation, *J. Electrochem. Soc.*, **165**, F315-F323 (2018).
8. **P. Valk**, J. Nerut, R. Kanarbik, J. Aruväli, P. Paiste, I. Tallo, and E. Lust, Synthesis and Characterization of Platinum-Praseodymium Oxide Nanocatalysts for Methanol Oxidation. *ECS Trans.*, **86**, 649–658 (2018).
9. **P. Valk**, J. Nerut, R. Kanarbik, J. Aruväli, P. Paiste, I. Tallo, and E. Lust, Synthesis and Characterization of Platinum-Praseodymium Oxide Nanocatalysts for Methanol Electrooxidation, *J. Electrochem. Soc.*, **166**, F1062-F1069 (2019).
10. P. Teppor, R. Jäger, J. Hints, O. Volobujeva, **P. Valk**, M. Koppel, and E. Lust, Highly Active Fe-N/C Oxygen Electrocatalysts Based on Silicon Carbide Derived Carbon, *ECS Trans*., **98**, 607–615 (2020).
11. P. Pikma, H. Ers, L. Siinor, J. Zhao, O. Oll, T. Romann, V. Grozovski, C. Siimenson, M. Väärtnõu, M. Paalo, R. Härmas, K. Lust, T. Thomberg, A. Jänes, J. Nerut, R. Jäger, **P. Valk**, I. Kivi, M. Maide, P. Möller, R. Kanarbik, G. Nurk, E. Lust, The review of advances in interfacial electrochemistry in Estonia: electrochemical double layer and adsorption studies for the development of electrochemical devices, *J. Solid State Electrochem.* (2022).
12. A.-V. Prits, J. Nerut, H. Kasuk, M. Koel, S. Sepp, **P. Valk**, J. Aruväli, M. Koppel, V. Mikli, O. Volobujeva, E. Lust, Carbon Aerogel Platinum-Praseodymium Oxide Nanocatalyst for Methanol Oxidation in 0.5 M Sulfuric Acid, *ECS Trans.* **108**, 79 (2022).
13. W. Lobjakas, J. Nerut, H. Kasuk, A. Adamson, T. Thomberg, J. Aruväli, **P. Valk**, P. Teppor, M. Koppel, V. Mikli, O. Volobujeva, E. Lust, Investigation of Oxygen Reduction on Platinum Nanoparticles Deposited Onto Peat-Derived Carbon Carrier, *ECS Trans.* **108**, 49 (2022) 49.
14. H.Q.V. Nguyen, J. Nerut, H. Kasuk, M. Härmas, **P. Valk**, T. Romann, M. Koppel, P. Teppor, J. Aruväli, O. Korjus, O. Volobujeva, E. Lust, Optimisation of the ethylene glycol reduction method for the synthesis of platinum-ceria-carbon materials as catalysts for the methanol oxidation reaction, *J. Solid State Electrochem.* **27**, 313–326 (2023).

ELULOOKIRJELDUS

Nimi: Peeter Valk
Sünniaeg: 23. oktoober 1989
Kodakondsus: eesti
Kontakt: Tartu Ülikooli keemia instituut
Ravila 14a, 50411, Tartu, Eesti
E- post: peeter.valk@ut.ee

Haridus:

2015–…	Tartu Ülikooli keemia instituut, doktoriõpe (keemia)
2012–2015	Tartu Ülikooli keemia instituut, MSc (keemia)
2009–2012	Tartu Ülikooli keemia instituut, BSc (keemia)

Teenistuskäik:

2022–…	Auve Tech OÜ, insener
2012–…	Tartu Ülikooli keemia instituut, keemik

Teaduspublikatsioonid:

1. E. Härk, S. Sepp, **P. Valk**, K. Vaarmets, J. Nerut, R. Jäger, and E. Lust, Impact of the Various Catalysts (Pt, Pt-Ru) Deposited onto Carbon Support to the Slow Oxygen Reduction Reaction Kinetics, *ECS Trans.*, **45**, 1–11 (2012).
2. S. Sepp, E. Härk, **P. Valk**, K. Vaarmets, J. Nerut, R. Jäger, and E. Lust, Impact of the Pt catalyst on the oxygen electroreduction reaction kinetics on various carbon supports, *J. Solid State Electrochem.*, **18**, 1223–1229 (2014).
3. E. Lust, K. Vaarmets, J. Nerut, I. Tallo, **P. Valk**, S. Sepp, and E. Härk, Influence of specific surface area and microporosity-mesoporosity of pristine and Pt-nanoclusters modified carbide derived carbon electrodes on the oxygen electroreduction, *Electrochim. Acta*, **140**, 294–303 (2014).
4. **P. Valk**, J. Nerut, R. Kanarbik, and E. Lust, Facile Synthesis of High Performance Platinum-Cerium Oxide Nanocatalysts for Methanol Oxidation, *ECS Trans.*, **75**, 1005–1012 (2016).
5. **P. Valk**, J. Nerut, I. Tallo, E. Tee, K. Vaarmets, T. Romann, H. Kurig, R. Palm, and E. Lust, Structure and stability of partially chlorinated molybdenum carbide composite materials synthesised via high temperature chlorination, *Electrochim. Acta*, **191**, 337–345 (2016).
6. K. Vaarmets, **P. Valk**, J. Nerut, I. Tallo, J. Aruväli, S. Sepp, and E. Lust, Rotating Disk Electrode Study of Carbon Supported Pt-nanoparticles Synthesized Using Microwave-Assisted Method, *ECS Trans.*, **80**, 743–755 (2017).

7. **P. Valk**, J. Nerut, R. Kanarbik, I. Tallo, J. Aruväli, and E. Lust, Synthesis and Characterization of Platinum-Cerium Oxide Nanocatalysts for Methanol Oxidation, *J. Electrochem. Soc.*, **165**, F315-F323 (2018).
8. **P. Valk**, J. Nerut, R. Kanarbik, J. Aruväli, P. Paiste, I. Tallo, and E. Lust, Synthesis and Characterization of Platinum-Praseodymium Oxide Nanocatalysts for Methanol Oxidation. *ECS Trans.*, **86**, 649–658 (2018).
9. **P. Valk**, J. Nerut, R. Kanarbik, J. Aruväli, P. Paiste, I. Tallo, and E. Lust, Synthesis and Characterization of Platinum-Praseodymium Oxide Nanocatalysts for Methanol Electrooxidation, *J. Electrochem. Soc.*, **166**, F1062-F1069 (2019).
10. P. Teppor, R. Jäger, J. Hints, O. Volobujeva, **P. Valk**, M. Koppel, and E. Lust, Highly Active Fe-N/C Oxygen Electrocatalysts Based on Silicon Carbide Derived Carbon, *ECS Trans*., **98**, 607–615 (2020).
11. P. Pikma, H. Ers, L. Siinor, J. Zhao, O. Oll, T. Romann, V. Grozovski, C. Siimenson, M. Väärtnõu, M. Paalo, R. Härmas, K. Lust, T. Thomberg, A. Jänes, J. Nerut, R. Jäger, **P. Valk**, I. Kivi, M. Maide, P. Möller, R. Kanarbik, G. Nurk, E. Lust, The review of advances in interfacial electrochemistry in Estonia: electrochemical double layer and adsorption studies for the development of electrochemical devices, *J. Solid State Electrochem.* (2022).
12. A.-V. Prits, J. Nerut, H. Kasuk, M. Koel, S. Sepp, **P. Valk**, J. Aruväli, M. Koppel, V. Mikli, O. Volobujeva, E. Lust, Carbon Aerogel Platinum-Praseodymium Oxide Nanocatalyst for Methanol Oxidation in 0.5 M Sulfuric Acid, *ECS Trans.* **108**, 79 (2022).
13. W. Lobjakas, J. Nerut, H. Kasuk, A. Adamson, T. Thomberg, J. Aruväli, **P. Valk**, P. Teppor, M. Koppel, V. Mikli, O. Volobujeva, E. Lust, Investigation of Oxygen Reduction on Platinum Nanoparticles Deposited Onto Peat-Derived Carbon Carrier, *ECS Trans.* **108**, 49 (2022) 49.
14. H.Q.V. Nguyen, J. Nerut, H. Kasuk, M. Härmas, **P. Valk**, T. Romann, M. Koppel, P. Teppor, J. Aruväli, O. Korjus, O. Volobujeva, E. Lust, Optimisation of the ethylene glycol reduction method for the synthesis of platinum-ceria-carbon materials as catalysts for the methanol oxidation reaction, *J. Solid State Electrochem.* **27**, 313–326 (2023).

DISSERTATIONES CHIMICAE UNIVERSITATIS TARTUENSIS

1. **Toomas Tamm.** Quantum-chemical simulation of solvent effects. Tartu, 1993, 110 p.
2. **Peeter Burk.** Theoretical study of gas-phase acid-base equilibria. Tartu, 1994, 96 p.
3. **Victor Lobanov.** Quantitative structure-property relationships in large descriptor spaces. Tartu, 1995, 135 p.
4. **Vahur Mäemets.** The ^{17}O and ^{1}H nuclear magnetic resonance study of H_2O in individual solvents and its charged clusters in aqueous solutions of electrolytes. Tartu, 1997, 140 p.
5. **Andrus Metsala.** Microcanonical rate constant in nonequilibrium distribution of vibrational energy and in restricted intramolecular vibrational energy redistribution on the basis of slater's theory of unimolecular reactions. Tartu, 1997, 150 p.
6. **Uko Maran.** Quantum-mechanical study of potential energy surfaces in different environments. Tartu, 1997, 137 p.
7. **Alar Jänes.** Adsorption of organic compounds on antimony, bismuth and cadmium electrodes. Tartu, 1998, 219 p.
8. **Kaido Tammeveski.** Oxygen electroreduction on thin platinum films and the electrochemical detection of superoxide anion. Tartu, 1998, 139 p.
9. **Ivo Leito.** Studies of Brønsted acid-base equilibria in water and non-aqueous media. Tartu, 1998, 101 p.
10. **Jaan Leis.** Conformational dynamics and equilibria in amides. Tartu, 1998, 131 p.
11. **Toonika Rinken.** The modelling of amperometric biosensors based on oxidoreductases. Tartu, 2000, 108 p.
12. **Dmitri Panov.** Partially solvated Grignard reagents. Tartu, 2000, 64 p.
13. **Kaja Orupõld.** Treatment and analysis of phenolic wastewater with microorganisms. Tartu, 2000, 123 p.
14. **Jüri Ivask.** Ion Chromatographic determination of major anions and cations in polar ice core. Tartu, 2000, 85 p.
15. **Lauri Vares.** Stereoselective Synthesis of Tetrahydrofuran and Tetrahydropyran Derivatives by Use of Asymmetric Horner-Wadsworth-Emmons and Ring Closure Reactions. Tartu, 2000, 184 p.
16. **Martin Lepiku.** Kinetic aspects of dopamine D_2 receptor interactions with specific ligands. Tartu, 2000, 81 p.
17. **Katrin Sak.** Some aspects of ligand specificity of P2Y receptors. Tartu, 2000, 106 p.
18. **Vello Pällin.** The role of solvation in the formation of iotsitch complexes. Tartu, 2001, 95 p.
19. **Katrin Kollist.** Interactions between polycyclic aromatic compounds and humic substances. Tartu, 2001, 93 p.

20. **Ivar Koppel.** Quantum chemical study of acidity of strong and superstrong Brønsted acids. Tartu, 2001, 104 p.
21. **Viljar Pihl.** The study of the substituent and solvent effects on the acidity of OH and CH acids. Tartu, 2001, 132 p.
22. **Natalia Palm.** Specification of the minimum, sufficient and significant set of descriptors for general description of solvent effects. Tartu, 2001, 134 p.
23. **Sulev Sild.** QSPR/QSAR approaches for complex molecular systems. Tartu, 2001, 134 p.
24. **Ruslan Petrukhin.** Industrial applications of the quantitative structure-property relationships. Tartu, 2001, 162 p.
25. **Boris V. Rogovoy.** Synthesis of (benzotriazolyl)carboximidamides and their application in relations with *N*- and *S*-nucleophyles. Tartu, 2002, 84 p.
26. **Koit Herodes.** Solvent effects on UV-vis absorption spectra of some solvatochromic substances in binary solvent mixtures: the preferential solvation model. Tartu, 2002, 102 p.
27. **Anti Perkson.** Synthesis and characterisation of nanostructured carbon. Tartu, 2002, 152 p.
28. **Ivari Kaljurand.** Self-consistent acidity scales of neutral and cationic Brønsted acids in acetonitrile and tetrahydrofuran. Tartu, 2003, 108 p.
29. **Karmen Lust.** Adsorption of anions on bismuth single crystal electrodes. Tartu, 2003, 128 p.
30. **Mare Piirsalu.** Substituent, temperature and solvent effects on the alkaline hydrolysis of substituted phenyl and alkyl esters of benzoic acid. Tartu, 2003, 156 p.
31. **Meeri Sassian.** Reactions of partially solvated Grignard reagents. Tartu, 2003, 78 p.
32. **Tarmo Tamm.** Quantum chemical modelling of polypyrrole. Tartu, 2003. 100 p.
33. **Erik Teinemaa.** The environmental fate of the particulate matter and organic pollutants from an oil shale power plant. Tartu, 2003. 102 p.
34. **Jaana Tammiku-Taul.** Quantum chemical study of the properties of Grignard reagents. Tartu, 2003. 120 p.
35. **Andre Lomaka.** Biomedical applications of predictive computational chemistry. Tartu, 2003. 132 p.
36. **Kostyantyn Kirichenko.** Benzotriazole – Mediated Carbon–Carbon Bond Formation. Tartu, 2003. 132 p.
37. **Gunnar Nurk.** Adsorption kinetics of some organic compounds on bismuth single crystal electrodes. Tartu, 2003, 170 p.
38. **Mati Arulepp.** Electrochemical characteristics of porous carbon materials and electrical double layer capacitors. Tartu, 2003, 196 p.
39. **Dan Cornel Fara.** QSPR modeling of complexation and distribution of organic compounds. Tartu, 2004, 126 p.
40. **Riina Mahlapuu.** Signalling of galanin and amyloid precursor protein through adenylate cyclase. Tartu, 2004, 124 p.

41. **Mihkel Kerikmäe.** Some luminescent materials for dosimetric applications and physical research. Tartu, 2004, 143 p.
42. **Jaanus Kruusma.** Determination of some important trace metal ions in human blood. Tartu, 2004, 115 p.
43. **Urmas Johanson.** Investigations of the electrochemical properties of polypyrrole modified electrodes. Tartu, 2004, 91 p.
44. **Kaido Sillar.** Computational study of the acid sites in zeolite ZSM-5. Tartu, 2004, 80 p.
45. **Aldo Oras.** Kinetic aspects of dATPαS interaction with $P2Y_1$ receptor. Tartu, 2004, 75 p.
46. **Erik Mölder.** Measurement of the oxygen mass transfer through the air-water interface. Tartu, 2005, 73 p.
47. **Thomas Thomberg.** The kinetics of electroreduction of peroxodisulfate anion on cadmium (0001) single crystal electrode. Tartu, 2005, 95 p.
48. **Olavi Loog.** Aspects of condensations of carbonyl compounds and their imine analogues. Tartu, 2005, 83 p.
49. **Siim Salmar.** Effect of ultrasound on ester hydrolysis in aqueous ethanol. Tartu, 2006, 73 p.
50. **Ain Uustare.** Modulation of signal transduction of heptahelical receptors by other receptors and G proteins. Tartu, 2006, 121 p.
51. **Sergei Yurchenko.** Determination of some carcinogenic contaminants in food. Tartu, 2006, 143 p.
52. **Kaido Tämm.** QSPR modeling of some properties of organic compounds. Tartu, 2006, 67 p.
53. **Olga Tšubrik.** New methods in the synthesis of multisubstituted hydrazines. Tartu. 2006, 183 p.
54. **Lilli Sooväli.** Spectrophotometric measurements and their uncertainty in chemical analysis and dissociation constant measurements. Tartu, 2006, 125 p.
55. **Eve Koort.** Uncertainty estimation of potentiometrically measured ph and pK_a values. Tartu, 2006, 139 p.
56. **Sergei Kopanchuk.** Regulation of ligand binding to melanocortin receptor subtypes. Tartu, 2006, 119 p.
57. **Silvar Kallip.** Surface structure of some bismuth and antimony single crystal electrodes. Tartu, 2006, 107 p.
58. **Kristjan Saal.** Surface silanization and its application in biomolecule coupling. Tartu, 2006, 77 p.
59. **Tanel Tätte.** High viscosity $Sn(OBu)_4$ oligomeric concentrates and their applications in technology. Tartu, 2006, 91 p.
60. **Dimitar Atanasov Dobchev**. Robust QSAR methods for the prediction of properties from molecular structure. Tartu, 2006, 118 p.
61. **Hannes Hagu**. Impact of ultrasound on hydrophobic interactions in solutions. Tartu, 2007, 81 p.
62. **Rutha Jäger.** Electroreduction of peroxodisulfate anion on bismuth electrodes. Tartu, 2007, 142 p.

63. **Kaido Viht.** Immobilizable bisubstrate-analogue inhibitors of basophilic protein kinases: development and application in biosensors. Tartu, 2007, 88 p.
64. **Eva-Ingrid Rõõm.** Acid-base equilibria in nonpolar media. Tartu, 2007, 156 p.
65. **Sven Tamp.** DFT study of the cesium cation containing complexes relevant to the cesium cation binding by the humic acids. Tartu, 2007, 102 p.
66. **Jaak Nerut.** Electroreduction of hexacyanoferrate(III) anion on Cadmium (0001) single crystal electrode. Tartu, 2007, 180 p.
67. **Lauri Jalukse.** Measurement uncertainty estimation in amperometric dissolved oxygen concentration measurement. Tartu, 2007, 112 p.
68. **Aime Lust.** Charge state of dopants and ordered clusters formation in CaF_2:Mn and CaF_2:Eu luminophors. Tartu, 2007, 100 p.
69. **Iiris Kahn**. Quantitative Structure-Activity Relationships of environmentally relevant properties. Tartu, 2007, 98 p.
70. **Mari Reinik.** Nitrates, nitrites, N-nitrosamines and polycyclic aromatic hydrocarbons in food: analytical methods, occurrence and dietary intake. Tartu, 2007, 172 p.
71. **Heili Kasuk.** Thermodynamic parameters and adsorption kinetics of organic compounds forming the compact adsorption layer at Bi single crystal electrodes. Tartu, 2007, 212 p.
72. **Erki Enkvist.** Synthesis of adenosine-peptide conjugates for biological applications. Tartu, 2007, 114 p.
73. **Svetoslav Hristov Slavov**. Biomedical applications of the QSAR approach. Tartu, 2007, 146 p.
74. **Eneli Härk.** Electroreduction of complex cations on electrochemically polished Bi(*hkl*) single crystal electrodes. Tartu, 2008, 158 p.
75. **Priit Möller.** Electrochemical characteristics of some cathodes for medium temperature solid oxide fuel cells, synthesized by solid state reaction technique. Tartu, 2008, 90 p.
76. **Signe Viggor.** Impact of biochemical parameters of genetically different pseudomonads at the degradation of phenolic compounds. Tartu, 2008, 122 p.
77. **Ave Sarapuu.** Electrochemical reduction of oxygen on quinone-modified carbon electrodes and on thin films of platinum and gold. Tartu, 2008, 134 p.
78. **Agnes Kütt.** Studies of acid-base equilibria in non-aqueous media. Tartu, 2008, 198 p.
79. **Rouvim Kadis.** Evaluation of measurement uncertainty in analytical chemistry: related concepts and some points of misinterpretation. Tartu, 2008, 118 p.
80. **Valter Reedo.** Elaboration of IVB group metal oxide structures and their possible applications. Tartu, 2008, 98 p.
81. **Aleksei Kuznetsov.** Allosteric effects in reactions catalyzed by the cAMP-dependent protein kinase catalytic subunit. Tartu, 2009, 133 p.

82. **Aleksei Bredihhin.** Use of mono- and polyanions in the synthesis of multisubstituted hydrazine derivatives. Tartu, 2009, 105 p.
83. **Anu Ploom.** Quantitative structure-reactivity analysis in organosilicon chemistry. Tartu, 2009, 99 p.
84. **Argo Vonk.** Determination of adenosine A_{2A}- and dopamine D_1 receptor-specific modulation of adenylate cyclase activity in rat striatum. Tartu, 2009, 129 p.
85. **Indrek Kivi.** Synthesis and electrochemical characterization of porous cathode materials for intermediate temperature solid oxide fuel cells. Tartu, 2009, 177 p.
86. **Jaanus Eskusson.** Synthesis and characterisation of diamond-like carbon thin films prepared by pulsed laser deposition method. Tartu, 2009, 117 p.
87. **Marko Lätt.** Carbide derived microporous carbon and electrical double layer capacitors. Tartu, 2009, 107 p.
88. **Vladimir Stepanov.** Slow conformational changes in dopamine transporter interaction with its ligands. Tartu, 2009, 103 p.
89. **Aleksander Trummal.** Computational Study of Structural and Solvent Effects on Acidities of Some Brønsted Acids. Tartu, 2009, 103 p.
90. **Eerold Vellemäe.** Applications of mischmetal in organic synthesis. Tartu, 2009, 93 p.
91. **Sven Parkel.** Ligand binding to 5-HT_{1A} receptors and its regulation by Mg^{2+} and Mn^{2+}. Tartu, 2010, 99 p.
92. **Signe Vahur.** Expanding the possibilities of ATR-FT-IR spectroscopy in determination of inorganic pigments. Tartu, 2010, 184 p.
93. **Tavo Romann**. Preparation and surface modification of bismuth thin film, porous, and microelectrodes. Tartu, 2010, 155 p.
94. **Nadežda Aleksejeva.** Electrocatalytic reduction of oxygen on carbon nanotube-based nanocomposite materials. Tartu, 2010, 147 p.
95. **Marko Kullapere.** Electrochemical properties of glassy carbon, nickel and gold electrodes modified with aryl groups. Tartu, 2010, 233 p.
96. **Liis Siinor.** Adsorption kinetics of ions at Bi single crystal planes from aqueous electrolyte solutions and room-temperature ionic liquids. Tartu, 2010, 101 p.
97. **Angela Vaasa.** Development of fluorescence-based kinetic and binding assays for characterization of protein kinases and their inhibitors. Tartu 2010, 101 p.
98. **Indrek Tulp.** Multivariate analysis of chemical and biological properties. Tartu 2010, 105 p.
99. **Aare Selberg.** Evaluation of environmental quality in Northern Estonia by the analysis of leachate. Tartu 2010, 117 p.
100. **Darja Lavõgina.** Development of protein kinase inhibitors based on adenosine analogue-oligoarginine conjugates. Tartu 2010, 248 p.
101. **Laura Herm.** Biochemistry of dopamine D_2 receptors and its association with motivated behaviour. Tartu 2010, 156 p.

102. **Terje Raudsepp.** Influence of dopant anions on the electrochemical properties of polypyrrole films. Tartu 2010, 112 p.
103. **Margus Marandi.** Electroformation of Polypyrrole Films: *In-situ* AFM and STM Study. Tartu 2011, 116 p.
104. **Kairi Kivirand.** Diamine oxidase-based biosensors: construction and working principles. Tartu, 2011, 140 p.
105. **Anneli Kruve.** Matrix effects in liquid-chromatography electrospray mass-spectrometry. Tartu, 2011, 156 p.
106. **Gary Urb.** Assessment of environmental impact of oil shale fly ash from PF and CFB combustion. Tartu, 2011, 108 p.
107. **Nikita Oskolkov.** A novel strategy for peptide-mediated cellular delivery and induction of endosomal escape. Tartu, 2011, 106 p.
108. **Dana Martin.** The QSPR/QSAR approach for the prediction of properties of fullerene derivatives. Tartu, 2011, 98 p.
109. **Säde Viirlaid.** Novel glutathione analogues and their antioxidant activity. Tartu, 2011, 106 p.
110. **Ülis Sõukand.** Simultaneous adsorption of Cd^{2+}, Ni^{2+}, and Pb^{2+} on peat. Tartu, 2011, 124 p.
111. **Lauri Lipping.** The acidity of strong and superstrong Brønsted acids, an outreach for the "limits of growth": a quantum chemical study. Tartu, 2011, 124 p.
112. **Heisi Kurig.** Electrical double-layer capacitors based on ionic liquids as electrolytes. Tartu, 2011, 146 p.
113. **Marje Kasari.** Bisubstrate luminescent probes, optical sensors and affinity adsorbents for measurement of active protein kinases in biological samples. Tartu, 2012, 126 p.
114. **Kalev Takkis.** Virtual screening of chemical databases for bioactive molecules. Tartu, 2012, 122 p.
115. **Ksenija Kisseljova**. Synthesis of aza-β^3-amino acid containing peptides and kinetic study of their phosphorylation by protein kinase A. Tartu, 2012, 104 p.
116. **Riin Rebane.** Advanced method development strategy for derivatization LC/ESI/MS. Tartu, 2012, 184 p.
117. **Vladislav Ivaništšev.** Double layer structure and adsorption kinetics of ions at metal electrodes in room temperature ionic liquids. Tartu, 2012, 128 p.
118. **Irja Helm.** High accuracy gravimetric Winkler method for determination of dissolved oxygen. Tartu, 2012, 139 p.
119. **Karin Kipper.** Fluoroalcohols as Components of LC-ESI-MS Eluents: Usage and Applications. Tartu, 2012, 164 p.
120. **Arno Ratas.** Energy storage and transfer in dosimetric luminescent materials. Tartu, 2012, 163 p.
121. **Reet Reinart-Okugbeni**. Assay systems for characterisation of subtype-selective binding and functional activity of ligands on dopamine receptors. Tartu, 2012, 159 p.

122. **Lauri Sikk.** Computational study of the Sonogashira cross-coupling reaction. Tartu, 2012, 81 p.
123. **Karita Raudkivi.** Neurochemical studies on inter-individual differences in affect-related behaviour of the laboratory rat. Tartu, 2012, 161 p.
124. **Indrek Saar.** Design of GalR2 subtype specific ligands: their role in depression-like behavior and feeding regulation. Tartu, 2013, 126 p.
125. **Ann Laheäär.** Electrochemical characterization of alkali metal salt based non-aqueous electrolytes for supercapacitors. Tartu, 2013, 127 p.
126. **Kerli Tõnurist.** Influence of electrospun separator materials properties on electrochemical performance of electrical double-layer capacitors. Tartu, 2013, 147 p.
127. **Kaija Põhako-Esko.** Novel organic and inorganic ionogels: preparation and characterization. Tartu, 2013, 124 p.
128. **Ivar Kruusenberg.** Electroreduction of oxygen on carbon nanomaterial-based catalysts. Tartu, 2013, 191 p.
129. **Sander Piiskop.** Kinetic effects of ultrasound in aqueous acetonitrile solutions. Tartu, 2013, 95 p.
130. **Ilona Faustova**. Regulatory role of L-type pyruvate kinase N-terminal domain. Tartu, 2013, 109 p.
131. **Kadi Tamm.** Synthesis and characterization of the micro-mesoporous anode materials and testing of the medium temperature solid oxide fuel cell single cells. Tartu, 2013, 138 p.
132. **Iva Bozhidarova Stoyanova-Slavova.** Validation of QSAR/QSPR for regulatory purposes. Tartu, 2013, 109 p.
133. **Vitali Grozovski**. Adsorption of organic molecules at single crystal electrodes studied by *in situ* STM method. Tartu, 2014, 146 p.
134. **Santa Veikšina**. Development of assay systems for characterisation of ligand binding properties to melanocortin 4 receptors. Tartu, 2014, 151 p.
135. **Jüri Liiv.** PVDF (polyvinylidene difluoride) as material for active element of twisting-ball displays. Tartu, 2014, 111 p.
136. **Kersti Vaarmets.** Electrochemical and physical characterization of pristine and activated molybdenum carbide-derived carbon electrodes for the oxygen electroreduction reaction. Tartu, 2014, 131 p.
137. **Lauri Tõntson**. Regulation of G-protein subtypes by receptors, guanine nucleotides and Mn^{2+}. Tartu, 2014, 105 p.
138. **Aiko Adamson.** Properties of amine-boranes and phosphorus analogues in the gas phase. Tartu, 2014, 78 p.
139. **Elo Kibena**. Electrochemical grafting of glassy carbon, gold, highly oriented pyrolytic graphite and chemical vapour deposition-grown graphene electrodes by diazonium reduction method. Tartu, 2014, 184 p.
140. **Teemu Näykki.** Novel Tools for Water Quality Monitoring – From Field to Laboratory. Tartu, 2014, 202 p.
141. **Karl Kaupmees.** Acidity and basicity in non-aqueous media: importance of solvent properties and purity. Tartu, 2014, 128 p.

142. **Oleg Lebedev**. Hydrazine polyanions: different strategies in the synthesis of heterocycles. Tartu, 2015, 118 p.
143. **Geven Piir.** Environmental risk assessment of chemicals using QSAR methods. Tartu, 2015, 123 p.
144. **Olga Mazina.** Development and application of the biosensor assay for measurements of cyclic adenosine monophosphate in studies of G protein-coupled receptor signalinga. Tartu, 2015, 116 p.
145. **Sandip Ashokrao Kadam.** Anion receptors: synthesis and accurate binding measurements. Tartu, 2015, 116 p.
146. **Indrek Tallo.** Synthesis and characterization of new micro-mesoporous carbide derived carbon materials for high energy and power density electrical double layer capacitors. Tartu, 2015, 148 p.
147. **Heiki Erikson.** Electrochemical reduction of oxygen on nanostructured palladium and gold catalysts. Tartu, 2015, 204 p.
148. **Erik Anderson.** *In situ* Scanning Tunnelling Microscopy studies of the interfacial structure between Bi(111) electrode and a room temperature ionic liquid. Tartu, 2015, 118 p.
149. **Girinath G. Pillai.** Computational Modelling of Diverse Chemical, Biochemical and Biomedical Properties. Tartu, 2015, 140 p.
150. **Piret Pikma.** Interfacial structure and adsorption of organic compounds at Cd(0001) and Sb(111) electrodes from ionic liquid and aqueous electrolytes: an *in situ* STM study. Tartu, 2015, 126 p.
151. **Ganesh babu Manoharan.** Combining chemical and genetic approaches for photoluminescence assays of protein kinases. Tartu, 2016, 126 p.
152. **Carolin Siimenson**. Electrochemical characterization of halide ion adsorption from liquid mixtures at Bi(111) and pyrolytic graphite electrode surface. Tartu, 2016, 110 p.
153. **Asko Laaniste.** Comparison and optimisation of novel mass spectrometry ionisation sources. Tartu, 2016, 156 p.
154. **Hanno Evard.** Estimating limit of detection for mass spectrometric analysis methods. Tartu, 2016, 224 p.
155. **Kadri Ligi.** Characterization and application of protein kinase-responsive organic probes with triplet-singlet energy transfer. Tartu, 2016, 122 p.
156. **Margarita Kagan.** Biosensing penicillins' residues in milk flows. Tartu, 2016, 130 p.
157. **Marie Kriisa.** Development of protein kinase-responsive photoluminescent probes and cellular regulators of protein phosphorylation. Tartu, 2016, 106 p.
158. **Mihkel Vestli.** Ultrasonic spray pyrolysis deposited electrolyte layers for intermediate temperature solid oxide fuel cells. Tartu, 2016, 156 p.
159. **Silver Sepp**. Influence of porosity of the carbide-derived carbon on the properties of the composite electrocatalysts and characteristics of polymer electrolyte fuel cells. Tartu, 2016, 137 p.
160. **Kristjan Haav**. Quantitative relative equilibrium constant measurements in supramolecular chemistry. Tartu, 2017, 158 p.

161. **Anu Teearu**. Development of MALDI-FT-ICR-MS methodology for the analysis of resinous materials. Tartu, 2017, 205 p.
162. **Taavi Ivan**. Bifunctional inhibitors and photoluminescent probes for studies on protein complexes. Tartu, 2017, 140 p.
163. **Maarja-Liisa Oldekop**. Characterization of amino acid derivatization reagents for LC-MS analysis. Tartu, 2017, 147 p.
164. **Kristel Jukk**. Electrochemical reduction of oxygen on platinum- and palladium-based nanocatalysts. Tartu, 2017, 250 p.
165. **Siim Kukk**. Kinetic aspects of interaction between dopamine transporter and *N*-substituted nortropane derivatives. Tartu, 2017, 107 p.
166. **Birgit Viira**. Design and modelling in early drug development in targeting HIV-1 reverse transcriptase and Malaria. Tartu, 2017, 172 p.
167. **Rait Kivi**. Allostery in cAMP dependent protein kinase catalytic subunit. Tartu, 2017, 115 p.
168. **Agnes Heering**. Experimental realization and applications of the unified acidity scale. Tartu, 2017, 123 p.
169. **Delia Juronen**. Biosensing system for the rapid multiplex detection of mastitis-causing pathogens in milk. Tartu, 2018, 85 p.
170. **Hedi Rahnel.** ARC-inhibitors: from reliable biochemical assays to regulators of physiology of cells. Tartu, 2018, 176 p.
171. **Anton Ruzanov.** Computational investigation of the electrical double layer at metal–aqueous solution and metal–ionic liquid interfaces. Tartu, 2018, 129 p.
172. **Katrin Kestav.** Crystal Structure-Guided Development of Bisubstrate-Analogue Inhibitors of Mitotic Protein Kinase Haspin. Tartu, 2018, 166 p.
173. **Mihkel Ilisson.** Synthesis of novel heterocyclic hydrazine derivatives and their conjugates. Tartu, 2018, 101 p.
174. **Anni Allikalt.** Development of assay systems for studying ligand binding to dopamine receptors. Tartu, 2018, 160 p.
175. **Ove Oll.** Electrical double layer structure and energy storage characteristics of ionic liquid based capacitors. Tartu, 2018, 187 p.
176. **Rasmus Palm.** Carbon materials for energy storage applications. Tartu, 2018, 114 p.
177. **Jörgen Metsik.** Preparation and stability of poly(3,4-ethylenedioxythiophene) thin films for transparent electrode applications. Tartu, 2018, 111 p.
178. **Sofja Tšepelevitš.** Experimental studies and modeling of solute-solvent interactions. Tartu, 2018, 109 p.
179. **Märt Lõkov.** Basicity of some nitrogen, phosphorus and carbon bases in acetonitrile. Tartu, 2018, 104 p.
180. **Anton Mastitski**. Preparation of α-aza-amino acid precursors and related compounds by novel methods of reductive one-pot alkylation and direct alkylation. Tartu, 2018, 155 p.
181. **Jürgen Vahter**. Development of bisubstrate inhibitors for protein kinase CK2. Tartu, 2019, 186 p.

182. **Piia Liigand.** Expanding and improving methodology and applications of ionization efficiency measurements. Tartu, 2019, 189 p.
183. **Sigrid Selberg.** Synthesis and properties of lipophilic phosphazene-based indicator molecules. Tartu, 2019, 74 p.
184. **Jaanus Liigand.** Standard substance free quantification for LC/ESI/MS analysis based on the predicted ionization efficiencies. Tartu, 2019, 254 p.
185. **Marek Mooste.** Surface and electrochemical characterisation of aryl film and nanocomposite material modified carbon and metal-based electrodes. Tartu, 2019, 304 p.
186. **Mare Oja.** Experimental investigation and modelling of pH profiles for effective membrane permeability of drug substances. Tartu, 2019, 306 p.
187. **Sajid Hussain.** Electrochemical reduction of oxygen on supported Pt catalysts. Tartu, 2019, 220 p.
188. **Ronald Väli.** Glucose-derived hard carbon electrode materials for sodium-ion batteries. Tartu, 2019, 180 p.
189. **Ester Tee.** Analysis and development of selective synthesis methods of hierarchical micro- and mesoporous carbons. Tartu, 2019, 210 p.
190. **Martin Maide.** Influence of the microstructure and chemical composition of the fuel electrode on the electrochemical performance of reversible solid oxide fuel cell. Tartu, 2020, 144 p.
191. **Edith Viirlaid.** Biosensing Pesticides in Water Samples. Tartu, 2020, 102 p.
192. **Maike Käärik.** Nanoporous carbon: the controlled nanostructure, and structure-property relationships. Tartu, 2020, 162 p.
193. **Artur Gornischeff.** Study of ionization efficiencies for derivatized compounds in LC/ESI/MS and their application for targeted analysis. Tartu, 2020, 124 p.
194. **Reet Link.** Ligand binding, allosteric modulation and constitutive activity of melanocortin-4 receptors. Tartu, 2020, 108 p.
195. **Pilleriin Peets.** Development of instrumental methods for the analysis of textile fibres and dyes. Tartu, 2020, 150 p.
196. **Larisa Ivanova.** Design of active compounds against neurodegenerative diseases. Tartu, 2020, 152 p.
197. **Meelis Härmas.** Impact of activated carbon microstructure and porosity on electrochemical performance of electrical double-layer capacitors. Tartu, 2020, 122 p.
198. **Ruta Hecht.** Novel Eluent Additives for LC-MS Based Bioanalytical Methods. Tartu, 2020, 202 p.
199. **Max Hecht.** Advances in the Development of a Point-of-Care Mass Spectrometer Test. Tartu, 2020, 168 p.
200. **Ida Rahu.** Bromine formation in inorganic bromide/nitrate mixtures and its application for oxidative aromatic bromination. Tartu, 2020, 116 p.
201. **Sander Ratso**. Electrocatalysis of oxygen reduction on non-precious metal catalysts. Tartu, 2020, 371 p.
202. **Astrid Darnell.** Computational design of anion receptors and evaluation of host-guest binding. Tartu, 2021, 150 p.

203. **Ove Korjus.** The development of ceramic fuel electrode for solid oxide cells. Tartu, 2021, 150 p.
204. **Merit Oss.** Ionization efficiency in electrospray ionization source and its relations to compounds' physico-chemical properties. Tartu, 2021, 124 p.
205. **Madis Lüsi**. Electroreduction of oxygen on nanostructured palladium catalysts. Tartu, 2021, 180 p.
206. **Eliise Tammekivi.** Derivatization and quantitative gas-chromatographic analysis of oils. Tartu, 2021, 122 p.
207. **Simona Selberg.** Development of Small-Molecule Regulators of Epi-transcriptomic Processes. Tartu, 2021, 122 p.
208. **Olivier Etebe Nonga.** Inhibitors and photoluminescent probes for in vitro studies on protein kinases PKA and PIM. Tartu, 2021, 189 p.
209. **Riinu Härmas.** The structure and H2 diffusion in porous carbide-derived carbon particles. Tartu, 2022, 123 p.
210. **Maarja Paalo.** Synthesis and characterization of novel carbon electrodes for high power density electrochemical capacitors. Tartu, 2022, 144 p.
211. **Jinfeng Zhao.** Electrochemical characteristics of Bi(hkl) and micro-meso-porous carbon electrodes in ionic liquid based electrolytes. Tartu, 2022, 134 p.
212. **Alar Heinsaar.** Investigation of oxygen electrode materials for high-temperature solid oxide cells in natural conditions. Tartu, 2022, 120 p.
213. **Jaana Lilloja.** Transition metal and nitrogen doped nanocarbon cathode catalysts for anion exchange membrane fuel cells. Tartu, 2022, 202 p.
214. **Maris-Johanna Tahk.** Novel fluorescence-based methods for illuminating transmembrane signal transduction by G-protein coupled receptors. Tartu, 2022, 200 p.
215. **Eerik Jõgi.** Development and Applications of E. coli Immunosensor. Tartu, 2022, 103 p.
216. **Alo Rüütel.** Design principles of synthetic molecular receptors for anion-selective electrodes. Tartu, 2022, 109 p.
217. **Tanel Sõrmus.** Development of stimuli-responsive and covalent bisubstrate inhibitors of protein kinases. Tartu, 2022, 148 p.
218. **Oleg Artemchuk.** Autotrophic nitrogen removal processes for nutrient removal from sidestream and mainstream wastewater. Tartu, 2022, 115 p.
219. **Andre Leesment.** Quantitative studies of Brønsted acidity in biphasic systems and gas-phase. Tartu, 2023, 83 p.
220. **Meeli Arujõe-Sado.** Structural effects in aza-peptide bond formation reaction. Tartu, 2023, 83 p.
221. **Jonas Mart Linge.** Electrochemical reduction of oxygen on silver-based catalysts. Tartu, 2023, 269 p.
222. **Tõnis Laasfeld.** Integrating Image Analysis and Quantitative Modeling for a Holistic View of GPCR Ligand Binding Dynamics. Tartu, 2023, 226 p.
223. **Ernesto de Jesus Zapata Flores.** Derivatization Reagents used in negative mode electrospray LC-MS. Tartu, 2023, 107 p.

224. **Patrick Teppor.** Obtaining platinum-free oxygen reduction catalysts through biomass valorization: a case study of peat. Tartu, 2023, 161 p.